2024

# Structural Construction and Surface Modification of Copper Current Collectors for Lithium Metal Batteries

Yaohua Liang
*South Dakota State University*, liangyh2020@gmail.com

# STRUCTURAL CONSTRUCTION AND SURFACE MODIFICATION OF COPPER CURRENT COLLECTORS FOR LITHIUM METAL BATTERIES

BY

YAOHUA LIANG

A dissertation submitted in partial fulfillment of the requirements for the

Doctor of Philosophy

Major in Agricultural and Biosystems Engineering

South Dakota State University

2024

DISSERTATION ACCEPTANCE PAGE
Yaohua Liang

This dissertation is approved as a creditable and independent investigation by a candidate for the Doctor of Philosophy degree and is acceptable for meeting the dissertation requirements for this degree. Acceptance of this does not imply that the conclusions reached by the candidate are necessarily the conclusions of the major department.

Zhengrong Gu
Advisor Date

Kasiviswanathan Muthukumarappan
Department Head Date

Nicole Lounsbery, PhD
Director, Graduate School Date

# ACKNOWLEDGEMENTS

I would like to express my deepest gratitude to all those who have contributed to the completion of this doctoral thesis. First and foremost, I extend my sincere appreciation to my academic advisor, Dr. Zhengrong Gu, for his guidance, support, and invaluable insights throughout the entirety of my doctoral journey. His mentorship and commitment to excellence have been instrumental in shaping the direction and quality of this research.

I am thankful for the unwavering support of the members of my doctoral committee, Dr. Xufei Yang, Dr. Songxin Tan, Dr. Ruanbao Zhou. Their constructive feedback, scholarly expertise, and encouragement have significantly enriched the content and rigor of this thesis.

I extend my heartfelt thanks to South Dakota State University for providing the necessary resources and a conducive academic environment. The access to state-of-the-art facilities, libraries, and research materials has greatly facilitated the realization of this project. My gratitude extends to my colleagues and fellow researchers who have offered valuable insights and engaged in thought-provoking discussions, enhancing the intellectual atmosphere of our academic community. I wish to acknowledge the financial support provided by NSF EPSCoR South Dakota 2D Materials for Biofilm Engineering, Science, and Technology Center (2DBEST) (No. OIA–1849206), as well as from the USDA–Sungrant project "Advancing the Bioeconomy through Regional Sun Grant Centers" (SA2000386). Their generosity has played a crucial role in enabling the successful completion of this research. To my friends and family, your unwavering support, understanding, and encouragement have been my pillars of strength. Your belief in my

abilities and your enduring patience during the challenges of this journey are deeply appreciated.

Finally, I express my deepest gratitude to all the participants and contributors who willingly participated in this study. Your willingness to share your experiences and insights has been indispensable to the accomplishment of this research. This thesis is the result of collaborative efforts and collective support, and I am sincerely thankful to each and every person who has played a role, big or small, in making this academic endeavor a reality.

CONTENTS

# ABBREVIATIONS

| | |
|---|---|
| EIS | Electrochemical Impedance Spectroscopy |
| CE | Coulombic efficiency |
| SEM | Scanning electron microscopy |
| EDX | Energy Dispersive X-Ray Analysis |
| STEM | Scanning Transmission Electron Microscopy |
| XRD | X-ray diffraction |
| LFP | Lithium iron phosphate |
| M | molar |
| mL | milliliter |
| eV | electron-volt |
| SHE | Standard hydrogen electrode |
| WE | Working electrode |
| XPS | X-ray photoelectron spectroscopy |
| LMA | Lithium Metal Anode |
| CPA@CF | Cu pyramid array |
| 3D | Three dimensional |
| CF | Cu foil |
| SEI | Solid Electrolyte Interphase |
| SCE | Saturated calomel electrode |
| PDF | Powder Diffraction File |
| Au@CuPPA | Gold (Au)-coated copper (Cu) pentagonal pyramid array |
| LMB | Lithium metal batteries |

# LIST OF FIGURES

# LIST OF TABLES

# ABSTRACT

STRUCTURAL CONSTRUCTION AND SURFACE MODIFICATION OF COPPER CURRENT COLLECTORS FOR LITHIUM METAL BATTERIES

YAOHUA LIANG

2024

Graphene, a prevalent anode material in commercial lithium-ion batteries, has reached its theoretical capacity limit. The imperative is to develop high-capacity anode materials to meet the growing demand for energy density. Lithium metal, renowned for its exceptionally high theoretical specific capacity density (3680 mAh $g^{-1}$) and low reduction potential (-3.04 V, relative to the standard hydrogen electrode), is commonly dubbed the "Holy Grail" for negative electrode materials in high-energy-density batteries. However, practical advancements in lithium metal anodes face obstacles like low Coulombic efficiency, limited cycle life, and heightened reactivity to the electrolyte and internal short circuits resulting from lithium dendrite growth.

In electrochemical systems, the current collector acts as the substrate for lithium metal deposition/stripping, and its surface properties significantly influence the cycle stability of the lithium metal anode. This dissertation systematically designs various interface modification strategies to stabilize lithium metal anodes, considering the surface composition and microstructure design of the anode current collector.

The dissertation introduces three innovative surface engineering strategies for modifying copper foil current collectors. Firstly, a three-dimensional structural copper pyramid array (CPA@CF) is formed on a flat copper foil (CF) through a straightforward electrodeposition method. This distinctive CPA@CF, featuring a substantial surface area

and a porous 3D structure, enhances the diffusion of lithium ions and facilitates charge transfer, effectively mitigating the volume change of Li. In the second approach, three-dimensional lithiophilic gold (Au)-coated copper (Cu) pentagonal pyramid arrays (Au@CuPPA) are engineered on copper foil utilizing a combination of electrodeposition and chemical reduction methods. With lithiophilic layers and a 3D porous structure, the Au@CuPPA enhances the deposition/stripping process of lithium ions and reduces nucleation overpotential. Finally, a facile method is presented where 3D structured cuprous oxide ($Cu_2O$) dendrites are grown on flat copper foil through a simple process involving electrodeposition and subsequent high-temperature treatment. The lithophilic $Cu_2O$ layer formed further establishes a favorable channel for the rapid diffusion of lithium ions ($Li^+$) at the solid-liquid interface. The staggered stacking of $Cu_2O$ dendrites forms a 3D structure with a significantly increased specific surface area, alleviating current density and promoting the uniform distribution of Li flow.

The objective of this dissertation is to establish a lithiophilic interface and devise micro-nano structures on the copper current collector, effectively governing the stable deposition of lithium metal, thereby seeking to advance the practical implementation of lithium metal anodes in high-energy-density battery systems.

# CHAPTER 1 INTRODUCTION

## 1.1 Background

As society progresses, the demand for energy continues to rise [1]. Efficient energy storage and conversion devices play a pivotal role in driving social advancement, and the advent of batteries has enabled more effective and convenient energy use [2, 3]. Over the past century, various battery configurations [4], such as lead-acid, nickel-cadmium, nickel-metal hydride, fuel cells, and lithium-ion batteries (Figure 1.1), have been commercially available. Among these, lithium-ion batteries have revolutionized communication and transportation methods, fostering the development of modern society with the Internet of Things and smart cities. They have also spurred the growth of application scenarios like mobile electronic terminals and electric vehicles [5].

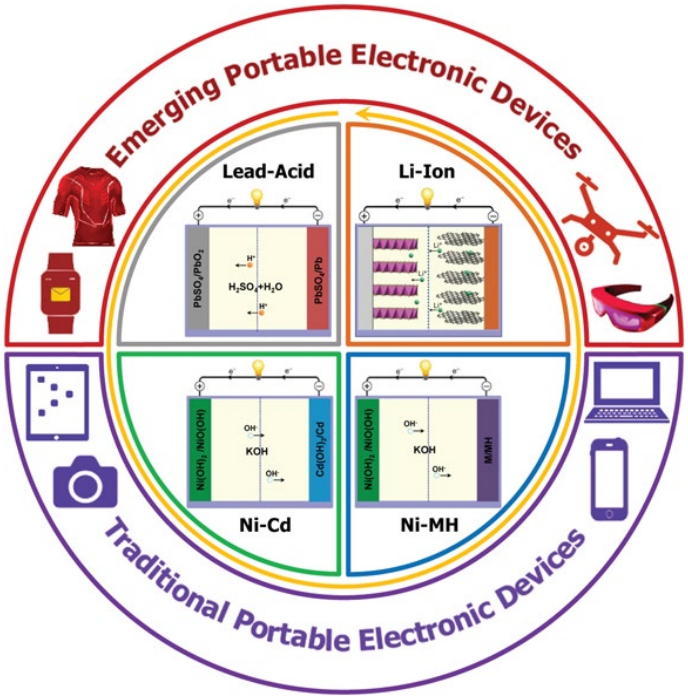


**Figure 1.1** Various secondary battery technologies [4].

Despite decades of development, lithium-ion batteries using graphite as the negative electrode and oxide as the positive electrode have become ubiquitous in modern life. However, the energy density of these commercial batteries has seen slow growth [6]. The theoretical capacity density of graphite anode material is 372 mAh $g^{-1}$, and the lithium insertion potential is high (Figure 1.2) [7]. Moreover, the actual energy density of graphite anodes is approaching its theoretical limit [8]. To enhance the energy density of lithium batteries, there is an urgent need to explore emerging anode materials with higher specific capacities. Lithium metal emerges as a promising option due to its ultra-high theoretical specific capacity density (3860 mAh $g^{-1}$), low reduction potential (-3.04 V, relative to the standard hydrogen electrode), and low density (0.53 g $cm^{-3}$) [9]. It is considered the "holy grail" anode material for improving the energy density of lithium batteries [10, 11].

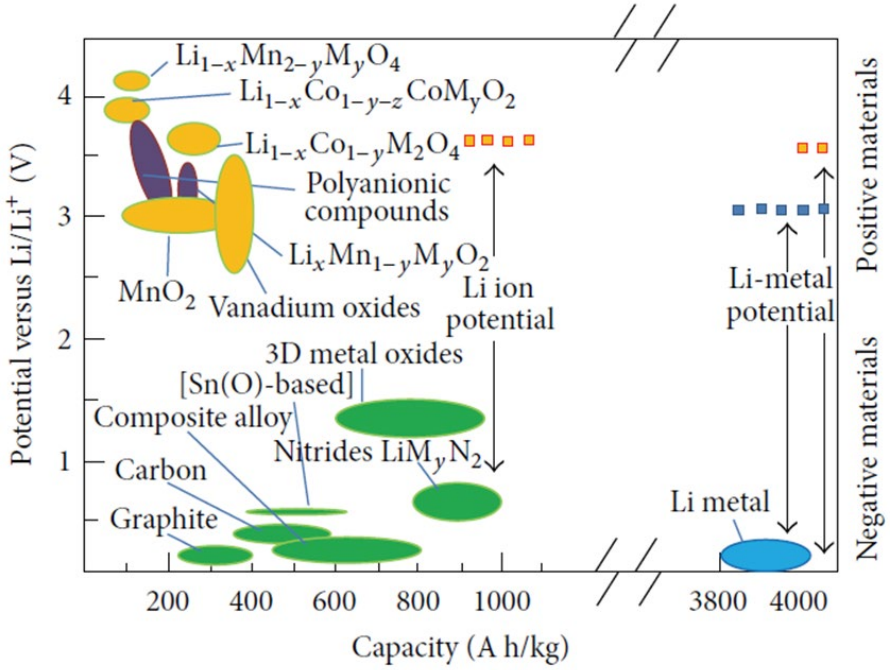


**Figure 1.2** Comparison of potential and capacity of anode materials for lithium batteries [7].

A lithium battery comprising metallic lithium and transition metal oxide cathode materials can achieve a theoretical energy density of up to 440 Wh $kg^{-1}$ [12]. Coupled with other high-specific-energy cathode materials like sulfur and oxygen, the theoretical energy densities of lithium-sulfur and lithium-oxygen batteries can reach 650 Wh $kg^{-1}$ and 950 Wh $kg^{-1}$, respectively [13, 14]. Therefore, lithium metal batteries, utilizing metallic lithium as the negative electrode material, hold the potential to overcome the energy density limitations of current lithium-ion batteries, significantly enhancing battery life in applications such as mobile electronic terminals and electric vehicles [15, 16].

### 1.2 Working principle of Lithium metal batteries

Lithium metal batteries and lithium-ion batteries both fall under the category of lithium batteries. A lithium-ion battery is a rechargeable battery (secondary battery) that relies on the movement of lithium ions between positive and negative electrodes [17, 18]. During the charge and discharge process, $Li^+$ intercalates and deintercalates between the two electrodes. In the charging phase, $Li^+$ deintercalates from the positive electrode, embedding into the negative electrode through the electrolyte, resulting in a lithium-rich state for the negative electrode. Conversely, during discharge, the process is reversed. Graphite is commonly used as the negative electrode material for lithium-ion batteries. The operational reaction of the graphite anode is expressed as [19]: $6C+xLi^++xe^- = Li_xC_6$. On the other hand, lithium metal batteries utilize metallic lithium as the negative electrode, and the corresponding positive electrode materials can include oxygen, elemental sulfur, metal oxides, and other substances. The lithium metal anode undergoes a deposition/stripping behavior of lithium, akin to an electroplating process, without

involving the intercalation and deintercalation of lithium ions. The operational reaction of the lithium metal anode is represented as: $Li\text{-}e^{-} = Li^{+}$ (Figure 1.3) [20].

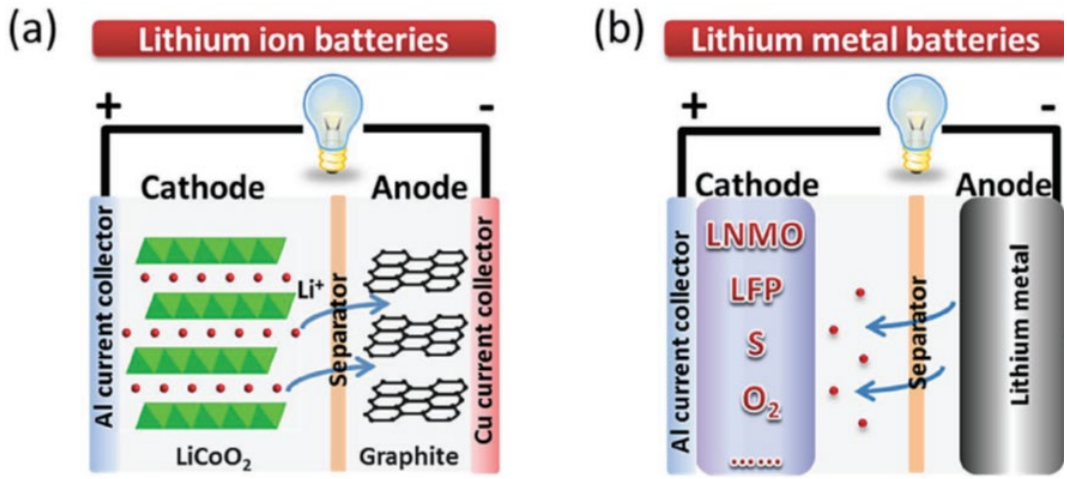


**Figure 1.3** The working mechanism of lithium-ion batteries (a) and lithium metal batteries (b) [20].

### 1.3 The challenges of Lithium metal anode

In the 1970s, Dr. M. Stanley Whittingham, a scientist at Exxon, pioneered the use of lithium metal anodes paired with titanium sulfide to create batteries [21, 22]. These batteries were initially employed in calculators, electronic watches, and implantable medical devices. Even today, lithium metal batteries continue to be utilized in pacemakers [23]. However, the lithium metal batteries mentioned earlier were exclusively primary batteries. In the 1980s, Morley Energy developed the first generation of rechargeable lithium metal batteries, showcasing exceptionally high energy density [24, 25]. Nonetheless, these lithium metal batteries faced significant challenges, including poor cycle performance and potential safety risks [26, 27]. These issues stem from the intrinsic thermodynamic properties of metallic lithium anodes and the instability of the

electrode interface caused by uncontrollable lithium dendrite growth during cycling [28, 29].

### 1.3.1 Thermodynamic properties of metallic lithium anode

Being the lightest element among alkali metals, lithium possesses the smallest atomic radius among all metals [30]. This characteristic grants metallic lithium an exceptionally high electrochemical equivalent and fast diffusion behavior [31]. Similar to other alkali metals, metallic lithium is highly reactive and can react slowly even in dry air. The presence of even a small amount of moisture leads to the rapid oxidation of lithium metal. Consequently, metallic lithium in the air is inevitably covered by an outer oxide layer, comprising lithium oxide, lithium hydroxide, lithium carbonate, and lithium nitride [32, 33]. Due to its high reactivity, elemental lithium does not exist in nature; only lithium compounds are found. Commercial lithium metal elements are produced through electrolysis [34].

When used as a battery electrode, metallic lithium exhibits the most negative potential (-3.040 V vs. the standard hydrogen electrode) [35]. This characteristic allows lithium metal batteries, utilizing metallic lithium as the negative electrode, to achieve higher voltage and theoretical energy density [36]. However, the highly negative potential also results in the high electrochemical reactivity of metallic lithium, making it challenging for it to exist stably in any electrolyte.

In contrast to other embedded anodes (such as silicon, carbon, tin), metallic lithium functions as a conversion anode. At the interface between the electrolyte and metallic lithium, lithium ions are electrochemically reduced to metallic lithium, which is deposited on the surface of the lithium sheet. The reverse process occurs during the

removal of metallic lithium. While the calculation method for embedded negative electrodes with a skeleton would suggest an infinite capacity for metallic lithium, given its nature as a conversion negative electrode without a skeleton, the general approach bases the capacity of metallic lithium anode on metallic lithium itself. This approach reveals a high theoretical specific capacity of 3860 mAh $g^{-1}$ [37].

### 1.3.2 Effect of lithium dendrite growth on anode and battery performance

Lithium metal, like everything, has its dual nature. While the metallic lithium anode boasts excellent theoretical properties, it faces serious practical challenges. Its advantages and issues encompass the following: (1) Metallic lithium exhibits high reactivity, contributing to an extremely high theoretical energy density [38]. However, this high activity leads to severe side reactions between metallic lithium and the electrolyte. These reactions cause irreversible consumption of the active material, resulting in low utilization of the metallic lithium anode [39, 40].

(2) Metal lithium, as a conductive conversion-type anode, acts as its electron channel, theoretically not requiring an external skeleton for the charge and discharge process [41]. However, the actual metal lithium anode experiences dendrite growth and volume expansion effects during operation [42]. These effects significantly impact the battery's utilization rate and service life, limiting the practical application of metallic lithium anodes. The mentioned issues are either directly caused by dendrite growth or further aggravated by it.

Dendrites refer to irregular lithium deposits that form during the charging process, unevenly depositing lithium ions on the surface of the negative electrode. Under certain dynamic conditions, the top growth rate is significantly faster than radial growth,

resulting in a one-dimensional fibrous structure [43]. There are three manifestations of this one-dimensional morphology: needle-like dendrites, mossy dendrites, and dendritic dendrites (Figure 1.4) [44-46]. Needle-like dendrites maintain a one-dimensional structure without many branches [47]. Mossy dendrites have more defects and bifurcations, growing uniformly in all directions [48]. Dendritic dendrites share similarities with mossy dendrites but generally grow around a specific branch [49]. In the actual dendrite growth process of metal lithium batteries, these morphologies have no strict boundaries, sometimes transforming into each other or coexisting within lithium metal batteries [50].

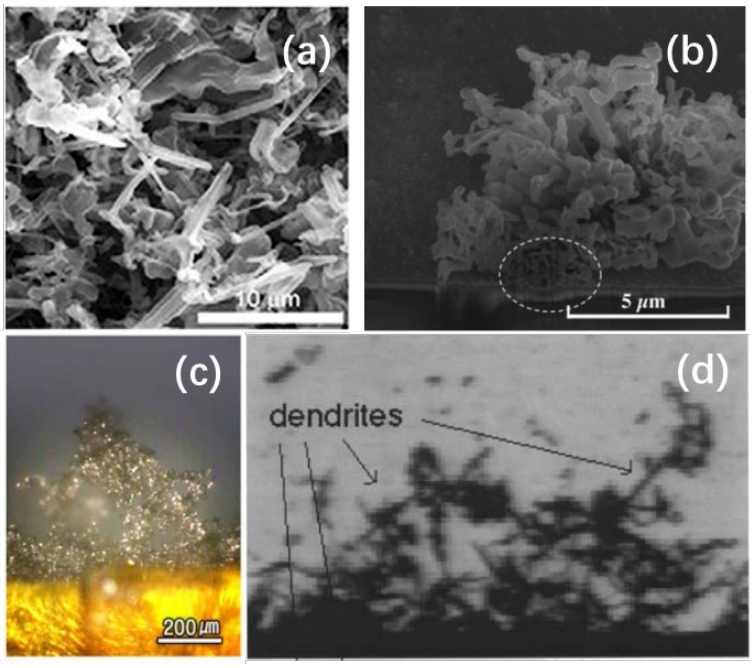


**Figure 1.4** Different morphologies of lithium dendrites. (a) needle-like [44], (b) mossy-structure [46], (c, d) tree-like [49, 50].

Dendritic growth poses a significant challenge to metallic lithium batteries, especially in large batteries, where the uneven deposition of lithium ions due to uneven current density

becomes pronounced [51]. In practical soft-pack batteries, the negative electrode current can easily reach several hundred milliamps [52]. If the negative electrode surface is uneven, creating a substantial local current at certain locations, it can lead to severe dendrite growth [53, 54]. This dendritic growth can result in the following four problems for the metallic lithium anode (Figure 1.5) [55]:

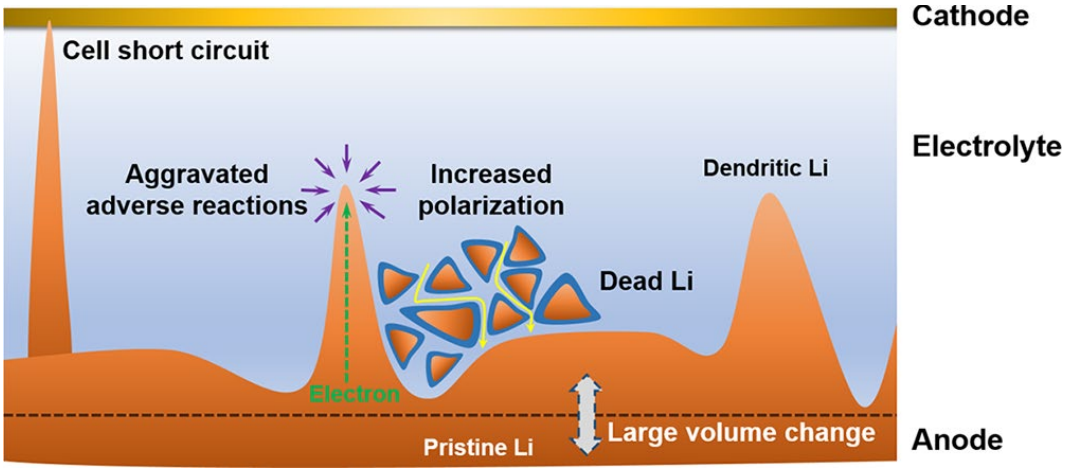


**Figure 1.5** The harm caused by dendrite growth to batteries [55].

(1) Battery short circuit. Dendrites, originating from the surface of the negative electrode, have the potential to penetrate the separator and make contact with the positive electrode material of the battery. This electronic contact between the positive and negative electrodes results in a short circuit [56]. Such short circuits are often accompanied by battery thermal runaway and can lead to electrolyte fires and battery explosions. The initial practical application of lithium metal batteries faced a setback due to the safety concerns posed by dendrite-induced short circuit issues [57]. The occurrence of battery short circuits caused by dendrite growth and the associated safety hazards are pivotal factors hindering the widespread practical application of metallic lithium anodes [58, 59].

(2) Aggravated side effects. The high reactivity of metallic lithium results in severe side reactions with the electrolyte [60]. Dendrite growth contributes to this issue in two ways: firstly, it destroys the Solid Electrolyte Interphase (SEI) film on the surface of the negative electrode, exposing more fresh lithium flakes to the electrolyte, leading to the formation of a new SEI [61, 62]. Secondly, the dendrite-like morphology increases the specific surface area of metallic lithium, expanding the contact area and promoting side reactions between metallic lithium and the electrolyte. These side reactions irreversibly consume the lithium active material and electrolyte but do not contribute to the discharge capacity. As a result, dendrite growth is often accompanied by intense side reactions, significantly reducing battery utilization [63].

(3) Polarization increases. The side reaction between metallic lithium and the electrolyte leads to the formation of a non-conductive film on the surface of metallic lithium. During the discharge process, the dendrite roots experience high current density, causing rapid electron loss and subsequent breakage of the dendrite roots [64, 65]. The uneven detachment of dendrites can transform them into non-functional dead lithium. These dead lithium formations significantly impede the transmission path of lithium ions and electrons in the negative electrode, resulting in severe polarization and decreased energy efficiency [66, 67].

(4) Huge volume expansion. Being a conversion-type anode without a skeleton, the metallic lithium anode exhibits infinite volume expansion during the deposition and extraction process of lithium ions. This expansion is much higher compared to graphite anodes (10%) and silicon anodes (400%) [68, 69]. The presence of dendrites makes metallic lithium, in the lithium-embedded state, more porous, occupying greater volume

and lower packing density. This porous structure undergoes significant volume changes upon the release of metallic lithium, posing a substantial challenge to the safe and efficient operation of metallic lithium [70, 71].

Dendrite growth not only introduces serious safety risks but also leads to low Coulombic efficiency and a shortened cycle life. Investigating the causes of dendrite nucleation and growth and subsequently proposing methods to inhibit dendrite growth will be crucial for realizing the commercial application of lithium metal batteries.

### 1.4 Model of dendrite growth

To mitigate the growth of dendrites during battery operation, it is crucial to comprehend the dendrite growth process of lithium. Various models for lithium dendrite nucleation and growth have been summarized in previous publications. While these models may not fully capture the intricacies of the nucleation and deposition process of metallic lithium dendrites and may even present some contradictions, they remain significant for understanding the formation process of metallic lithium dendrites. This does not hinder us from utilizing these models to comprehend the operational dynamics of metallic lithium electrodes and subsequently developing methods to inhibit the growth of lithium dendrites.

#### 1.4.1 Surface nucleation and diffusion models

Among various metal batteries, metallic lithium batteries are prone to dendritic lithium growth, while metallic magnesium batteries can achieve a relatively flat, dendrite-free morphology [72, 73]. Analyzing the crystal structures of lithium metal and magnesium metal can offer guiding strategies to inhibit dendrite growth. First principles calculations

reveal that the magnesium-magnesium bond is exceptionally strong (Figure 1.6), resulting in a higher difference in free energy between different dimensions of magnesium metal compared to lithium metal. Metallic magnesium is more inclined to form high-dimensional structures (such as two-dimensional and three-dimensional) on its surface rather than one-dimensional dendrites, indicating a reduced propensity for dendritic growth. Systematic analysis of different metals, including lithium, sodium, and magnesium, shows that metallic magnesium tends to be deposited uniformly in the surrounding area rather than gathering in a specific position to form dendrites. This suggests that magnesium has a relatively strong diffusion ability to the surrounding area. These factors contribute to metallic magnesium's tendency to form uniform deposits, while metallic lithium is more prone to dendritic growth due to its lower surface energy and higher diffusion barrier [74, 75].

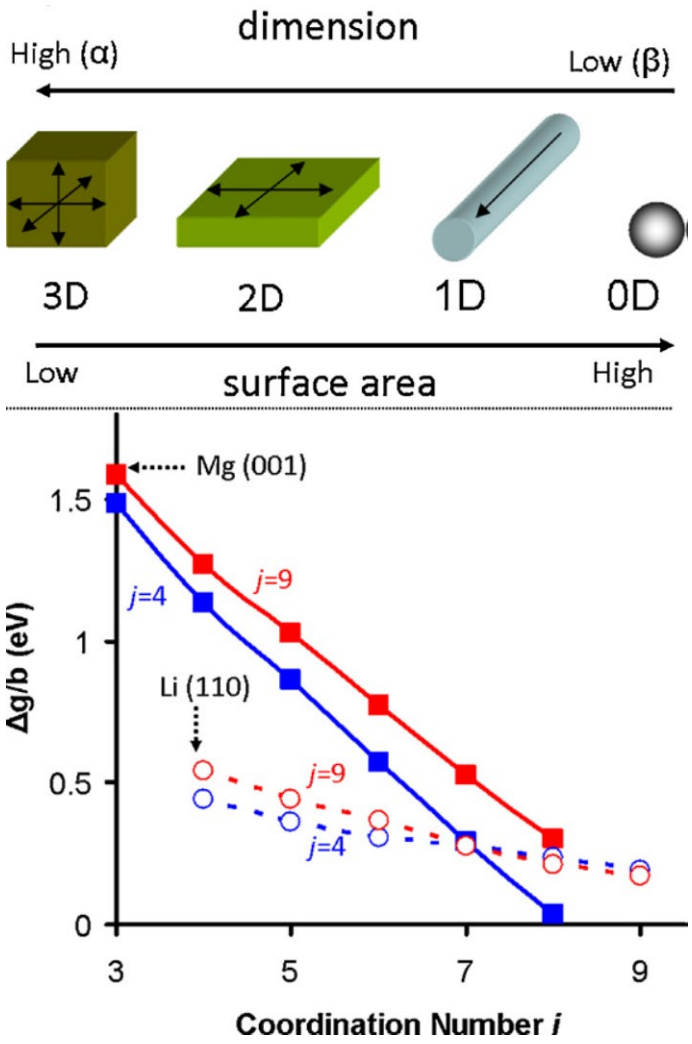


**Figure 1.6** The relationship between different dimensional morphology and surface energy of metallic materials [75].

Calculating and analyzing the surface energy of lithium hydroxide, oxide, and halogen compound materials can provide insights into the corresponding surface diffusion energy barrier. Lithium carbonate, with low surface energy and a high diffusion energy barrier, tends to gather lithium ions in specific areas, making it challenging to achieve a dendrite-free deposition morphology when used as the main component of the solid electrolyte interface (SEI) film (Figure 1.7) [76]. Conversely, metal halides have relatively high

surface energy and very low diffusion energy barriers. When used as the main component of the SEI film, they hold promise for achieving a dendrite-free deposition morphology. Therefore, considering surface energy and diffusion energy barriers offers a new perspective on understanding the causes of dendrite formation [77].

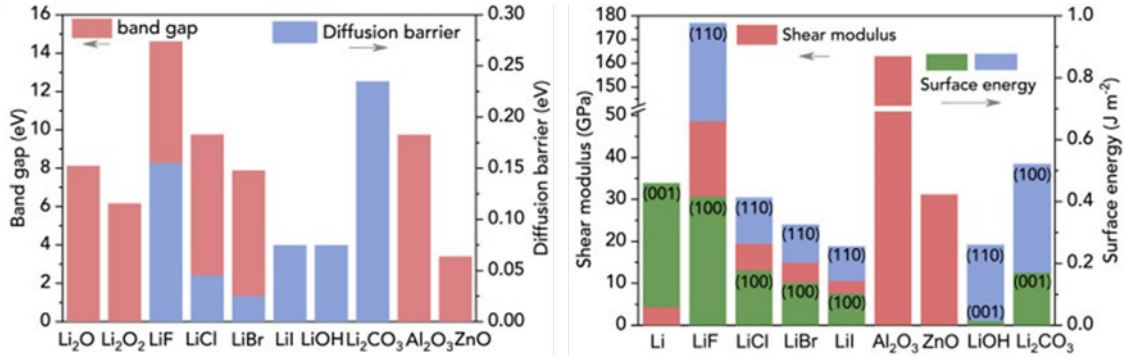


**Figure 1.7** $Li^+$ diffusion energy barrier and surface energy in different components of SEI [76].

### 1.4.2 heterogeneous nucleation model

In the initial stage of metallic lithium deposition, lithium ions gain electrons and are deposited on the current collector, resembling a heterogeneous nucleation process. The initial nucleation morphology plays a crucial role in determining the final lithium metal deposition morphology. Therefore, a thorough study of the heterogeneous nucleation behavior of metallic lithium anodes is essential.

The heterogeneous nucleation process comprises five stages: nucleation inhibition, long latency, short latency, early growth, and late growth [78, 79]. Nuclei formed during the nucleation inhibition stage are thermodynamically unstable and tend to dissolve back into the electrolyte. In the long latency period, thermodynamically stable crystal nuclei survive and grow amidst the fluctuations of the ion and electric fields. When the

electrode surpasses a certain overpotential, a short latency period ensues, leading to more uniform sizing of the lithium crystal nucleus. Under a specific overpotential, metallic lithium with a certain radius begins nucleating and growing (Figure 1.8). In subsequent early and late growth stages, thermodynamically and kinetically stable nuclei gradually grow to their final size. Once the lithium crystal nucleus forms, its growth becomes inevitable and unstoppable, underscoring the importance of inhibiting dendrite growth during the initial nucleation stage.

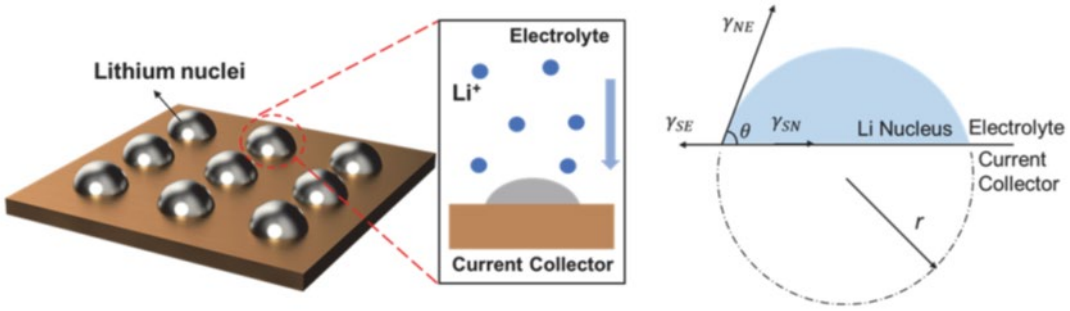


**Figure 1.8** Heterogeneous nucleation process of lithium metal [80].

Based on this model, strategies for suppressing dendrites can be inferred [80, 81]:

(a) Reduce the roughness of the metallic lithium anode surface to enhance smoothness and improve the uniformity of crystal nuclei during the incubation period.

(b) Design the anode's skeleton size to be smaller than the thermodynamically stable crystal nucleus size to prevent dendrite formation.

(c) Limit the overpotential of the negative electrode.

(d) Enhance the lithophilicity of the metallic lithium electrode.

The research team [82] from Stanford University explored the heterogeneous nucleation process of metallic lithium and investigated the effects of different matrices on the nucleation process (Figure 1.9). These matrices include those with solubility in metallic

lithium (e.g., Pt, Al, Mg, Zn, Ag, Au) and those insoluble in metallic lithium (e.g., Si, Sn, C, Ni, Cu) [83, 84]. When both types of matrices coexist on the current collector surface, lithium ions are more likely to be deposited on the surface of the first type, demonstrating a typical heterogeneous nucleation phenomenon of lithium metal. The nucleation behavior of metallic lithium in different matrices varies.

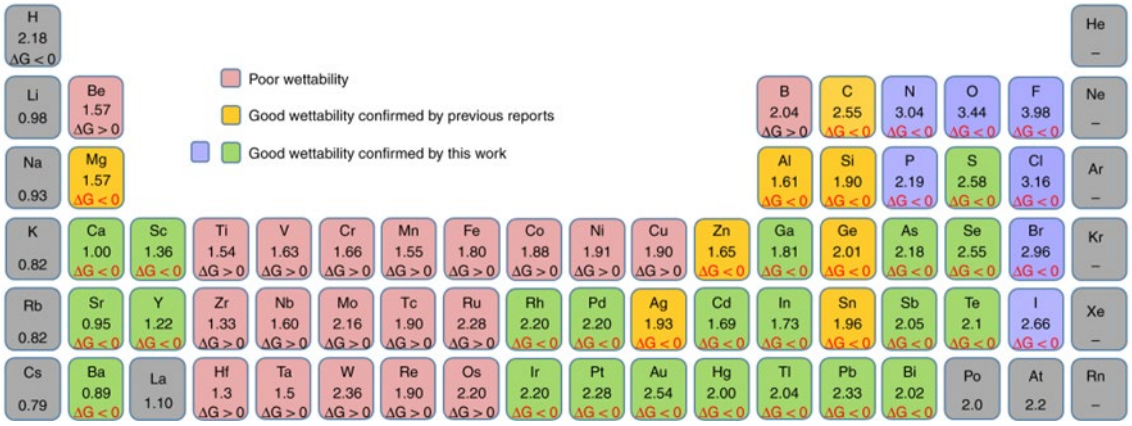


**Figure 1.9** Lithiophilic elements and lithiophobic elements [83].

### 1.4.3 SEI model

In liquid electrolytes, the Solid Electrolyte Interphase (SEI) is commonly observed on the surface of metallic lithium anodes [85, 86]. When holes develop on the SEI surface, lithium ions tend to accumulate near these openings, leading to the rapid deposition of a large number of lithium ions and eventually triggering dendrite growth. Apart from the physical hole structure causing dendrite growth, the properties of the SEI significantly impact the deposition behavior of lithium ions [87].

The lithium ion conductivity in metallic lithium batteries plays a crucial role in shaping the deposition morphology of metallic lithium. In contrast to the liquid phase diffusion control process in the main phase of the electrolyte, the short-range solid phase diffusion

process in the SEI influences the initial nucleation of lithium ions, thereby altering the final deposition morphology of metallic lithium [88]. Generally, the deposition and stripping behavior of lithium ions is highly dependent on the ionic conductivity in the SEI [89, 90]. The deposition process of lithium ions can be divided into four stages:

(1) Spherical lithium begins to appear on the lithium surface, and its length and diameter increase simultaneously. Since the transfer rate of lithium ions in the liquid phase diffusion process in the main phase of the electrolyte is much higher than the solid phase diffusion in the SEI, the control variable in the deposition process of lithium ions is mainly the diffusion rate of lithium ions in the SEI.

(2) Lithium deposits begin to grow from the surface of the lithium sheets and "push out" the lithium formed in the previous stage, causing the length of the deposits to increase. At this time, the diameter of the lithium deposit remains unchanged and the length increases rapidly.

(3) When the length of the growing dendrite reaches a certain value, it will pierce the SEI, and a new SEI layer will be formed on the surface of the newly grown lithium metal.

(4) Kink begins to appear on the surface of the dendrite, causing the dendrite to decompose into two parts: one part is the original dendrite, which does not change its length and diameter; the other part is the newly appeared dendrite, which keeps the original diameter unchanged, and the length continues to increase.

Li dendrites induced by the Solid Electrolyte Interphase (SEI) continually reduce the tip growth rate. This reduction occurs due to the continuous formation of SEI, which competes with the lithium ion deposition process. Additionally, the lower ion diffusion rate in SEI limits the growth rate of dendrites. At lower current densities, the diffusion

rate of lithium ions in the SEI is relatively fast, leading to simultaneous increases in the diameter and length of the lithium deposits [91]. This constitutes a surface growth process, forming a macroscopic and relatively dense lithium layer. Conversely, at high current densities, the electron transport speed is very fast, making the diffusion speed of lithium ions in the SEI the determining factor in the lithium deposition process. In this scenario, lithium only increases in the length direction while the diameter remains unchanged, resulting in the large-scale growth of dendrites [92, 93].

The crucial aspect of the lithium metal anode during battery charging and discharging is the SEI attached to its surface. This SEI has a decisive impact on the deposition of lithium ions. However, researchers currently lack comprehensive knowledge about the properties of this film structure, and a clear understanding of the impact of dendrites is yet to be achieved.

### 1.4.4 Sand's time model

In dilute solutions, Sand's time is commonly used to describe the initiation time of dendrite growth. When metallic lithium undergoes rapid charging and discharging in a dual-ion electrolyte, the cations are rapidly consumed, and at a certain moment, their ion concentration drops to zero [94, 95]. Shortly after, the strong negative electric field on the surface of the negative electrode adsorbs a large number of lithium ions, depositing them on the surface and rapidly forming dendrites [96]. Researchers define the time when metallic lithium dendrites begin to appear as Sand's time (T) and express it using physical parameters in the battery.

The Sand's time model incorporates the following variables [97, 98]:

$u_c$ and $u_a$: Migration numbers of cations and anions, respectively.

e: Electron charge.

J: Current density.

$Z_c$: Cation charge number.

$C_0$: Initial concentration of cations.

D: Diffusion factor.

$D_c$ and $D_a$: Diffusion coefficients of cations and anions, respectively.

The Sand's time model offers a quantitative method to comprehend the growth pattern of lithium dendrites, demonstrating that time T is inversely proportional to the square of J (current density).

### 1.5 Strategies to inhibit dendrite growth

Lithium metal anodes have been around for nearly seventy years, but researchers still don't know much about the process of lithium dendrite nucleation and growth. Although there is currently no model that can completely explain the formation of lithium dendrites, this does not hinder the exploration of methods to inhibit dendrite growth. Researchers can suppress dendrite growth under certain conditions, which provides many meaningful references for the safe and stable operation of lithium metal anodes.

#### 1.5.1 Electrolyte modification

During battery operation, electrons flow through the external circuit, while lithium ions move in the internal circuit. To facilitate ion transport between the positive and negative electrodes, an electrolyte layer must be introduced. However, lithium metal is generally unstable with most electrolytes. Ether-based DOL and DME electrolytes demonstrate greater stability compared to carbonate-based EC systems (Figure 1.10) [99]. While

lithium metal cannot persist stably with most electrolytes, the reaction product formed during the initial passivation process can effectively protect the surface of the negative electrode, preventing further reactions. As modifying the electrolyte doesn't necessitate significant changes in electrode and battery manufacturing processes, it proves to be economically feasible [100]. Consequently, extensive research has been conducted on electrolytes to identify the optimal composition.

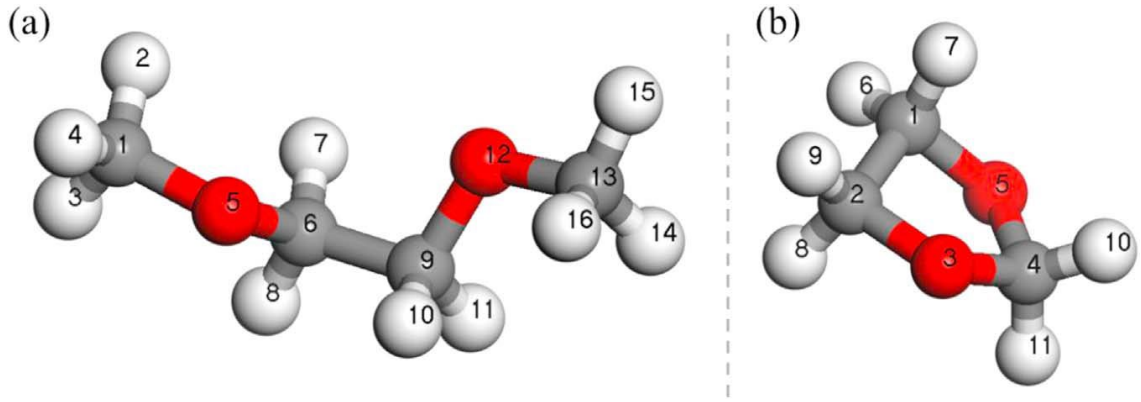


**Figure 1.10** Molecular orbital of DME (a) and DOL (b) electrolytes [99].

1.5.1.1 Additives to stabilize SEI

Many film-forming additives can react with lithium metal, creating a stable Solid Electrolyte Interphase (SEI) layer on its surface [101, 102]. This SEI layer acts as a protective shield for the lithium anode, exhibiting self-sacrificial properties. In commercial lithium-ion battery systems, additives designed to stabilize the SEI on graphite or silicon anodes have been extensively researched and prioritized [103, 104]. Common film-forming additives include FEC (fluoroethylene carbonate) [105], VC (vinylene carbonate) [106], and ES (ethylene sulfite) [107].

The SEI film on the lithium anode surface is influenced by dendrite growth, potentially making it less stable. Therefore, there's a need to explore suitable electrolyte additives to

enhance the stability of the lithium anode. Due to the high reactivity of lithium, it readily reacts with various lithium salts and organic solvents to form SEI. Effective film-forming additives are generally characterized by the following features: i) Lower LUMO energy level and higher HOMO energy level, enabling preferential reaction with metallic lithium. ii) The reaction product of the additive and metallic lithium should exhibit good chemical and electrochemical stability, along with electronic insulation and ion conduction properties. iii) The formed SEI should maintain a dense and continuous structure.

Given high Young's modulus (~64.9 GPa) and electronic insulation properties ($10^{-31}$ $S \cdot cm^{-1}$), LiF aligns well with the requirements for reaction products [108, 109]. Therefore, selecting fluorine-containing additives can effectively build a LiF-rich SEI on the surface of lithium metal, inhibiting the growth of lithium dendrites.

In a study conducted by Zhang et al., 5% (w) FEC was added to the 1.0 $mol \cdot L^{-1}$ LiPF6-EC/DEC electrolyte system to protect the lithium metal anode [110], as depicted in Figure 1.11. FEC, with a lower LUMO energy level of -0.87 eV compared to EC (-0.38 eV) and DEC (0 eV), can preferentially react with lithium metal to generate a LiF-rich Solid Electrolyte Interphase (SEI), enabling uniform deposition of lithium ions. The research findings indicate that the Li||Cu battery system's Coulombic efficiency, with 5% (w) FEC added at a current density of 0.1 mA $cm^{-2}$ and a capacity of 0.5 mAh $cm^{-2}$, can still be maintained at around 98% after 100 cycles. In contrast, the Coulombic efficiency of the electrolyte system without FEC addition is only maintained at 92%. When forming a full battery using the ternary cathode material $LiNi_{0.5}Co_{0.2}Mn_{0.3}O_2$ (NCM523) and metallic lithium, with a NCM523 load capacity of 12 mg $cm^{-2}$, the full battery with 5% (w) FEC added can achieve a current density of 180 mA $g^{-1}$ and cycle stably for 100

cycles. In contrast, the system without FEC experiences abrupt capacity fading around 50 cycles. This phenomenon is attributed to the continuous growth of lithium dendrites and the accumulation of dead lithium, leading to battery failure.

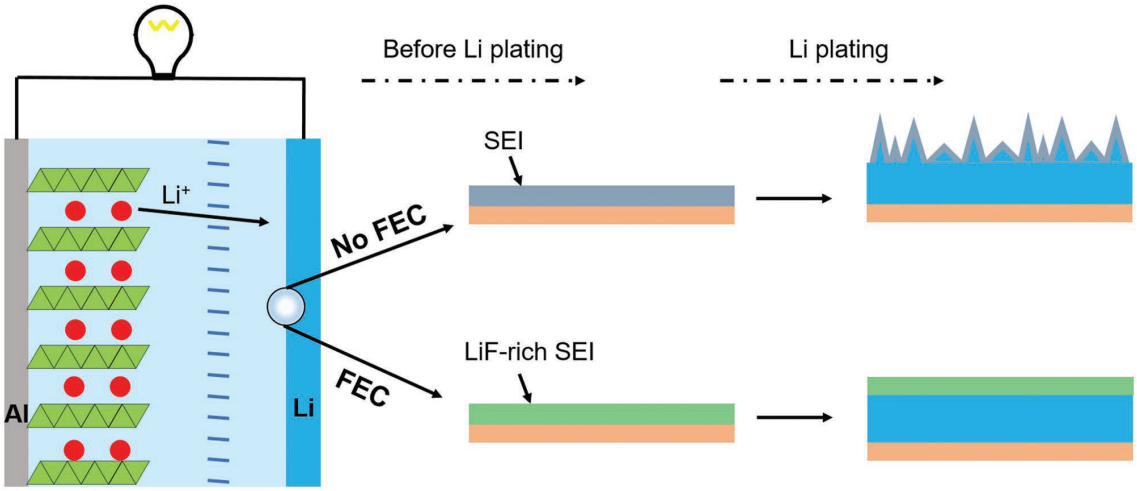


**Figure 1.11** Effects of presence and absence of FEC additives on lithium metal [110].

$LiNO_3$ is commonly used as an ether electrolyte additive in lithium-sulfur battery systems to inhibit the shuttle of polysulfides and the growth of lithium dendrites [111-113]. However, $LiNO_3$ is insoluble in carbonate solvents, and ester solvent systems are generally used for high-voltage lithium metal batteries [114]. To address this challenge, Yan et al [115]. explored the solvation chemistry of $LiNO_3$ in ester electrolytes and found that adding a trace amount of $CuF_2$ can promote the dissolution of $LiNO_3$ in the EC/DEC electrolyte system. The addition of $LiNO_3$ to the electrolyte system results in the generation of nitrogen-containing inorganic products ($Li_3N$ and $LiN_xO_y$) on the surface of the Li negative electrode in the battery. These products regulate the nucleation process of lithium and guide the uniform deposition of lithium. When combined with FEC in the DME electrolyte system, FEC and $LiNO_3$ form an ether/ester cosolvent electrolyte system, solving the issue of $LiNO_3$ being insoluble in FEC [116]. The joint action of FEC

and $LiNO_3$ results in the formation of a stable lithium anode Solid Electrolyte Interphase (SEI) that includes products such as LiF, $Li_3N$, and $LiN_xO_y$. These products constitute a stable SEI and guide the uniform deposition of lithium ions. As shown in Figure 1.12, when using the FEC/$LiNO_3$ system and depositing it for half an hour at a current density of 1.0 mA $cm^{-2}$, the cross-sectional structure of lithium metal remains flat. In contrast, the EC/DEC electrolyte system generates a large amount of dendrite lithium. The FEC/$LiNO^3$ electrolyte system also exhibits more stable full battery cycle performance in button and soft pack batteries. Additionally, there are other additive systems containing F, N, S, B, and other elements used to stabilize the SEI membrane structure, such as $LiAsF_6$ [117], LiBOB (lithium bisoxalate borate) [118], LiDFOB (lithium difluoroxalate borate) [119], LiPS (poly) lithium sulfide) [120], $H_3BO_3$ [121], etc.

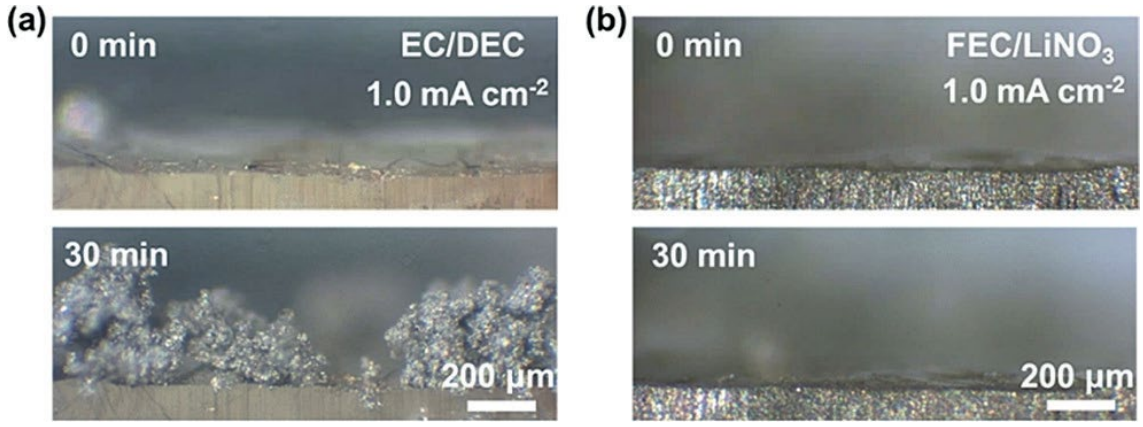


**Figure 1.12** Observations of lithium deposition processes using optical microscopy in two different electrolytes: EC/DEC (a) and FEC/$LiNO_3$ (b) [116].

1.5.1.2 Additives for Lithium Deposition

In addition to film-forming additives that react with metallic lithium to form a stable Solid Electrolyte Interphase (SEI), another type of additive controls the deposition behavior of lithium ions through charge induction to inhibit the growth of lithium

dendrites. As shown in Figure 1.13, Ding et al [122]. used $CsPF_6$ as an additive to induce the lithium deposition process through charge induction. According to the Nernst equation, when the concentration of $Cs^+$ is low, its reduction potential will be lower than that of $Li^+$. When the negative electrode external voltage (Va) is between the reduction potential of $Li^+$ and the reduction potential of low-concentration $Cs^+$ (i.e., $E_{Li+/Li} > V_a > E_{Cs+/Cs}$), $Cs^+$ will be attracted to the surface of the protruding lithium nuclei. Other $Li^+$ will be deposited at non-protruding positions under the interaction of charged particles, inducing uniform deposition of $Li^+$. Research shows that the surface of the lithium anode without adding $CsPF_6$ generates a large number of lithium dendrites after Li is deposited. In contrast, the surface of the lithium anode that adds 0.05 mol $L^{-1}$ $CsPF_6$ is very smooth and flat after depositing Li, indicating that the $CsPF_6$ additive can effectively regulate $Li^+$ deposition behavior [123]. This self-healing strategy through electric fields has been further proven to be able to effectively regulate the lithium deposition morphology and improve the performance of lithium metal batteries [124].

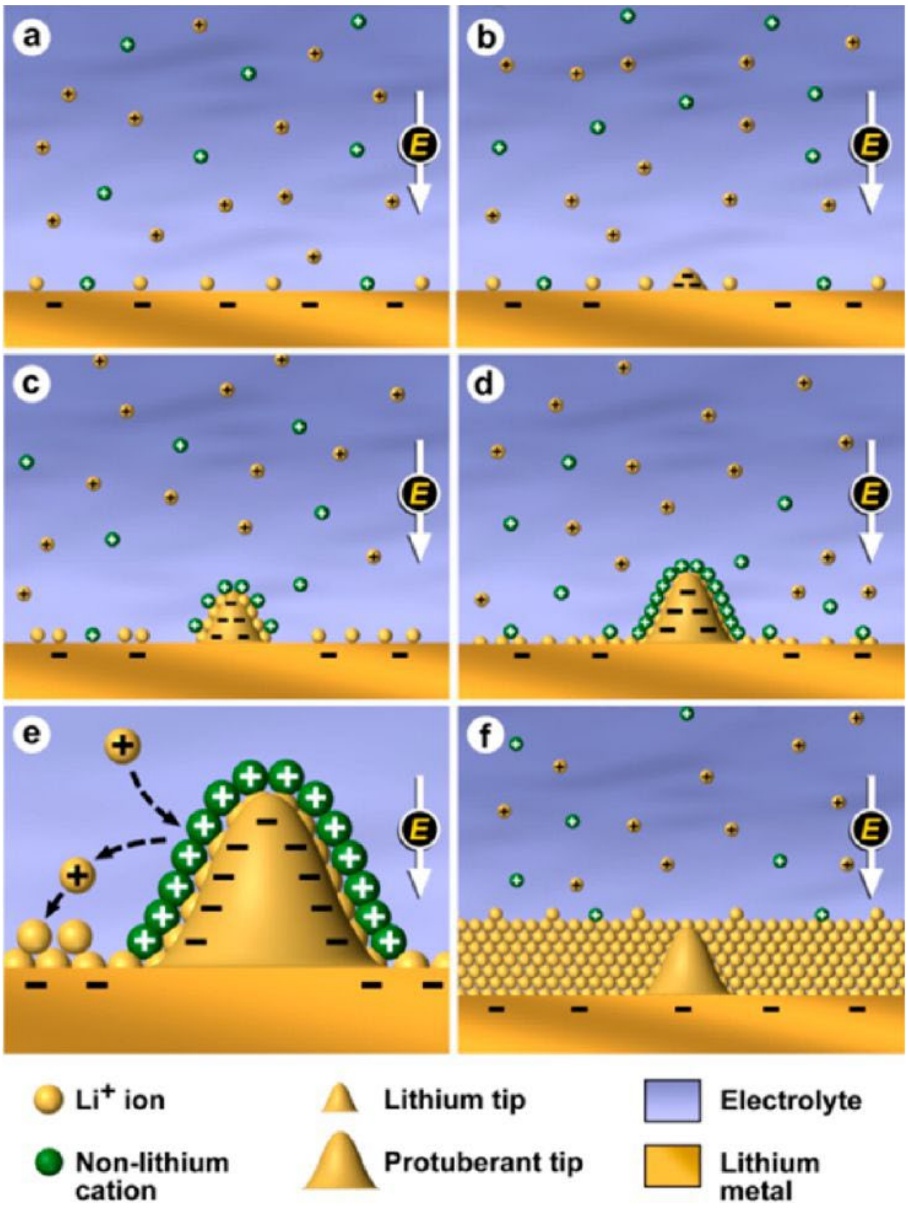


**Figure 1.13** Regulations of lithium deposition process based on Self-Healing Electrostatic Shield mechanism [122].

Ye et al [125]. reported the use of $AlCl_3$ as an electrolyte additive to inhibit the growth of lithium dendrites. $AlCl_3$ reacts with trace amounts of water in the electrolyte to form $Al(OH)_3$ colloidal particles. Additional $Al^{3+}$ is adsorbed on the surface of the particles, making them positively charged. Following the charge-induced model, these charged

particles can regulate the deposition behavior of lithium. Cheng et al. used nanodiamond as an additive to regulate $Li^+$ deposition. Through Density Functional Theory (DFT) calculations, they found that nanodiamond has the lowest $Li^+$ diffusion energy barrier on the (110) surface and a surface with higher adsorption energy for $Li^+$. During the lithium deposition process, $Li^+$ can be adsorbed on the surface of nanodiamond particles, serving as nucleation sites for uniform nucleation. The research results show that the lithium deposition morphology forms a dense array rather than dendrites, indicating that nanodiamonds, with their high surface energy and low diffusion energy barrier, are more likely to induce the uniform nucleation and growth process of lithium.

### 1.5.2 Artificial SEI improves lithium metal anode

The Solid Electrolyte Interface (SEI) formed on the surface of the lithium negative electrode in lithium metal batteries acts as a passivation film resulting from the reaction between the active lithium electrode and the organic electrolyte. It consists of inorganic layers, including $Li_2CO_3$, LiOH, $Li_2O$, LiF, and organic layers like $ROCO_2Li$ and ROLi. The complexity and uncontrollability of the in-situ generated SEI in the electrolyte can lead to an uneven SEI structure and surface defects, causing uneven lithium deposition. The growth of lithium dendrites further disrupts the SEI structure, escalating battery polarization and posing safety concerns such as thermal runaway [126-128]. Therefore, creating a uniform and stable artificial SEI layer with ion conduction and electronic insulation on the surface of metallic lithium before use is a viable strategy for protecting the lithium anode [129-132]. As discussed in the electrolyte section, LiF has the ability to passivate the SEI film and inhibit the growth of lithium dendrites. Designing a stable LiF-rich artificial SEI on the surface of metallic lithium proves to be an effective means of

safeguarding the lithium anode. Zhao et al [133]. demonstrated a method where the fluorine-containing organic compound CYTOP was heated at 350 °C to produce fluorine gas ($F_2$) (Figure 1.14). This $F_2$ then reacted with metallic lithium for 12 hours, resulting in a LiF protective layer approximately 380 nm thick on the lithium surface. A symmetrical battery with the LiF-protected lithium anode exhibited stable cycling for 300 cycles at a current density of 1 mA $cm^{-2}$ and a deplating capacity of 1 mAh $cm^{-2}$, maintaining a stable lithium anode without dendrite formation. Researchers have explored other fluorine-containing compounds like $CuF_2$ [133], $AlF_3$ [134], $NiF_2$ [135], $SbF_3$ [136], $BF_3 \cdot H_2O$ [137] to construct LiF-containing protective layers on the lithium anode surface. Liang et al. [138] used a sequential reaction of a tetrahydrofuran solution of metal chloride $MCl_x$ (M = In, Zn, Bi, As) and metal lithium to generate LiCl and $Li_xM$ alloy layers. This inhibits dendrite formation, as LiCl acts as an electronically insulating layer preventing $Li^+$ reduction to Li metal on the surface, while the high ion conductivity alloy lithium compound $Li_xM$ promotes rapid $Li^+$ migration to the alloy layer, subsequently being reduced to Li metal on the lithium surface. In a full battery composed of $Li_4Ti_5O_{12}$, the lithium anode with $Li_xM$/LiCl protective layer exhibited more stable long-term cycle performance than the pure lithium anode. This presents a promising avenue for protecting lithium anodes through artificial SEI construction.

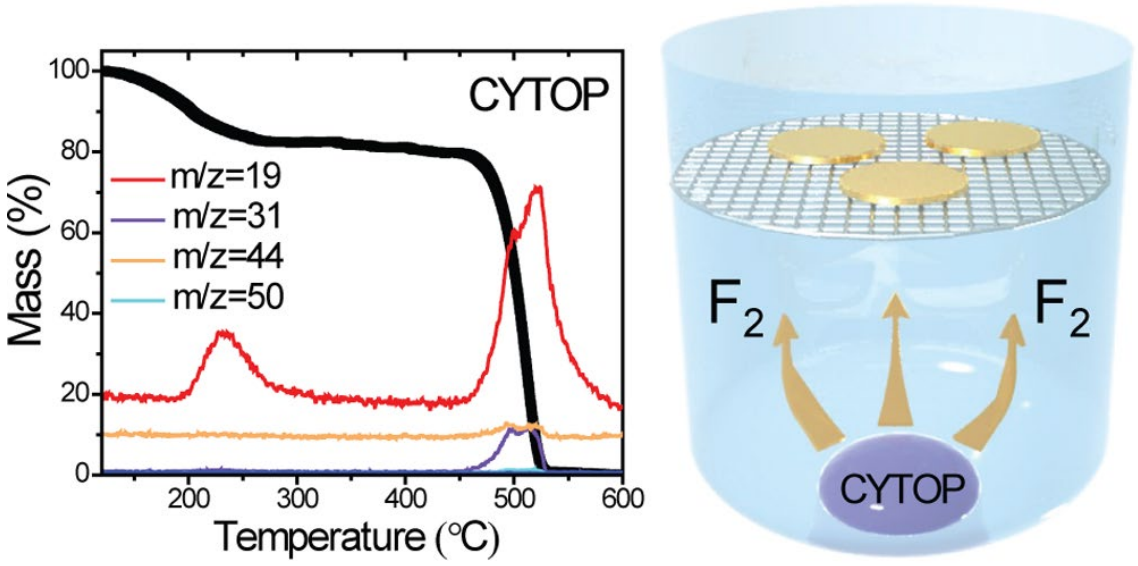


**Figure 1.14** Formation of LiF protective layer [132].

Apart from lithium halides in main group VII, compounds formed by main group VI elements and lithium also exhibit good ionic conductivity and provide effective protection for the lithium anode [139-141]. Chen et al [142]. demonstrated the synthesis of a high ion conductivity $Li_2S$ (~$10^{-5}$ S·$cm^{-1}$) inorganic protective layer on the lithium surface by heating elemental sulfur at 240 °C and reacting it with metallic lithium for 24 hours (Figure 1.15). The $Li_2S$-protected lithium anode in a symmetrical battery exhibited stable cycling for 750 hours at a current density of 1 mA $cm^{-2}$ and a deplating capacity of 1 mAh $cm^{-2}$, with only a slight increase in polarization voltage from the initial 60 mV to 90 mV. The $Li_2S$@Li electrode applied in lithium metal full batteries with LFP and LTO as positive electrodes maintained better rate performance and cycle performance compared to pure lithium negative electrodes, which suffered from capacity decline due to dendrite growth issues. Building on the $Li_2S$ design strategy, Liu et al. [143] utilized a low-boiling-point solid solution compound $SeS_2$ (~118 °C) as a gas evaporation precursor. The generated selenium sulfide gas reacted with metallic lithium to form a $Li_2S$/$Li_2Se$

mixed protective layer. Since Se and S belong to the same main group and have larger radii than S, DFT calculations revealed that $Li_2Se$ has a lower ion migration energy barrier than $Li_2S$, enhancing the ion conductivity of the $Li_2S$ system. This $Li_2S/Li_2Se$ mixed protective layer exhibited excellent electrochemical cycle performance when used in symmetrical batteries, LFP, NCM622, and Li-S full cells. In addition to the mentioned inorganic protective layers, various inorganic artificial SEIs such as $GeCl_4$ [144], $MoS_2$ [145], $Al_2O_3$ [146], $Li_3PO_4$ [147], $Li_xSi$ [148], Mg [149, 150], Sn [151], etc. have been extensively studied for protecting lithium metal anodes.

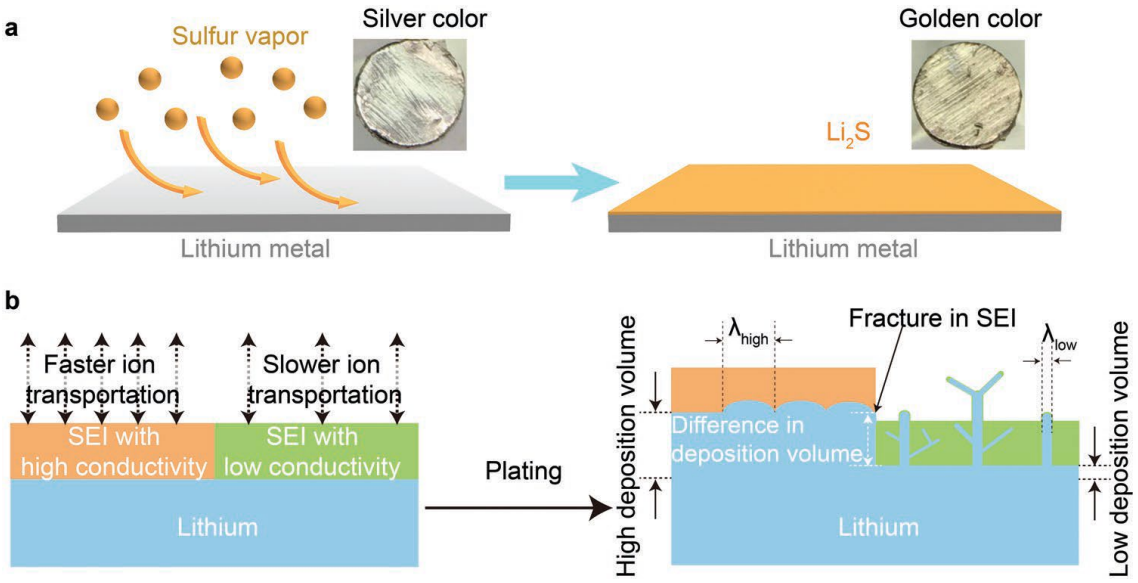


**Figure 1.15** Synthesis and mechanism of lithium-sulfur protective layer [142].

Organic polymers are gaining attention as promising materials for stabilizing the solid-liquid interface layer of lithium anodes due to their high toughness and mechanical stability. Li et al. [152] demonstrated the construction of an elastic PAA (polyacrylic acid) protective layer on the surface of metallic lithium (Figure 1.16). In situ reaction between metal lithium and polyacrylic acid produced lithium polyacrylate (LiPAA). The migration of lithium ions occurred through the chain segment migration of Li-containing

polymer. The LiPAA SEI layer not only prevented side reactions between metallic lithium and the electrolyte but also adaptively adjusted the stress of lithium dendrites on the SEI layer, enabling the uniform deposition of metallic lithium under the SEI layer. Research findings indicated that in a symmetrical battery, the Li@LiPAA electrode achieved a stable deplating cycle of 700 hours under the conditions of a current density of 0.5 mA $cm^{-2}$ and a capacity of 1 mAh $cm^{-2}$. Furthermore, it maintained stable cycling performance in the LFP full battery. Additionally, polymers used in artificial SEIs for lithium anodes include PVDF-HFP [153] (polyvinylidene fluoride-hexafluoropropylene), highly polarized β-PVDF [154], PDMS (polydimethylsiloxane) [90], PEO (polyepoxyethane) [155], and other systems.

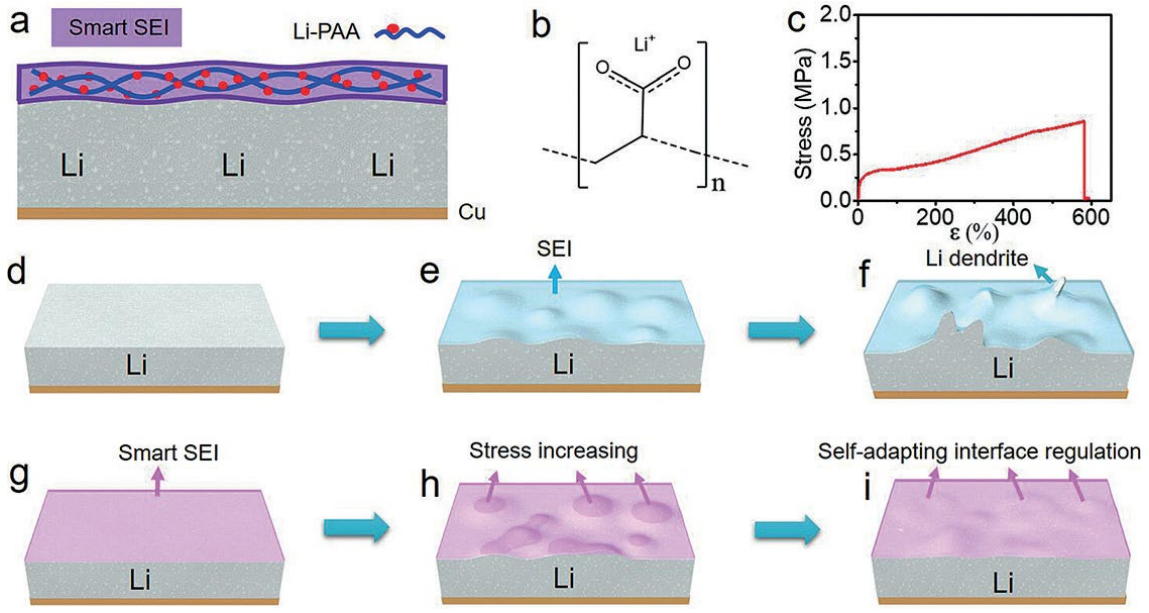


**Figure 1.16** The process of Li-PAA protecting lithium anode [152].

When the ionic conductivity of a pure organic polymer system reaches its limit, combining the advantages of inorganics and organic polymers becomes essential to prepare an artificial SEI layer with both high ionic conductivity and toughness. Liu et al.

[92] synthesized nanoscale $Cu_3N$ particles through a solution method, dissolved the $Cu_3N$ particles and the organic polymer SBR (styrene-butadiene rubber) in THF (tetrahydrofuran) to create a uniform solution system, and coated the mixed solution system on the surface of lithium metal. In situ, $Cu_3N$ nanoparticles reacted with metallic lithium to form $Li_3N$ ($\sim 10^{-3}$ – $10^{-4}$ S $cm^{-1}$) particles with high ionic conductivity. This artificial SEI combines the high ionic conductivity and toughness of SBR polymers. When $Cu_3N$/SBR is applied to the Li‖Cu battery system, stable lithium deplating cycles were achieved for 100 cycles under a current density of 1 mA $cm^{-2}$ and a lithium plating capacity of 1 mAh $cm^{-2}$ in its ester electrolyte system. The Coulombic efficiency was maintained at 97.4%, representing a significant improvement compared to the rapid decay trend of a pure lithium anode. Additionally, organic/inorganic hybrid protective layers used to protect lithium anodes include PEO/$TiO_2$, PMMA (polymethylmethacrylate)/$SiO_2$, PEDOT-co-PEG (poly3,4-ethylenedioxythiophene monomer- Polyethylene glycol)/$AlF_3$, etc.

The implementation of the artificial SEI strategy has significantly enhanced the protection of lithium metal. However, in high lithium utilization battery systems, there is a need to enhance the ion conductivity and structural stability of the artificial SEI. Researchers must persist in developing advanced protection strategies and delve into their intrinsic mechanisms to achieve the full potential of high-specific-energy lithium metal batteries.

### 1.5.3 Modified separator protects lithium metal anode

The separator in lithium secondary batteries serves the crucial role of preventing contact between positive and negative electrodes, thus averting short circuits. While allowing

solvated lithium ions to pass through, it restricts the conduction of electrons. In lithium metal batteries, the penetration of lithium dendrites through the separator can bridge the positive and negative poles, leading to safety hazards like short circuits and fires. Given the intimate contact between the separator and lithium anode, researchers modify commercial separators with inorganic or organic materials to enhance resistance to dendrite stress and regulate dendrite growth. Notably, Liu et al [156]. altered the functionalized carbon layer on the separator's negative end to alter the growth direction of lithium dendrites and impede further expansion (Figure 1.17). The top potential (φt) of the lithium dendrite exceeds the lithium surface potential (φs) at the bottom [157]. The sharper the dendrite, the greater the potential difference between the top and surface, acting as the driving force for dendrite growth. As lithium dendrites grow, they can breach the separator, leading to the release of significant dead lithium. The functionalized nanocarbon layer, modified with para-benzenesulfonic acid (pb-$SO_3H$), undergoes immersion in $LiNO_3$ solution to adsorb lithium ions, forming pb-$SO_3Li$. Subsequently, the lithium-containing functionalized carbon layer is applied to the separator. The physical contact between the functionalized carbon layer and lithium metal, resulting in the same potential, causes lithium dendrites to grow from both surfaces during the charging process. When dendrites at both ends touch, the potential difference becomes zero, halting the driving force for further dendrite growth. Subsequent lithium is uniformly deposited between the carbon layer and lithium metal. Research findings reveal a uniform lithium layer on the separator's surface instead of dendritic lithium. When this functionalized carbon layer is incorporated into the Li||LFP full battery, it demonstrates stable cycling and a consistent polarity voltage value for over 800 cycles. In

contrast, the ordinary diaphragm system experiences rapid capacity decay, occurring near 220 cycles.

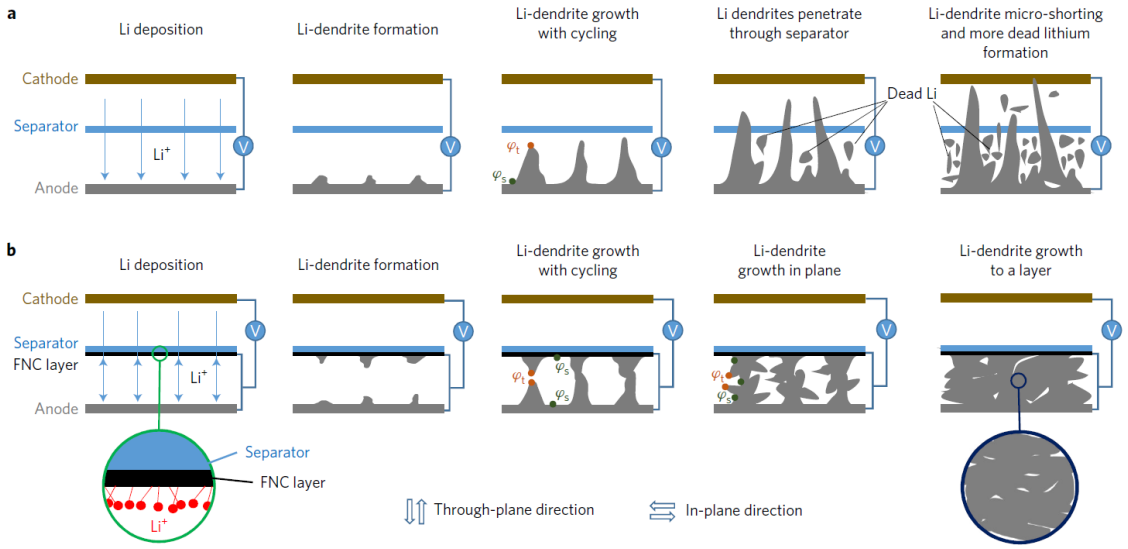


**Figure 1.17** Effects of traditional separators and FNC-modified separators on lithium dendrites [156].

Li et al. [158] innovatively utilized graphene oxide (GO) and polyacrylamide (PAM) for copolymerization, resulting in a porous two-dimensional molecular brush structure material known as GO-g-PAM. This material was applied as a coating on the surface of the PP separator to finely regulate the deposition of lithium ions. The two-dimensional structure of GO facilitates swift lithium-ion transport in the electrolyte. Meanwhile, the C=O and N-H functional groups in PAM play a crucial role in adsorbing lithium ions and evenly distributing them at the molecular level. This ensures the dispersion of lithium ions on the surface of the current collector, effectively suppressing the growth of lithium dendrites. Research findings demonstrate that the GO-g-PAM modified PP separator, when employed in a Li‖Cu battery system, maintains a stable Coulombic efficiency of 98% under a current density of 1 mA $cm^{-2}$ and lithium plating capacity of 1mAh $cm^{-2}$, even

after 150 cycles. Both the surface and cross-section of the lithium metal exhibit a stable and smooth structure, with no signs of lithium dendrites or dead lithium. Additionally, to achieve a stable and high-energy-density lithium-sulfur battery system, inorganic materials such as BN [159], MOF [160], N-graphene [161], and PAN fibers [162] are employed to modify the separator. These materials serve the dual purpose of regulating lithium ion deposition and inhibiting the growth of lithium dendrites, while also mitigating the shuttle effect of polysulfides in the sulfur cathode. This comprehensive approach ensures the development of a high-energy-density lithium-sulfur battery with enhanced safety and stability. However, it is crucial to acknowledge the challenges associated with modifying the separator to protect the lithium anode. For instance, an increase in separator thickness may lead to a reduction in battery energy density, longer diffusion paths for lithium ions in the solution system, increased impedance, and elevated polarization voltage. Therefore, it is imperative to judiciously design the thickness and chemical composition of the modification layer to strike a balance between protection and performance.

### 1.5.4 Solid state electrolyte

In addition to optimizing and enhancing the electrolyte, the incorporation of solid-state electrolytes (SSEs) presents a viable strategy to address inherent issues associated with lithium metal anodes. SSEs typically exhibit superior mechanical strength and a higher Li+ migration number, effectively impeding the growth of lithium dendrites. Furthermore, batteries utilizing SSEs offer advantages over those with liquid electrolytes, including prevention of safety concerns such as electrolyte leakage, poor chemical stability, and high flammability [163]. Additionally, the challenges posed by the shuttle effect,

stemming from soluble discharge intermediates (such as polysulfides and $O_2^-$) in lithium-sulfur or lithium-air batteries, can be completely circumvented. To ensure optimal electrochemical performance in solid-state lithium batteries, solid-state electrolytes must possess key attributes, including electronic insulation, low ion-specific area resistance, high thermal stability and safety, robust mechanical strength, electrochemical compatibility with lithium anodes, and minimal interface impedance between the two electrodes. Currently, solid electrolyte materials for lithium batteries primarily fall into two categories: inorganic solid electrolytes (ICEs) and polymer solid electrolytes (SPEs) [164].

Polymer Solid Electrolytes (SPEs) generally exhibit good flexibility and low contact resistance with electrode materials. However, they possess low strength and are susceptible to penetration by lithium dendrites. On the other hand, Inorganic Solid Electrolytes (ICEs) have poor contact with electrode materials but boast high hardness, effectively impeding the continued growth of lithium dendrites. To leverage the advantages of both types, Duan et al. [165] pioneered the design of an Asymmetric All-Solid Electrolyte structure (ASE). In their innovative approach, a 25 μm celgard separator serves as the electrolyte carrier (Figure 1.18). They incorporated a 5.4 μm thick PEGMEA polymer electrolyte layer (polyethylene glycol methacrylate) on the cathode material surface. Additionally, a dense $Li_7La_3Zr_2O_{12}$ (LLZO) layer with a thickness of 5.6 μm was designed on the lithium metal surface. The total thickness of the ASE was carefully controlled at 36 μm. A lithium symmetric battery constructed with ASE demonstrated a 3200 hour detachment and lithium plating cycle at a current density of 0.1 mA $cm^{-2}$ and 100%, respectively. Moreover, in a Li/ASE/LFP full cell, the battery

exhibited stable cycling for 120 cycles while maintaining a high Coulombic efficiency of 99.8%.

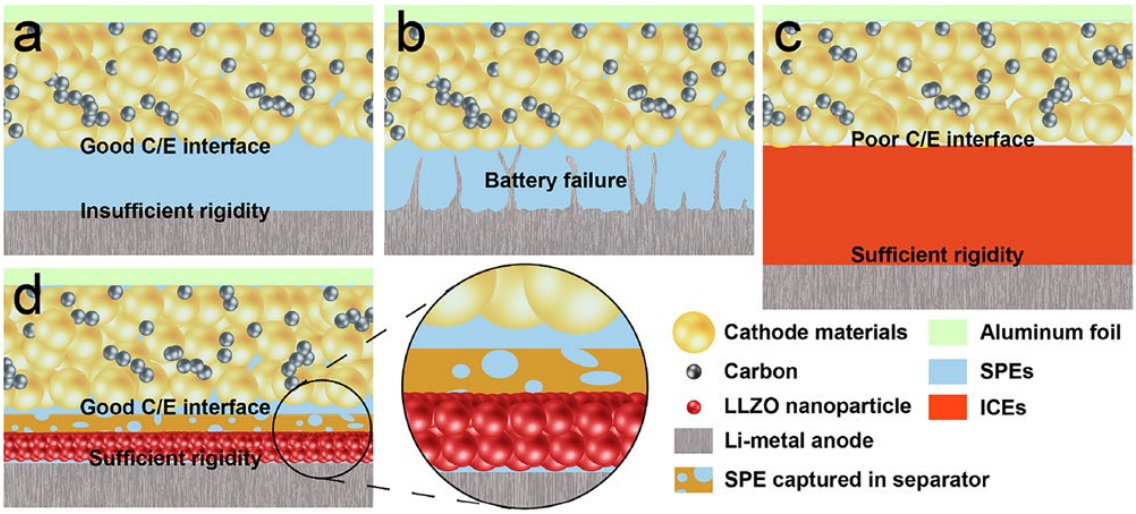


**Figure 1.18** Schematic diagram of solid-state lithium metal batteries using SPEs, ICEs and ASE as electrolyte [165].

Nevertheless, the contact resistance between metallic lithium and the solid electrolyte is relatively high, leading to the generation of lithium dendrites, especially at high current densities where the elevated interface contact resistance significantly increases battery polarization. To address this challenge, Duan [166] introduced an appropriate amount of graphite additive to molten metal lithium, creating a Li-C composite. The molten Li-C composite exhibited lower fluidity and higher viscosity compared to pure lithium, as depicted in Figure 1.19. Subsequently, the molten Li-C negative electrode was coated onto the pomegranate-type inorganic ceramic solid electrolyte $Li_{6.5}La_3Zr_{1.5}Ta_{0.5}O_{12}$ (LLZTO), establishing a uniform and stable Li-C/LLZTO interface. Research revealed that LLZO exhibited better compatibility with Li-C composites, allowing molten Li-C composites to be well adsorbed on the surface of LLZTO. In contrast, molten Li had

difficulty spontaneously adsorbing on LLZTO. Cross-sectional structure analysis indicated close contact between the Li-C electrode and LLZTO electrolyte, resulting in an interface impedance of 11 Ω $cm^2$. Conversely, there were micron-sized gaps between the Li electrode and LLZTO, leading to a high interface impedance of 381 Ω $cm^2$. Leveraging this stable interface, the Li-C/LLZTO/Li-C symmetric battery demonstrated stable cycling for 250 hours at a current density of 0.3mA $cm^{-2}$. When Li-C/LLZTO and LFP formed a full battery, it cycled steadily for 250 hours at 0.5 mA $cm^{-2}$, comparable to the performance in the liquid electrolyte system. However, when employing a pure lithium anode, the full battery capacity rapidly decayed to zero.

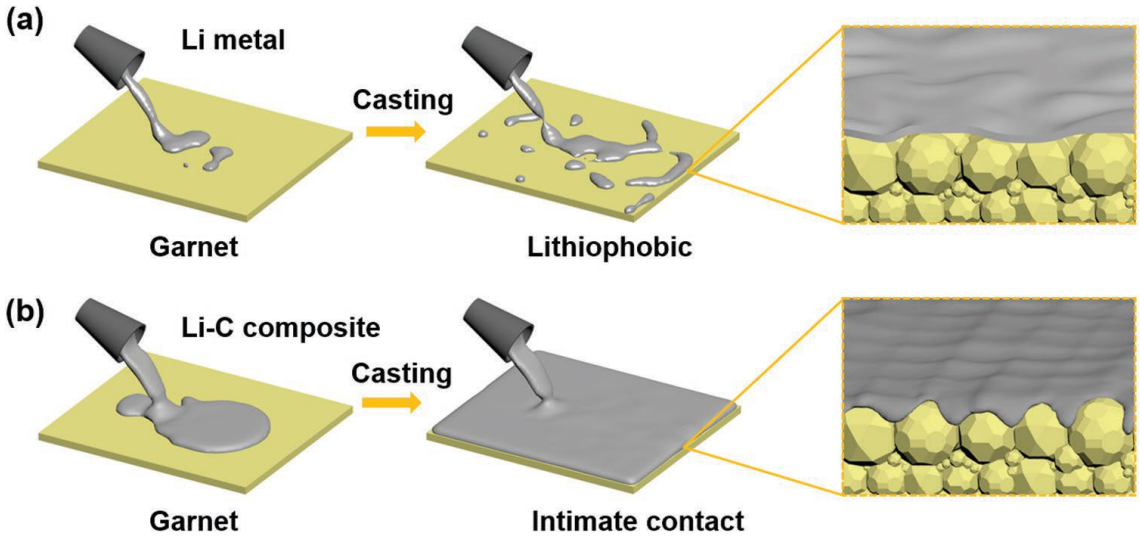


**Figure 1.19** Schematic diagram of coating Li-C composite anode electrode on LLZO solid electrolyte [166].

To control lithium ion deposition behavior at the lithium/electrolyte interface in an all-solid-state battery system, Zhao et al. [167] incorporated Al-doped $Li_{6.75}La_3Zr_{1.75}Ta_{0.25}O_{12}$ (Al-LLZTO) powder into a polymer system containing dissolved lithium salts (PEO/LiTFSI). This mixture was evenly dispersed, coated on a

polytetrafluoroethylene plate, and dried to form a uniform polymer-inorganic solid electrolyte film (PLL). Al-LLZTO, with its high ionic conductivity, and the addition of particles reducing the crystallinity of the PEO polymer, resulted in PLL exhibiting exceptional ionic conductivity at 25 °C ($1.12 \times 10^{-5}$ S $cm^{-1}$) and a cationic migration number $t_+$ of 0.58, surpassing PEO/LiTFSI ($t_+ = 0.37$), 1 mol $L^{-1}$ LiPF6-EC/DEC ($t_+ = 0.22$), and 1mol $L^{-1}$ LiTFSI-DME ($t_+ = 0.21$). The $TFSI^-$ anions were effectively fixed by the polymer matrix and inorganic filler particles, uniformly distributing space charges and lithium ions at the interface, inducing a consistent deposition of lithium with a smoother, non-dendritic morphology compared to the liquid system.

Stabilizing the interface between the lithium anode and electrolyte primarily involves two key approaches: First, the addition of compounds to enhance the lithium metal electrode, establishing a Li/electrolyte interface characterized by rapid ion transport and low resistance; second, the modification of solid electrolytes to enhance lithophilicity and regulate the deposition behavior of lithium ions. Despite these advancements, the practical implementation of solid-state lithium metal batteries at high current densities remains challenging, necessitating further efforts in constructing a stable solid-solid interface and advancing electrolyte materials.

### 1.5.5 Current collector

The current collector acts as the foundation for the deposition and stripping of metallic lithium, with its surface properties and structure significantly influencing the cycle stability of the lithium anode. Purposeful adjustments to the current collector interface and structure can efficiently control the electrodeposition of metallic lithium, paving the

way for the widespread implementation of metallic lithium anodes in high-energy-density battery systems.

1.5.5.1 Lithiophilic treatment

At low potential, the formation of a lithium-embedded alloy between metallic lithium and copper is challenging due to poor affinity between the two. As a result, copper is commonly used as the negative electrode current collector material in lithium-ion batteries [168]. In lithium metal batteries, lithium ions gain electrons on the surface of the copper current collector, leading to their reduction and the generation of lithium atoms. Without the induction effect of heterogeneous nucleation, these lithium atoms are prone to nucleate and grow uncontrollably in the form of dendrites [150]. Yan et al. from Stanford University investigated the nucleation modes of lithium on different metal substrates, revealing that the lithium deposition morphology depends on the choice of substrate. Copper current collectors exhibit a significantly greater nucleation overpotential compared to other lithiophilic substrates. Leveraging the affinity of metallic lithium on different substrates, a design incorporating gold nanoparticle-modified hollow carbon spheres was introduced. Studies demonstrated a high recycling Coulombic efficiency of metallic lithium in the hollow carbon sphere, reaching 98%, and stable cycling for 300 cycles. Moreover, researchers have undertaken lithiophilic modifications on copper current collectors to induce uniform nucleation and growth of metallic lithium, thereby inhibiting lithium dendrites. Stan et al. [169] employed magnetron sputtering technology to create lithiophilic zinc and gold modified layers on traditional copper current collectors (Figure 1.20). These layers, forming lithium-zinc and lithium-gold alloys during metallic lithium deposition, act as inducers and homogenizers, facilitating

nucleation and electrodissolution. Wet chemistry methods have also been utilized to prepare lithiophilic zinc, gold, silver, indium, etc., on the surface of copper current collectors, achieving a modified layer that promotes the uniform electrodeposition of metallic lithium [170-173].

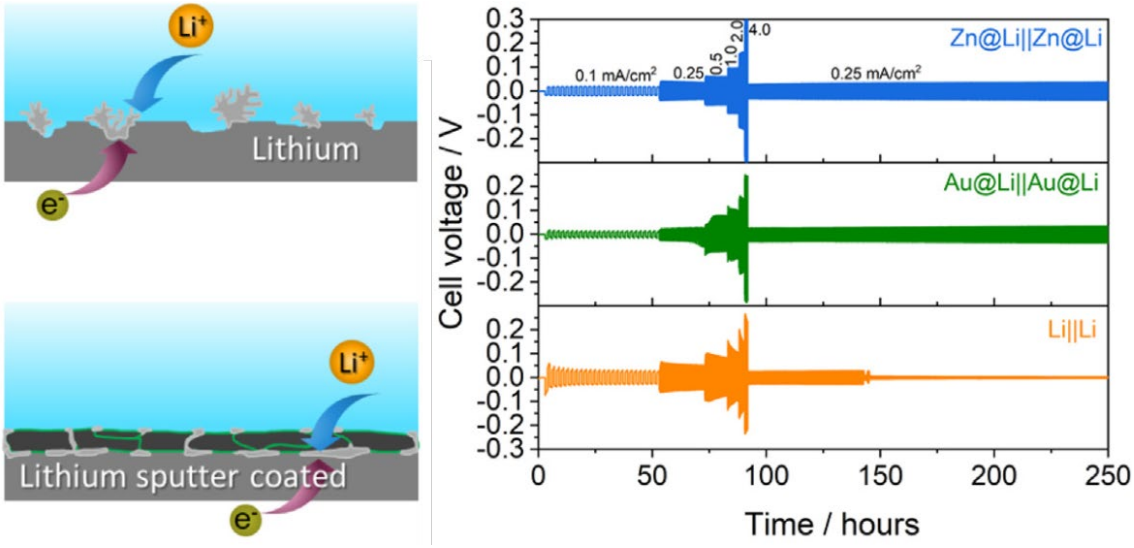


**Figure 1.20** Preparation of lithiophilic modified layer using magnetron sputtering [169].

Due to its high reactivity, metallic lithium can react with a variety of oxides. The spontaneous reaction between metallic lithium and oxides indicates affinity. As a result, many metal oxides or non-metal oxides exhibit affinity with metallic lithium. Utilizing oxides to modify copper current collectors proves effective in enhancing the deposition uniformity of metallic lithium. Oyakhire et al [174]. employed atomic layer deposition technology to deposit an ultra-thin titanium oxide modification layer on the surface of the copper current collector, as depicted in Figure 1.21. The lithiophilic nature of titanium oxide reduces the nucleation energy barrier of metallic lithium on the modified layer, promoting the formation of large and dense nuclei instead of rapidly forming small crystal nuclei. This nucleation behavior achieves uniform deposition of metallic lithium,

significantly improving the cycle life of metallic lithium deposition-extraction on titanium oxide-modified current collectors. Chen et al. [175] utilized laser-assisted technology to modify a silicon oxide layer on the surface of a copper current collector, achieving stable cycling for 250 cycles with a Coulombic efficiency of up to 99.3% at a current density of 2.0 mA $cm^{-2}$. Similar positive outcomes have been reported for lithiophilic oxides such as aluminum oxide and copper oxide [176]. Additionally, graphene oxide, as a versatile two-dimensional material with adjustable conductivity and high surface energy, finds widespread use in the field of energy materials. Wondimkun et al. [177] applied spin coating technology to coat an ultra-thin, binder-free graphene oxide layer on a copper current collector. The presence of graphene oxide induces the nucleation and growth of metallic lithium while inhibiting the growth of lithium dendrites. The use of the modified copper current collector, in combination with lithium nickel cobalt manganese ternary cathode material, in assembling lithium-free anode batteries significantly improves the cycle life of the battery.

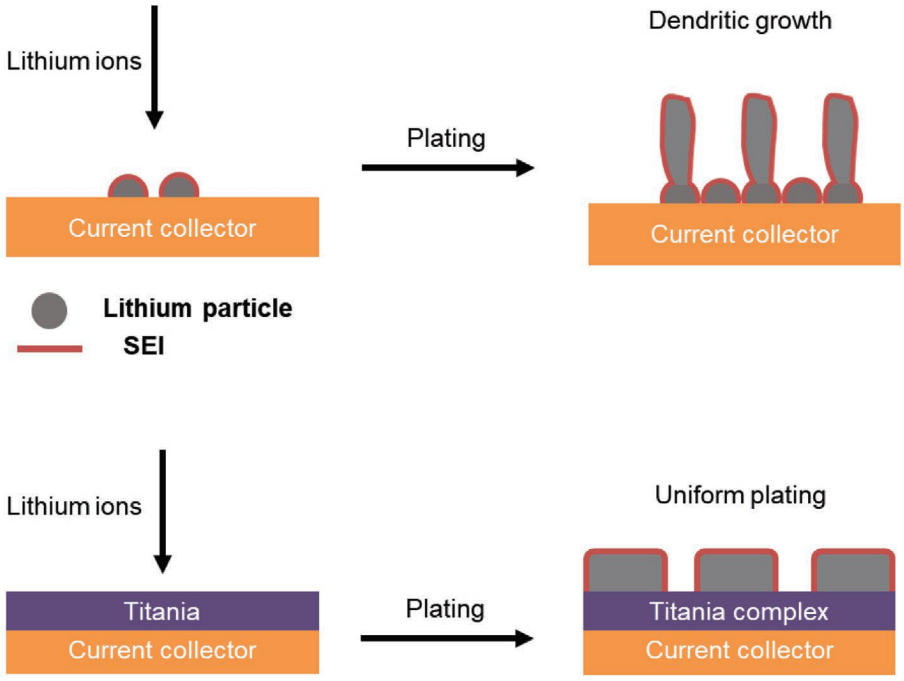


**Figure 1.21** Preparation of titanium oxide modification layer using atomic layer deposition technology for Li deposition [174].

1.5.5.2 Surface conductive layer designed with uniform surface electric field

Liu et al. [178] investigated the impact of different electric field distributions on the current collector surface on metallic lithium deposition using the phase field calculation method. The research revealed that the uneven electric field distribution, caused by the inherent roughness of the current collector surface, exacerbates the non-uniform deposition of metallic lithium. Constructing a uniform electric field on the current collector's surface emerges as an effective strategy to suppress metallic lithium dendrites. Li et al. [179] engineered a copper nitride modification layer on the copper current collector through reactive sputtering. During cycling, the modified layer undergoes reduction by metallic lithium, forming a composite layer consisting of lithium nitride and copper nanoparticles. This composite layer acts as a mixed conductor of ions and

electrons, ensuring a uniform electric field distribution on the current collector's surface. This regulation of lithium ions and electrons induces uniform nucleation and growth of metallic lithium, fundamentally inhibiting metallic lithium dendrites (Figure 1.22). In a similar approach, Lee et al. [180] prepared copper nitride nanowires on the current collector's surface. The copper nitride nanowires, upon lithiation, transformed into lithium nitride-wrapped copper nanowires, facilitating uniform mass transfer of lithium ions in three-dimensional space. This mechanism ensures a stable cycle for the metallic lithium anode. Considering the high lithium ion conductivity of lithium sulfide, He et al. [181] and Lin et al. [182] employed a gas-phase reaction method to form an in-situ copper sulfide modification layer on the copper current collector's surface. After lithiation, a similar mixed conductive network of lithium sulfide and nano-copper was established, achieving the uniform deposition of the metallic lithium anode and extending its cycle life.

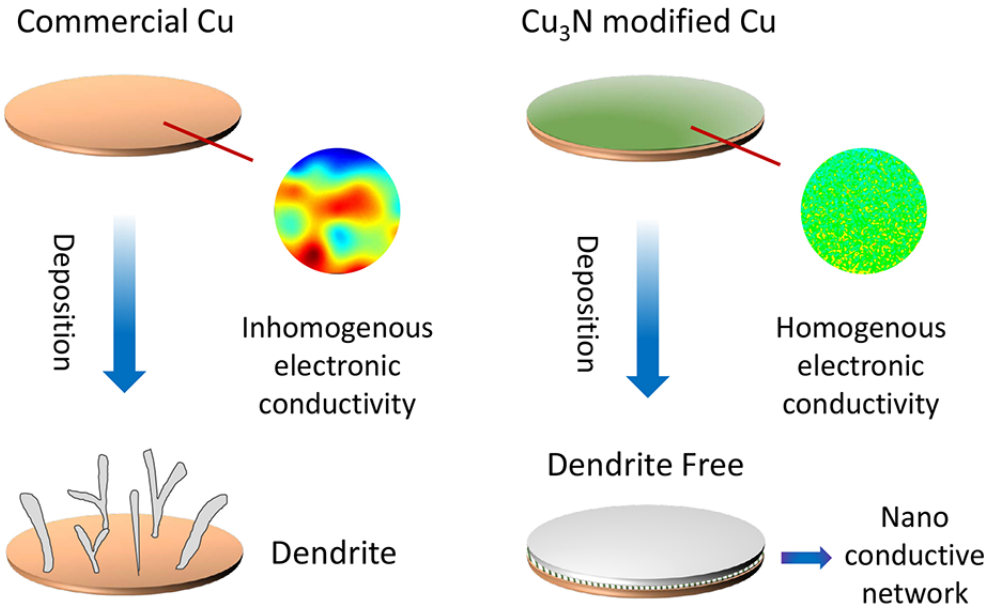


**Figure 1.22** Preparation of copper nitride modification layer using magnetron sputtering for Li deposition [179].

1.5.5.3 Three-dimensional porous structure

The local current density on the electrode surface plays a crucial role in determining the electrodeposition morphology of metallic lithium. To curb the formation of metallic lithium dendrites, researchers have focused on reducing the local current density and optimizing the electric field distribution. Structural modifications to the current collector of the lithium anode have been explored to increase its specific surface area, effectively lowering the local current density on the collector's surface. Essential parameters for the three-dimensional structure design of current collectors include pore volume, pore diameter, and specific surface area, with the latter being a crucial factor influencing the electrodeposition of metallic lithium. In a study by Yang et al., [183] a self-assembly deposition method was employed to immerse commercial copper current collectors in ammonia water, resulting in the creation of a three-dimensional porous copper foil. The percentage of metallic lithium deposited within this three-dimensional structure (η) was found to be typically determined by the ratio of the electrochemically active surface of the current collector to the geometric surface of the electrode, denoted as the electroactive area ratio (r) (Figure 1.23).

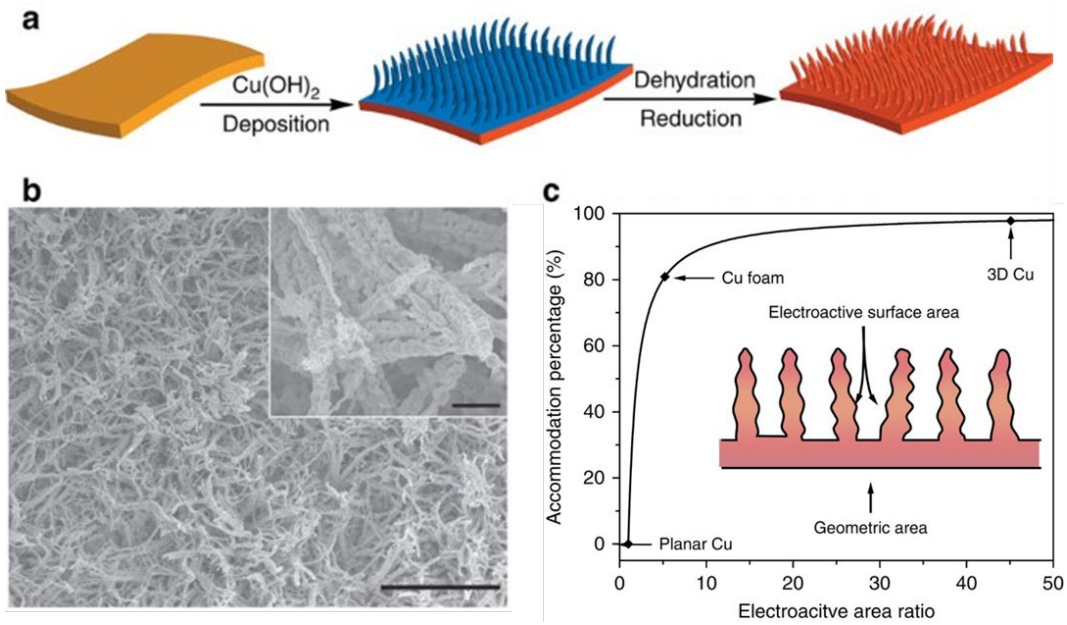


**Figure 1.23** Preparation of three-dimensional porous copper current collector (a); SEM image of three-dimensional porous copper current collector (b); Relationship between the deposition rate of metallic lithium inside the three-dimensional porous structure and its electrochemical active area (c) [183].

A comparison is made between the electrodeposition of metallic lithium on traditional copper current collectors, three-dimensional porous copper current collectors, and foam copper (Figure 1.23 c,). The results highlight the importance of a high electroactive area ratio for three-dimensional current collectors in accommodating lithium metal, which is crucial for achieving high capacity. Through optimized design, the team demonstrated that metallic lithium could be stably cycled for 120 cycles with a Coulombic efficiency of up to 98.5%. To enhance performance further, a lithiophilic aluminum coating was electrochemically modified on the surface of the three-dimensional porous copper current collector. This coating induced uniform nucleation and growth of metallic lithium within the three-dimensional structure [184]. Other researchers, such as Tang et al. [185] and

Umh et al.,[186] utilized electroplating to deposit copper on the surface of an ordered template, producing a three-dimensional porous current collector with controllable pore volume, pore diameter, and surface area. Additionally, numerous studies explored the use of porous structures as current collectors for metallic lithium anodes, developing composite lithium metal with porous current collector materials to create composite lithium anodes. These materials include various metal foams [187], dealloyed porous materials [188, 189], metal mesh [190, 191], carbon cloth [192, 193], and multi-level structured carbon skeletons [194, 195], achieving stable cycling of metallic lithium anodes under high current density and large deposition amounts.

## 1.6 Motivation and objectives

### 1.6.1 Motivation

The current state of lithium metal batteries faces challenges such as uncontrollable dendrite growth and high reactivity with electrolytes, leading to issues like low Coulombic efficiency, short cycle life, and poor safety. These challenges hinder their widespread commercial application. In practical electrochemical systems, the slow diffusion rate of lithium ions on the electrode surface results in inadequate supplementation of lithium-ion consumption, particularly due to fast charge transfer kinetics. This imbalance leads to lithium-ion depletion at the electrode interface, contributing to the growth of metallic lithium dendrites. The current collector plays a pivotal role as the substrate for electrochemical reactions involving metallic lithium. Surface lithophilic modification addresses this by reducing the self-diffusion energy barrier and nucleation energy barrier of metallic lithium through alterations to the current collector's surface state. This modification induces uniform nucleation and growth of

metallic lithium. Additionally, the three-dimensional microstructure design of the interface can regulate the surface area of the current collector, effectively reducing the local current density and promoting uniform electrodeposition of metallic lithium. These strategies aim to overcome the kinetic factors contributing to dendrite growth in metallic lithium.

### 1.6.2 Objectives and outline

This dissertation aims to address the challenges posed by the unstable SEI films and subpar electrochemical performance resulting from lithium dendrite growth through surface engineering of copper foil current collectors. The study involves the preparation and investigation of three distinct modified copper-based current collectors. Utilizing straightforward electrochemical deposition techniques, three-dimensional structured substrates are synthesized. The creation of diverse lithiophilic layers is achieved through chemical reduction methods and high-temperature treatments.

Chapter 2 focuses on the utilization of a facile and scalable electrodeposition method to prepare pyramidal structured copper array (CPA@CF) electrodes designed for lithium metal anodes. The chapter will delve into the morphology, properties, and electrochemical performance of this electrode material.

Chapter 3 investigates the design of three-dimensional current collectors featuring gold-lithiophilic phase modification to enhance the performance of lithium metal anodes. A comparative analysis of the electrochemical performance between planar copper foil and optimized current collectors will highlight the advantages of surface engineering strategies. Ex-situ XRD and SEM characterization will serve to demonstrate the modified current collector's ability to inhibit the growth of lithium dendrites.

Chapter 4 explores the development of a three-dimensional current collector with lithiophilic cuprous oxide phase modification, aimed at stabilizing the SIE film and impeding the growth of lithium dendrites. The enhanced current collector exhibits reduced nucleation overpotential and fosters favorable interfacial reactions. Analytical techniques such as XRD and XPS illustrate the phase transformation undergone by the modified current collector throughout cycling. Ex-situ SEM characterization robustly confirms its effectiveness in curtailing the growth of lithium dendrites.

Chapter 5 provides a comprehensive overview of the research findings and conclusions presented in this dissertation. The innovative aspects of the study are highlighted. The dissertation outlines potential avenues for future research that could propel the project to new heights. Furthermore, this dissertation explores prospects for enhancing strategies related to the lithium metal anode, suggesting pathways for further advancements in the field.

# CHAPTER 2: 3D CU PYRAMID ARRAY GROWN ON PLANAR CU FOIL FOR STABLE AND DENDRITE-FREE LITHIUM DEPOSITION

(Published in MATERIALS SCIENCE, http://doi.org/10.5755/j02.ms.34077)

**ABSTRACT**

Lithium metal is recognized as the anticipated anode for rechargeable batteries because of its inherent physicochemical properties. Unfortunately, the industrialization of Li metal anodes (LMAs) has been entangled in some intractable problems stemming from the uncontrollable growth of Li dendrites, which could result in the issue of short-circuit, thereby leading to cell failure. Here, a three-dimensional structured Cu pyramid array (CPA@CF) is constructed on planar Cu foil (CF) by the simple electrodeposition method. Owing to the features of large surface area and 3D porous structure, the proposed CPA@CF not only can promote Li-ion diffusion and charge transfer, but also effectively slow down the volume change of Li. Consequently, an even and steady Li plating/stripping process up to 360 h is realized using such a CPA@CF current collector. The Li@CPA@CF|$LiFePO_4$ full cell achieves an excellent Coulombic efficiency (CE) of 99.3 % for 160 cycles at 0.3 C with a superior capacity retention of 84.2 %.

**Keywords:** Li metal anode, dendrite-free, current collector, three-dimensional, Cu array.

## 2.1 Introduction

With the expanding demand for electronic products, electric transportation, and the application of clean energy, a cost-effective and performance-enhanced solution is desired [5, 6]. Li metal as an anode has been spotlighted since the 1960s by virtue of its lowest electrode potential of -3.04 V (vs. SHE) associated with the high capacity of 3860 mAh $g^{-1}$, which exceeds is more than ten times that of common graphite anode [18].

However, the implementation of commercial Li metal anode has been impeded by its proneness to the generation of Li dendrite, and severe volume changes during the unceasing cycling process, which generally triggers the SEI (solid electrolyte interphases) film crack and further promotes the side reaction [23, 34]. Meanwhile, the ruptured SEI film causes that the exposed fresh Li metal reacts with the electrolyte, which accelerates the consumption of active materials. These can give rise to low Coulombic efficiency, relatively large interfacial resistance, and even short–circuit issues [29, 36].

Several solutions have been explored to surmount these obstacles. One strategy is to establish a steady electrode/electrolyte interface by tailoring the appropriate electrolytes, such as adding lithium iodide (LiI) [121], nitrofullerene [115] as an electrolyte additive, thus activating a robust SEI film to protect Li metal. Employing artificial SEI film, such as LiF layer [129], and $Li_2S$/$Li_2Se$ protection layer [133], is another strategy. These strategies undoubtedly can form stable interfaces and lessen relentless consumption of active Li. Nevertheless, the optimized SEI layer is not firm enough to stifle the volume expansion of active materials during the Li cycling process. Beyond that, utilizing a 3D conductive host, such as $Ni_3S_2$@3D host [190], Au nanoparticles@3D Ni foam [183], nanoporous $AuLi_3$ nanosheet-modified@Ni foam [192], is a successful approach to postpone the volume change, constrain the growth of Li dendrite. As commercial anode current collectors, a tremendous amount of 3D porous Cu current collectors have been employed to store the active Li and block Li dendrite formation, such as lithiophilic layer modified 3D Cu foam [184], 3D Cu nanowires array [194]. However, the fabrication process of the aforementioned strategies is complicated and expensive, thus restricting

their large-scale commercialization. Consequently, adopting a straightforward, facile, and inexpensive synthesis approach for the construction of current collectors is imperative. Herein, we synthesized a pyramid-structured Cu array (CPA@CF) electrode for Li metal anodes employing the facile electrodeposition method. In comparison with planar Cu foil (CF), nano-pyramids of CPA@CF interleaved stacked to constitute 3D porous structures, which can enlarge the surface area, postpone the disordered expansion of Li and curb Li dendrite growth. Owing to these properties, CPA@CF based electrode exhibits extremely low overpotential, superior Coulombic efficiency (CE) and durable cycling stability up to 360 h. In addition, Li@CPA@CF based full cell also demonstrates outstanding cycling stability and rate properties.

## 2.2 Materials and methods

### 2.2.1 Materials preparation

Synthesis of Cu Pyramid Array/Cu foil: The copper foils were immersed in acetone, ethanol, 0.8 M $H_2SO_4$ and deionized water, sequentially, with ultrasonic treatment for 20 min, and then dried at 60 °C for 30 min. The Cu Pyramid Array (denoted as CPA@CF) was prepared in a three-electrode setup using the Pt-coated Ti mesh as the counter electrode, SCE as the reference electrode and as-pretreated samples (1*2.5 cm) as the working electrode with a 1 $cm^2$ area soaked in the plating solution, which consisting of $CuSO_4 \cdot 5H_2O$ (26 mM), $NiSO_4 \cdot 6H_2O$ (2 mM), $NaH_2PO_2 \cdot H_2O$ (200 mM), $Na_3C_6H_5O_7 \cdot 2H_2O$ (30 mM) and polyethylene glycol (8 mg $L^{-1}$). Potentiostatic electrodeposition was implemented at -1.00 V for 10 min by utilizing the electrochemical instrumentation (CHI760E, CH Instruments, Inc.). The as-prepared samples were washed with deionized water and dried at 60 °C for 30 min.

### 2.2.2 Materials characterization

Material characterization: The scanning electron microscopy (Thermo Scientific™ Helios™ 5 CX Dual Beam field emission system with STEM-in-SEM and a full Oxford AZtec EDS, and FESEM, Hitachi, S-4700) was used to capture SEM, STEM images and EDX elemental mapping results of electrodes and characterize the morphological evolution of lithium deposited on the samples. To facilitate SEM observation, begin by cutting the sample into 1x1 $cm^2$. Next, affix the sample to the holder using conductive tape. Place the holder into the SEM's vacuum chamber and carefully adjust its position and angle to optimize image capture. To characterize the morphology of lithium dendrites, begin by depositing varying amounts of lithium onto current collector within a CR2032-type coin cell. Next, disassemble the coin cell within a glove box filled with argon. Retrieve the lithium-loaded current collector and clean it with DOL (1,3-dioxolane) solvent, followed by drying. Subsequently, cut the sample to the appropriate size and affix it to the holder for imaging. The X-ray Powder diffractometer (Rigaku Ultima-Plus) was used to identify the elements of the samples. Position the 1x1 $cm^2$ sample flat on the glass substrate, and then insert the glass substrate into the X-ray emission chamber. Adjust both the scanning range and scanning speed to the desired parameters for conducting the test.

### 2.2.3 Electrochemical measurements

The CR2032-type coin cells were fabricated in an argon glovebox for the electrochemical properties testing of the samples. Assemble the half-cell in the following sequence: negative electrode case, lithium metal, electrolyte, separator, electrolyte, current collector, electrolyte, and positive electrode case. Coulombic Efficiency measurements and long-

term Li plating/stripping process evaluations under different testing conditions at 25 °C were conducted by employing a NEWARE battery testing system. Coulomb efficiency test procedure: during discharge at a specific current density, the cut-off condition is determined by time; similarly, when charging at the same current density, the cut-off condition is defined by voltage. In the lithium deposition/stripping cycle test, commence by pre-depositing a specified amount of lithium on the current collector to create a lithium-lithium symmetric battery. Subsequently, perform charging and discharging at a specific current density, using time as the cut-off condition. $LiFePO_4$ with an areal mass load of 3 mg $cm^{-2}$ was adopted as the cathode material for the evaluation of the full cells. A certain amount of lithium metal (4 mAh $cm^{-2}$) was predeposited on the samples before assembling the full cell. During EIS (electrochemical impedence spectroscopy) testing, a small-amplitude sinusoidal AC signal is commonly employed as the input signal. The system's impedance is then measured for subsequent equivalent circuit analysis. Both the input and output signals of impedance exhibit three key characteristics: amplitude, frequency, and phase. The EIS analysis with a frequency range of 100 kHz-10 mHz and an amplitude of 5 mV was performed using a model CHI760E instrument.

### 2.3 Material characterization of CPA@CF

A relatively smooth and flat surface of the CF with a small amount of contamination was observed in Figure 2.1 a-c. The CPA@CF possesses a nano–pyramid structure with ridges on the surface contour as exhibited in Figure 2.1 e-f. These Cu pyramid arrays were interleaved stacked to generate a 3D porous structure, which leads to a larger surface area compared to planar CFs. The 3D porous structure owned by CPA@CF could sterically hamper the disordered expansion of Lithium and constrain the growth of Li

dendrites. Also, the construction of the pyramid array amplifies the surface area of the substrates and diminishes the local current density of the electrodes during the Li cycling process. In Figure 2.1 g, the three typical peaks of CPA@CF and CF are consistent and appear at 43.36, 50.32, 74.04°, respectively [196]. These three typical peaks are completely aligned with the (111), (200), and (220) lattice planes of Cu, respectively, according to the standard spectrum of Cu (PDF, No.04-0836), which proves that CPA@CF is perfectly composed of Cu element and has not been oxidized. Meanwhile, EDS elemental mapping of CPA@CF indicates the existence of the element Cu, as exhibited in Figure 2.1 h-j.

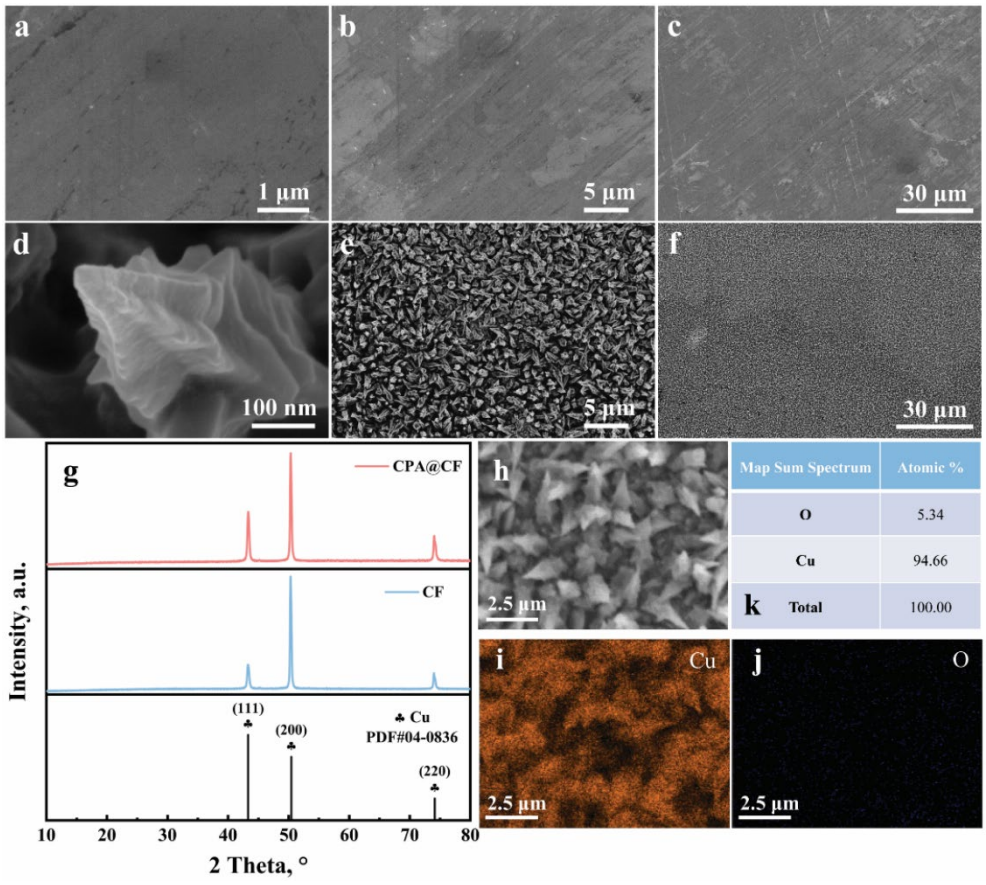


**Figure 2.1** SEM images of the bare CF (a-c); SEM images of CPA@CF (d-f); typical XRD pattern of CF and as prepared CPA@CF (g); SEM image of CPA@CF for EDS

mapping (h); elemental mapping images of Cu (i); elemental mapping images of O (j); the atomic ratio of CPA@CF (k).

### 2.4 Morphological evolution of Li metal

SEM was exploited to observe the morphological evolution of Li metal plated on CF and CPA@CF (Figure 2.2) at 1 mA $cm^{-2}$ with different area capacity densities. At a charge amount stage of 0.4 mAh $cm^{-2}$ (Figure 2.2 a and e), a large number of pebbles-shaped lithium nuclei with erratic-size emerged on the surface of the planar CF. The shape of the Li metal gradually evolves to be more random as the deposition capacity increases (Figure 2.2 b and c). Spaghetti–shaped lithium metal was observed at a charge capacity of 1.6 mAh $cm^{-2}$, as displayed in Figure 2.2 d. The uncontrollable growth of Li dendrite on CFs can be attributable to the planar structure of the substrate and lithophobicity of Cu. In contrast, the morphology of Li metal plated on CPA@CF shows an obviously different evolution trend. The nano-pyramid structure is buried by the spherical lithium nuclei and the arrays structure on the substrate has dissipated at 0.4 mAh $cm^{-2}$ [197]. The size and quantity of spherical lithium nuclei increase as the Li deposition is ongoing (Figure 2.2 j and k). The morphology of lithium metal still maintains a regular ellipse shape, and no dendrites are generated when the charge capacity reaches 1.6 mAh $cm^{-2}$, as displayed in Figure 2.2 l and p. The homogeneous Li distribution on CPA@CF benefits from the 3D porous structure of the Cu array, which is conducive to achieving an even electric field, and uniformly mediating the charge distribution. Figure 2.2 q – r illustrates the behavior of Li plating on planar CF and CPA@CF. Li metal initially grows in an orientation away from the substrate surface and ultimately produces Li dendrites and dead Li after cycling because of the disordered electric field caused by the innate lithiophobicity of copper.

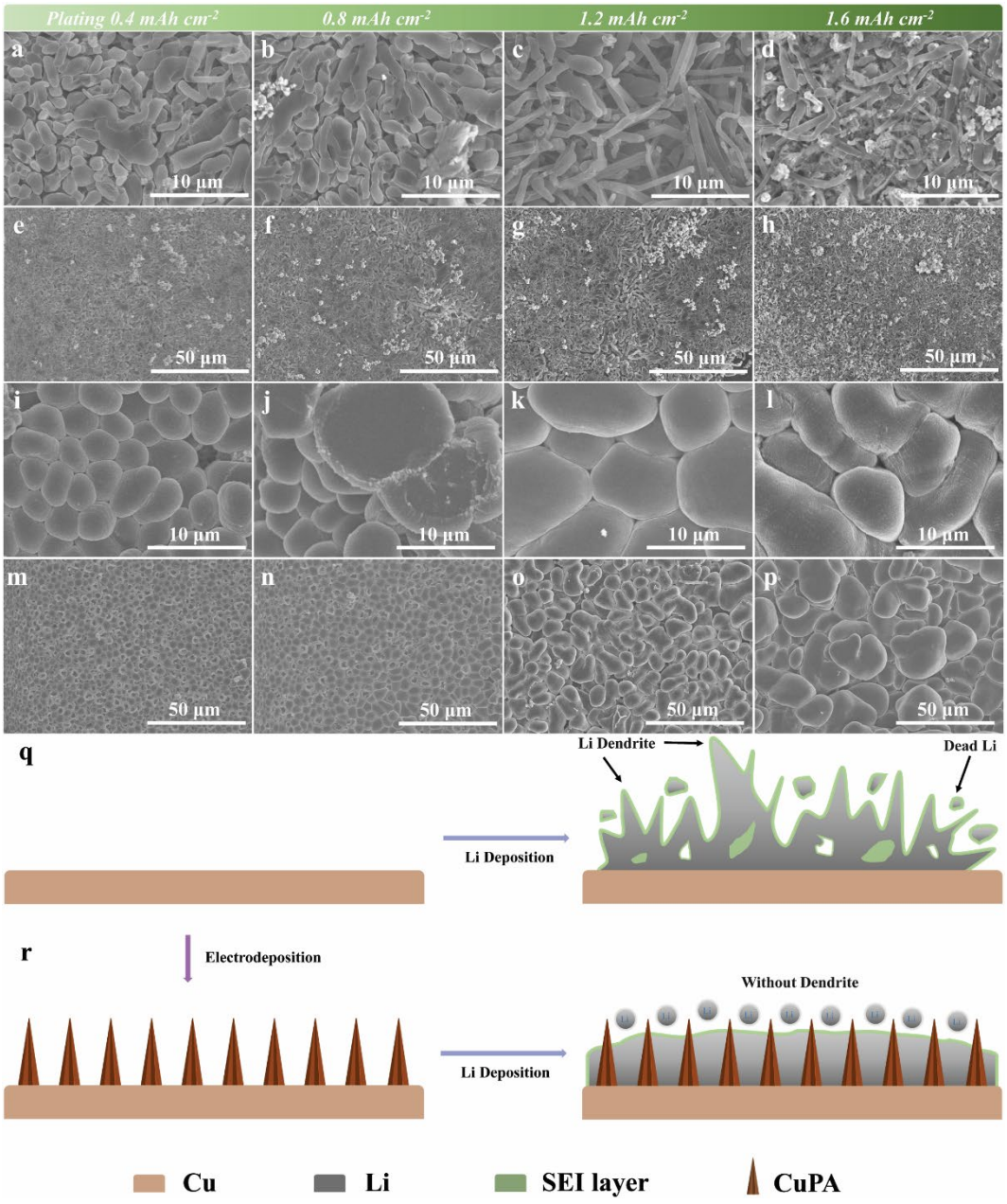


**Figure 2.2** SEM images of Li grown on the CF (a-h); SEM images of Li grown on the CPA@CF (i-p); illustration of Li growth behavior on CF (q); illustration of Li growth behavior on CPA@CF (r).

The enormous Li dendrites generated after long-term cycling can stab the separator and trigger the occurrence of short circuits. By contrast, the CPA@CF current collector

provides a 3D porous structure, which could facilitate the uniform growth of Li and the formation of the steady SEI film. Meanwhile, the infinite volume expansion of Li is significantly mitigated due to the structure of the Cu array, which also can considerably decrease the local current density and achieve Li homogenous deposition.

### 2.5 Electrochemical characterizations of CPA@CF

The nucleation overpotential can be denoted as the gap between the sharp drop of voltage at the initial stage of lithium nucleation and steady voltage plateau at the subsequent stage of further Li plating, which depends on the current density and the degree of lithiophilicity of the substrates [198]. The Li nucleation overpotential on the bare CF is 179.2 mV. In comparison, the Li nucleation overpotential on the CPA@CF is 49 mV, which manifests CPA@CF possesses a prominently low Li nucleation barrier, as shown in Figure 2.3 a and b. To analyze the interfacial performance of two current collectors, EIS measurement was implemented. The diameter of the semicircle ($R_{ct}$) at the high–frequency regions reflects the interfacial resistance and the charge transfer resistance [199]. The planar CF exhibits a high $R_{ct}$ value of 257 Ω before cycling, whereas the CPA@CF current collector displays a low $R_{ct}$ value of 90.58 Ω before cycling (Figure 2.3 c), and then it decreases to 29.53 Ω after 20 cycles, which is less than the $R_{ct}$ value of 42.84 Ω of the CF after 20 cycles (Figure 2.3 d). The lower Rct value of the CPA@CF before cycling and after 20 cycles reveals a superior Li diffusion kinetics and a more stable SEI film during the cycling process.

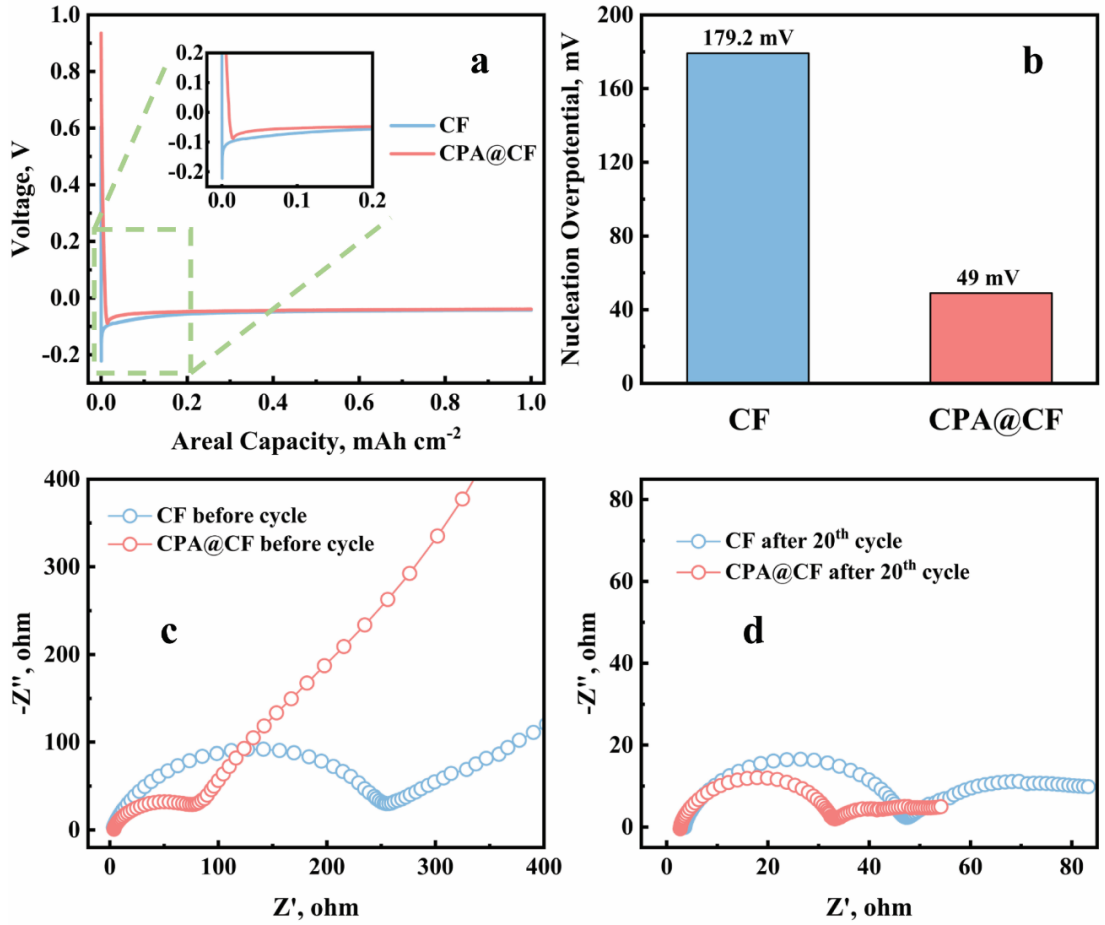


**Figure 2.3** nucleation overpotential of two type electrodes at 1 mA $cm^{-2}$ (a); the corresponding histogram (b); EIS of CF and CPA@CF before cycle (c); EIS of CF and CPA@CF after 20 cycles at 1.5 mA $cm^{-2}$ (d).

The electrochemical properties of the CPA@CF current collector were assessed by Coulombic Efficiency (CE) testing. Figure 2.4 a shows that the capacity of the reversible stripped Li decreases relatively after 10 cycles and reduces significantly after 40 cycles for the CF electrode, while the reversible charge capacity of CPA@CF has remained almost unchanged in subsequent cycling (Figure 2.4 b). The planar CF shows a poor initial CE of 89.1 %, and the CE of the CF after 15 cycles slumps steeply to 68.2 % at 1 mA $cm^{-2}$. In contrast, the CPA@CF maintains an exceptional CE of 96.8 % over 61

cycles, as displayed in Figure 2.4 c. The CE of CPA@CF remains at 94.3 % over 81 cycles, whereas the CE of bare CF displays dramatic degradation after 14 cycles at a different testing condition, as exhibited in Figure 2.4 d. Obviously, the CE of CPA@CF is remarkably enhanced compared to planar CF. The inferior CE performance of the CF can be blamed on the uncontrolled growth of Li dendrites, which gives rise to the rupture of the SEI, whereby the fresh Li metal reacts with the electrolyte, resulting in a large consumption of the active Li.

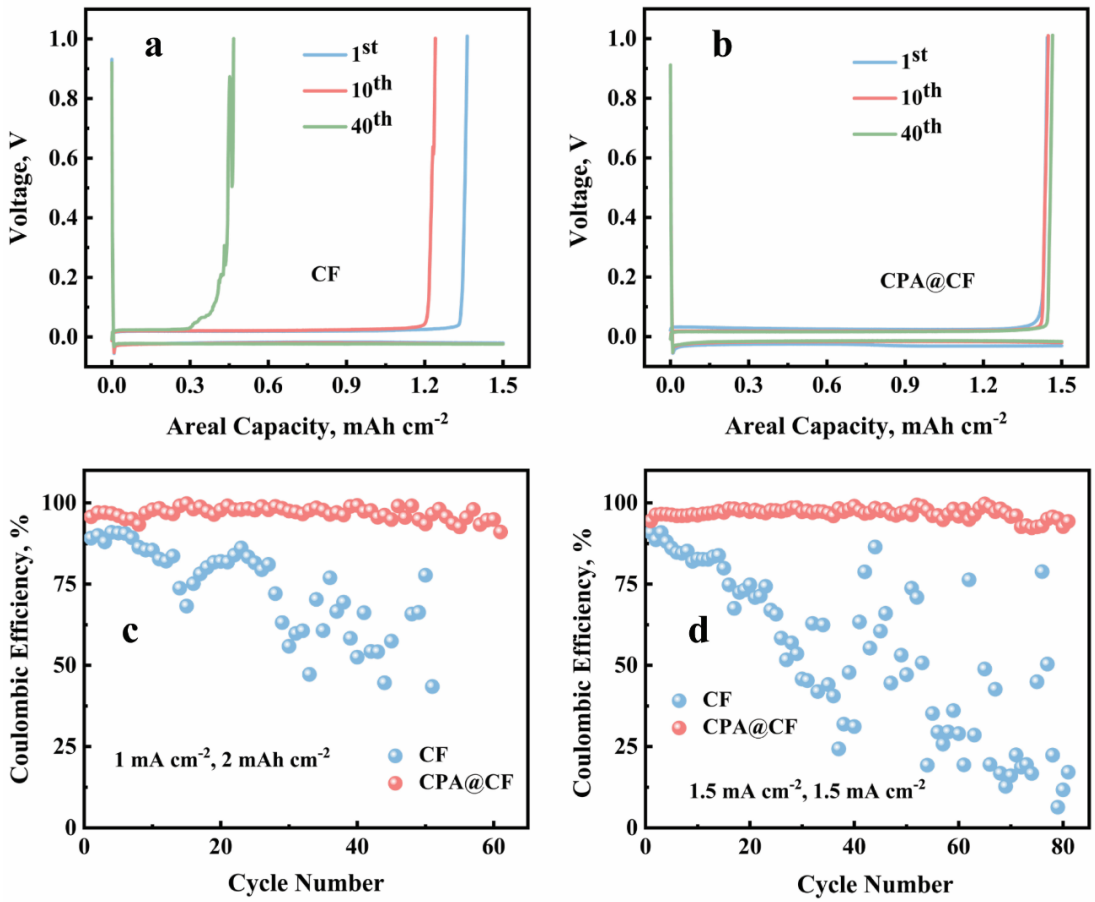


**Figure 2.4** voltage-areal capacity curves of CF (a); voltage-areal capacity curves of CPA@CF at 1.5 mA $cm^{-2}$ (b); CEs of CF and CPA@CF at different testing conditions (c, d).

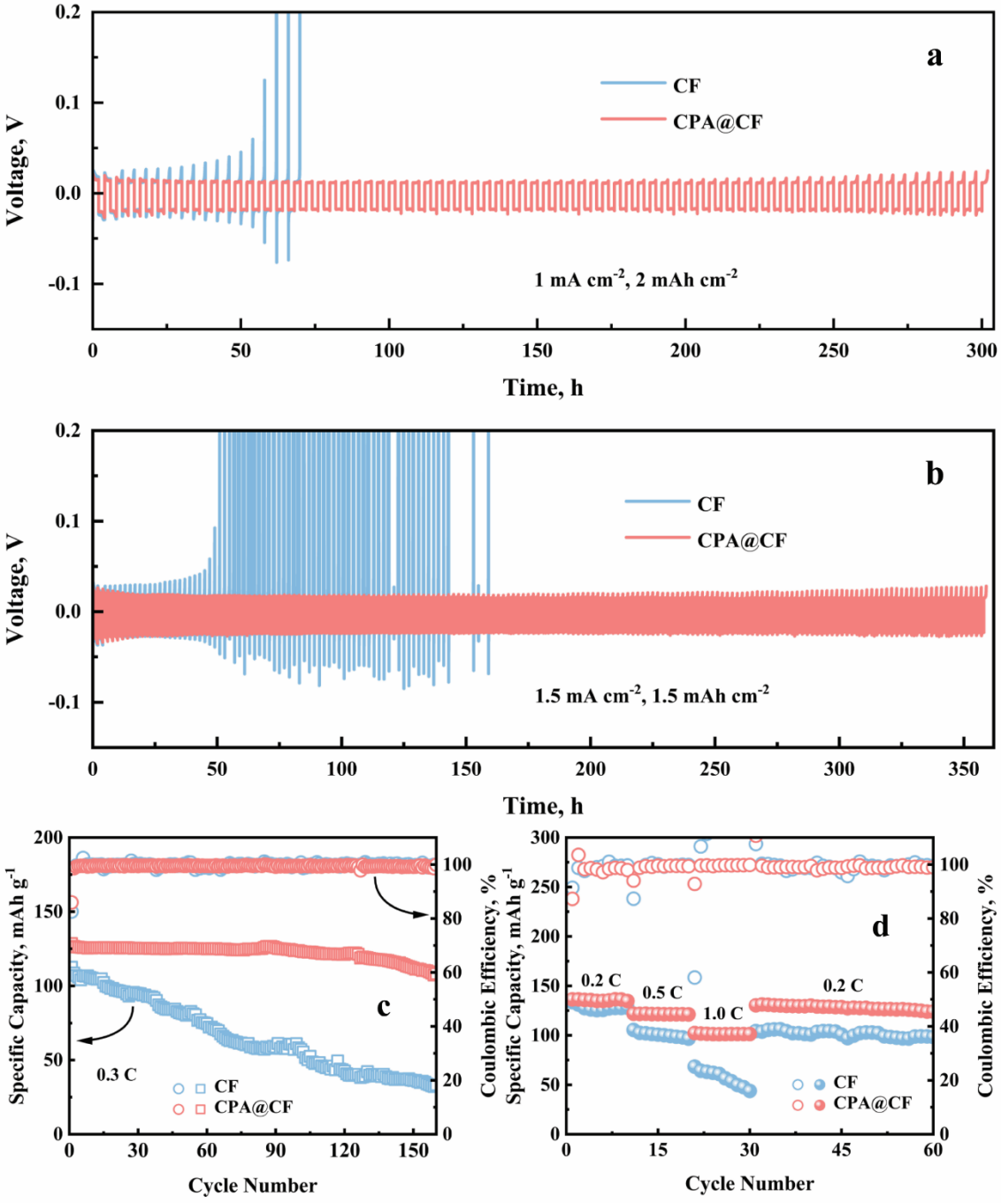


**Figure 2.5** voltage-time curves of CF (a); voltage-time curves of CPA@CF under different testing conditions (b); cycling performance of full cells (c); rate performance of full cells (d).

Moreover, the cycling stability of two current collectors was examined by assembling the CF and CPA@CF based symmetrical coin cells. CPA@CF based electrode exhibits a stable voltage curve without apparent voltage fluctuation at 1 mA $cm^{-2}$, as displayed in Figure 2.5 a. At 1.5 mA $cm^{-2}$, the voltage-curve of the pristine CF shows a sharp ascent after 45 h, indicating an enlarging polarization inside the coin cell, and then an abrupt voltage fall appears after 119 h, resulting from the internal short–circuit and electrode failure, whereas the CPA@CF based electrode can cycle stably for 360 h without the issues of voltage oscillation and short-circuit, as exhibited in Figure 2.5 b. This further proves that the CPA@CF current collector can stably operate at a relatively high current and capacity density and achieve stable charging and discharging cycling.

To evaluate the commercial application of the proposed electrode, full cells were examined by pairing the Li pre-deposited CPA@CF with the $LiFePO_4$ cathode. Figure 2.5 c shows the CE of the Li@CF and Li@CPA@CF based full cells at 0.3 C for 160 cycles. The specific capacity of the Li@CF|$LiFePO_4$ decreases to 33.3 mAh $g^{-1}$ after 160 cycles, while the specific capacity of the full cell with Li@CPA@CF retains at 108.2 mAh $g^{-1}$ after 160 cycles, which is 84.2 % of its initial capacity. The rate performance of full cell with Li@CF or Li@CPA@CF was compared in Figure 2.5 d. The capacity of CPA@CF based full cell is 135.6, 132.4 and 121.4 mAh $g^{-1}$, compared to 127.9, 100.7 and 50.7 of the CF based full cell, at 0.2, 0.5 and 1 C, respectively. Evidently, the CPA@CF based electrode demonstrates the excellent reversible specific capacity and outstanding capacity retention, proving the far–reaching impact of the CPA@CF electrode with the high surface area and porous structure on the electrochemical performance of the full cell.

## 2.6 Conclusions

In summary, we presented a Cu pyramid array/Cu foil (CPA@CF) composite synthesized by facile electrochemical deposition route and as a current collector to channel the Li uniform growth for dendrite-free Li metal battery. The CPA@CF possesses a 3D porous structure, which could greatly augment the surface area of the electrode and effectively lower current density. Meanwhile, the exclusive nano–pyramid structure of the CPA@CF provides an efficient porous path for Li-ion migration and interfacial charge transfer. Due to these positive characteristics, the CPA@CF electrode demonstrates a relatively low nucleation overpotential of Li deposition, superior CE of 94.3 % over 81 cycles and long cycling stability for over 360 h at 1.5 mA $cm^{-2}$. Moreover, the CPA@CF based full cell presents a superior cycling stability at 0.3 C and exceptional rate performance. Our study proffers a promising route to accomplish the practical application of LMAs in prospective energy storage devices.

# CHAPTER 3 MEDIATING LITHIUM PLATING/STRIPPING BY CONSTRUCTING 3D AU@CU PENTAGONAL PYRAMID ARRAY

(Published in Batteries, https://doi.org/10.3390/batteries9050279)

**ABSTRACT**

Lithium (Li) metal is perceived as the "holy grail" of anodes for secondary batteries due to its innate merits. Regrettably, the commercial application of Li metal anodes (LMAs) has been hampered by problems derived from the uncontrollable growth of Li dendrites, which could result in formation of short-circuits, thereby leading to fatal safety accidents. Here, a three-dimensional lithiophilic gold (Au)-coated copper (Cu) pentagonal pyramid array (Au@CuPPA) is constructed on planar Cu foil via electrodeposition followed by a chemical reduction method. Owing to the features of the lithiophilic layer and 3D porous structure, the proposed Au@CuPPA can not only facilitate Li-ion migration and charge transfer, but also effectively diminish the nucleation overpotential. Consequently, an even and steady Li plating/stripping process for up to 460 h and with a charge capacity of 3 mAh $cm^{-2}$ is accomplished by using the Au@CuPPA current collector. The Li@Au@CuPPA|$LiFePO_4$ full cell achieves a high Coulombic efficiency (CE) of 99.4% for 150 cycles at 0.5 C with a capacity retention of 92.4%.

**Keywords:** Li metal anode; dendrite growth; current collector; lithiophilic layer; Cu array; pentagonal pyramid

## 3.1 Introduction

Commercial Li-ion batteries utilizing layered graphite as the anode cannot satisfy increasing energy density requirements for expanding industries focused on energy

storage [13, 15]. Lithium metal is recognized as a highly anticipated anode candidate due to its inherent properties, such as its ultrahigh specific capacity of 3860 mAh $g^{-1}$ and extremely low electrode potential of -3.04 V [11, 14]. These intriguing merits define Li metal as an indispensable component for Li-Sulfur, Li-Air, and Li-Selenium battery systems [2, 7]. However, its persistent impediment to extensive applications is the existence of uncontrollable growth of lithium dendrites during continuous reversible reaction processes, which triggers inhomogeneous Li deposition, decreased stability of solid electrolyte interphase (SEI) film, puncture of the separator, and eventual cell malfunction [4, 20].

To solve these challenges, many approaches, including novel liquid electrolyte additives [118, 124], artificial SEI films [127, 146], and new separators [156, 160], were used to deter the growth of lithium dendrites and stabilize the interfacial reaction of the electrodes. However, these strategies cannot provide the structural host for Li deposition, and the challenge of the lithium metal's boundless volume change is still ubiquitous. Alternatively, employing a porous, structured current collector with a large specific surface area-conductive skeleton has been deemed as an effective and simple method to regulate the volume expansion of Li and confine the dendrite growth [29, 38]. Numerous modified Cu-based current collectors, such as the 3D Cu skeleton with hierarchically structured bi-continuous porosity [189, 192], 3D porous copper [184, 191], or copper mesh [186, 188], were exploited for Li metal anode applications. Unfortunately, Li metal cannot be incorporated into these current collectors due to the weak adhesion of lithium to copper [187]. Particularly, under a high current density, the further Li deposition merely takes place on the upper area of the 3D Cu current collector, causing

underutilization of the porous skeleton [170, 171]. As a result, it is imperative to design a 3D porous Li host with a lithiophilic interface to solve these challenges.

Herein, we synthesized a high surface area copper substrate with a pyramidal architecture which was functionalized by an Au layer (Au@CuPPA) for Li metal anodes by employing the facile electrodeposition and chemical reduction method. In comparison with a planar Cu foil current collector, nano-pyramids of Au@CuPPA are interleaved and stacked to constitute 3D porous structures, which increases the surface area and minimizes lithium dendrite growth. More importantly, the lithiophilic Au layer on the surface of Au@CuPPA can provide diffusion channels for the Li metal that travel to the bottom of the 3D structure, thereby providing an adequate utilization of the nanoporous structure. Owing to these properties, Au@CuPPA-based electrodes exhibit extremely low overpotential, superior Coulombic efficiency (CE), and durable cycling stability for up to 460 h. In addition, the Li@Au@CuPPA-based full cell demonstrates high cycling stability and rate properties.

## 3.2 Materials and Methods

### 3.2.1 Synthesis of Au@Cu Pentagonal Pyramid Array/Cu Foil

The copper foils were sequentially immersed in acetone, ethanol, 0.8 M $H_2SO_4$, and deionized water, with ultrasonic bath treatment for 20 min, and then dried in a vacuum for 30 min at 60 ℃. The Copper Pyramid Array (CuPA) was prepared in a three-electrode setup using the platinum-coated titanium mesh as the counter electrode, saturated calomel electrode as the reference electrode, and the pretreated Cu foil as the working electrode (surface area of 1 $cm^2$) soaked in the electroplating solution consisting of $CuSO_4 \cdot 5H_2O$ (26 mM), $NiSO_4 \cdot 6H_2O$ (2 mM), $NaH_2PO_2 \cdot H_2O$ (200 mM),

$Na_3C_6H_5O_7 \cdot 2H_2O$ (30 mM), and polyethylene glycol (8 mg $L^{-1}$). Potentiostatic electrodeposition was implemented at -1.00 V for 10 min by utilizing the electrochemical instrumentation (CHI760E, CH Instruments, Inc. Austin, TX, USA). Subsequently, 1.5 mg $mL^{-1}$ of $HAuCl_4$ solution and a 200 mM $NaBH_4$ solution were prepared via the magnetic stirring method for 15 min. Then, CuPA was immersed into the $HAuCl_4$ solution with magnetic stirring for 5 min. After that, the $NaBH_4$ solution was added dropwise to the above solution within 1 min after magnetic stirring for 30 min. Lastly, the as-prepared samples denoted as Au@CuPPA were washed with deionized water and dried in a vacuum environment for 30 min at 60 ℃.

### 3.2.2 Material Characterization

The scanning electron microscopy (Thermo Scientific™Helios™5 CX Dual Beam field emission system with STEM-in-SEM and a full Oxford AZtec EDS, Waltham, MA, USA) was used to capture the SEM, STEM images, and EDX elemental mapping results of pristine Cu foil, CuPA, and Au@CuPPA. For STEM observation, the pentagonal pyramid array on the surface of sample is removed using a scraper and transferred to ethanol solvent. Employ an ultrasonic disperser to disperse the array into a suspension suitable for observation. Utilize a dropper to deposit a few drops onto an electron microscope grid covered with a supporting film. Following drying or blotting with filter paper, the resulting specimen is prepared for STEM observation. The X-ray diffractometer (Rigaku Ultima-Plus, Tokyo, Japan) and the X-ray Photoelectron Spectrometer (Thermo Scientific K-alpha$^+$,Waltham, MA, USA) were used to identify the composition information of the samples. XPS technology employs an electron spectrometer to gauge the energy distribution of photoelectrons and Auger electrons

emitted from the sample surface upon X-ray photon irradiation. This method enables qualitative and semi-quantitative analysis. Typically, details such as sample surface element composition, chemical state, and molecular structure can be derived from the XPS spectrum's peak position and shape. Additionally, the sample surface element content or concentration can be determined from the peak intensity. Scanning electron microscopy (FESEM, Hitachi, S-4700, Tokyo, Japan) was utilized to characterize the morphological evolution of lithium metal deposition.

### 3.2.3 Electrochemical Measurements

The CR2032-type coin cells were fabricated in an argon glovebox. Coulombic efficiency measurements and long-term Li plating and stripping evaluation under different current densities and capacity were conducted by employing a NEWARE battery-testing system at 25 °C. Lithium iron phosphate ($LiFePO_4$) with a mass load of 3 mg $cm^{-2}$ was adopted as the cathode material for the evaluation of the full cells. A certain amount of lithium metal (3 mAh $cm^{-2}$) was pre-deposited on the Au@CuPPA substrates before assembling the full cell. The assembly sequence for the full cell is as follows: negative electrode case, current collector with pre-deposited lithium, electrolyte, separator, electrolyte, LFP positive electrode, electrolyte, and positive electrode case. The Electrochemical Impedance Spectroscopy (EIS) measurement with a frequency range of 100 kHz-10 mHz and an amplitude of 5 mV was performed using a CHI760E electrochemical instrument.

### 3.3 Material characterizations of Au@CuPPA

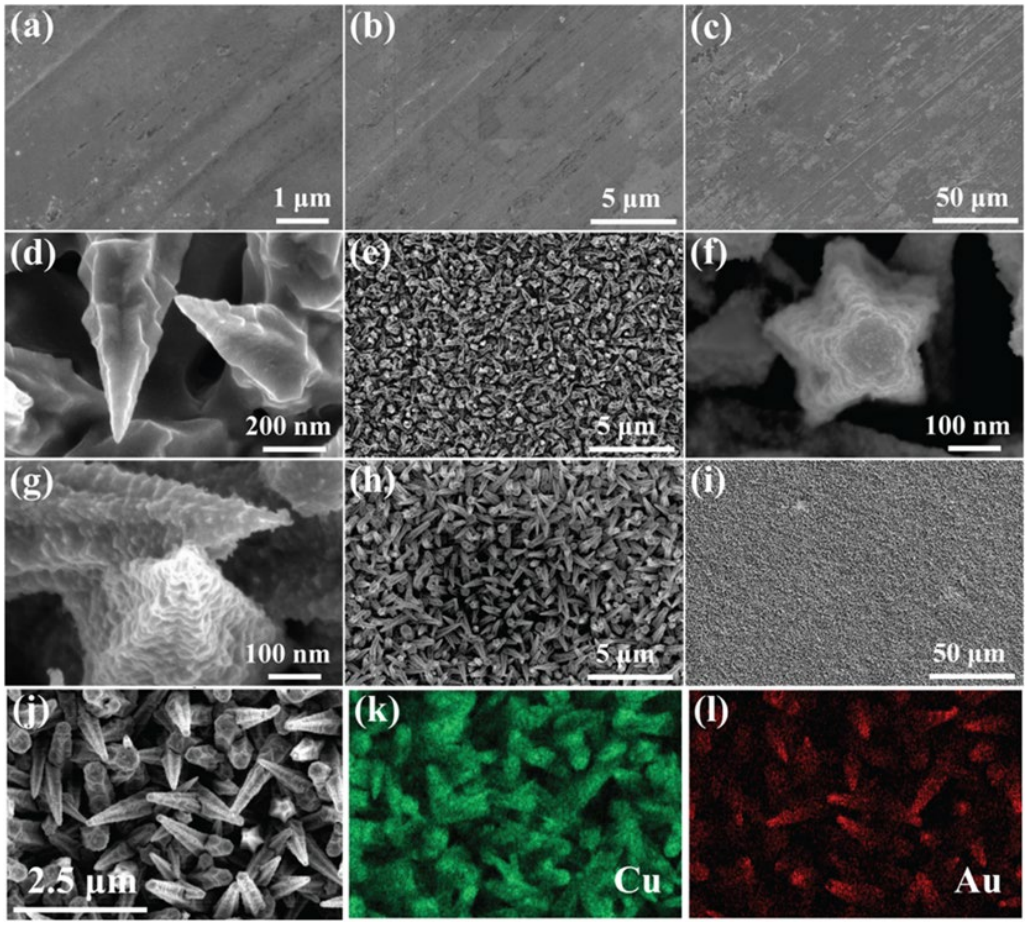


**Figure 3.1** SEM images of (a-c) Cu foil, (d-e) CuPA, and (f-i) Au@CuPPA at different magnifications. Elemental mapping images of (k) Cu and (I) Au for Au@CuPPA in the (j) selected area.

Figure 3.1 a-c displays SEM images of planar Cu foil under different magnifications. A relatively smooth and flat surface of Cu foil was observed. Figure 3.1 d, e shows SEM images of CuPA electrodeposited on pristine Cu foil. The individual CuPA substrate possesses a nano-pyramid structure. These Cu pyramid arrays are stacked to generate a 3D porous structure, which leads to a larger specific surface area compared to planar Cu foil sub-strate. Figure 3.1 f-I demonstrates that Au@CuPPA architecture has a pentagonal

pyramidal shape and surface-modified by gold (Au). Meanwhile, the 3D porous structure owned by Au@CuPPA could sterically retard the growth of Li dendrites. Also, the pentagonal pyra-mid structure expands the specific surface area of the current collector and diminishes the local current density of the electrodes during the Li plating/stripping process. Figure 3.1 j-l illustrates the EDS elemental mapping of Au@CuPPA, indicating the existence and even distribution of the elements Au and Cu.

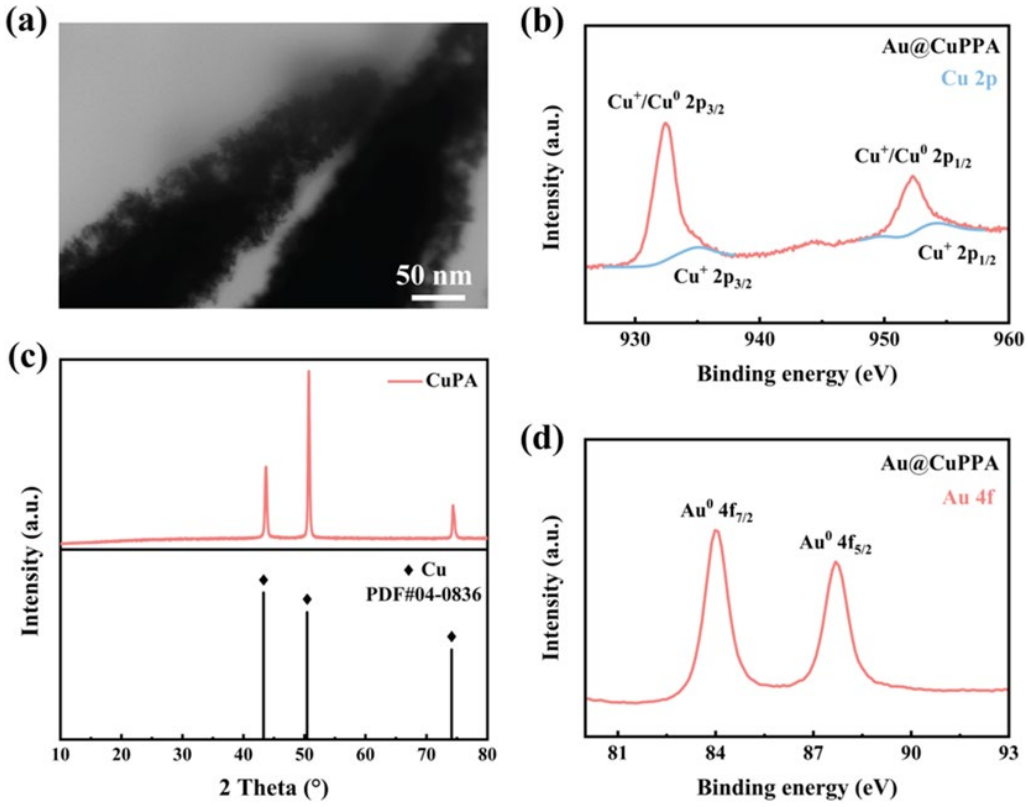


**Figure 3.2** (a) STEM image of Au@CuPPA. (c) XRD pattern of CuPA. XPS spectra of (b) Cu 2p and (d) Au 4f of Au@CuPPA.

The STEM image (Figure 3.2 a) demonstrates a uniform and dense distribution of the Au layer on the surface of the Cu array. Figure 3.2 c displays the XRD profiles of CuPA. The three typical peaks of CuPA at 43.36, 50.32, 74.04°, respectively [200, 201]. These three

typical peaks are completely aligned with the (111), (200), and (220) lattice planes of Cu (PDF, No.04-0836), which proves that CuPA is perfectly composed of Cu element. The Cu 2p XPS spectrum of Au@CuPPA (Figure. 3.2 b) indicates the presence of $Cu^{2+}$ (935.02 and 954.01 eV) and $Cu^{0}/Cu^{+}$ (932.38 and 952.08 eV) [202, 203]. The oxidized Cu is formed during exposure of the sample to the ambient atmosphere. The peaks located at the binding energies of 84.01 and 87.68 eV of Au@CuPPA correspond to $Au^{0}$, as shown in Figure 3.2 d [204].

### 3.4 Morphology of Li metal deposition

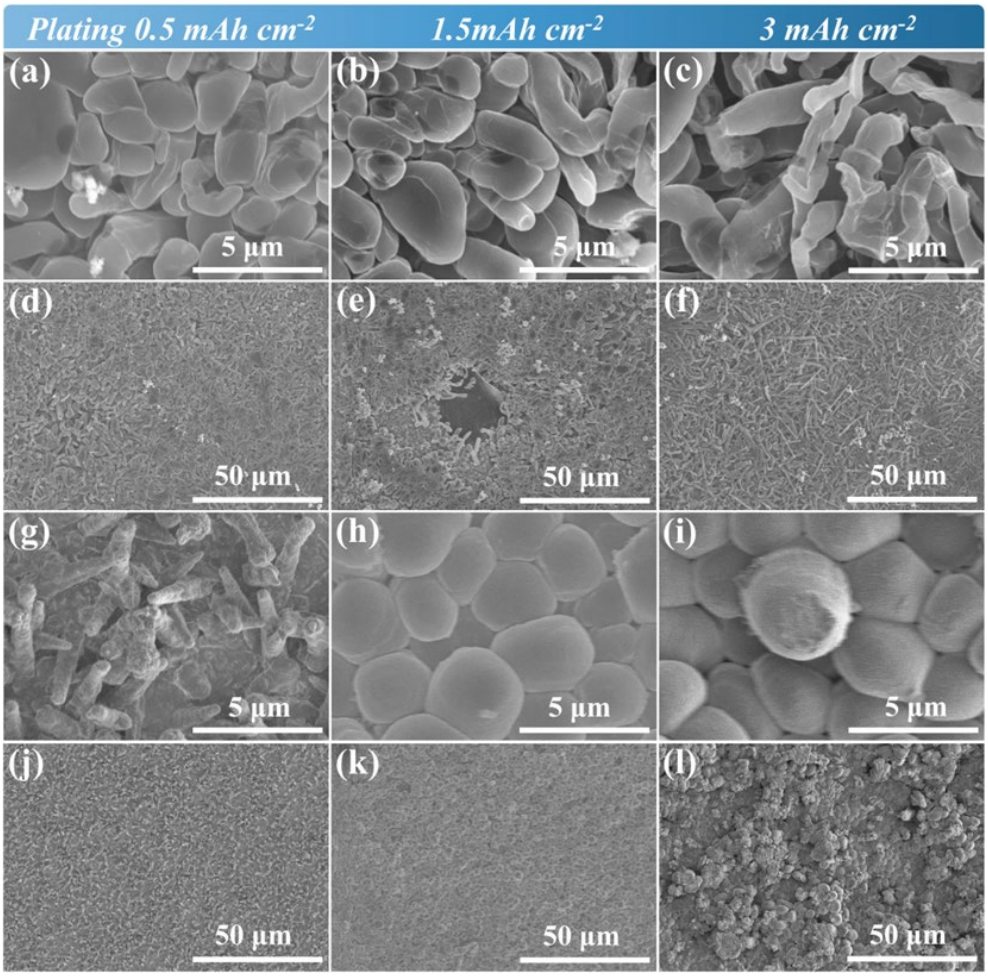

**Figure 3.3** SEM images of Lithium deposited on (a-f) Cu foil and the (g-l) Au@CuPPA with different charge capacities at 3 mA $cm^{-2}$.

The morphological evolution of Li growth on the two type substrates under various charge capacities is displayed in Figure 3.3. At a charge amount stage of 0.5 mAh $cm^{-2}$, numerous pebbles-shaped lithium nuclei with erratic-size emerged on the surface of planar Cu foil, as shown in Figure 3.3 a, d. The shape of the Li metal gradually evolves to be more random as the charge capacity increases (Figure 3.3 b, e). Spaghetti-shaped lithium metal particles are observed at a charge capacity of 3 mAh $cm^{-2}$ (Figure 3.3 c, f). Whereas, the morphology of Li deposition on Au@CuPPA shows a different evolution trend. Li metal will preferentially deposit on the surface of Au@CuPPA along the pentagonal pyramid structures due to the induction effect of gold at a charge capacity of 0.5 mAh $cm^{-2}$, as shown in Figure 3.3 g, h. After 1.5 mAh $cm^{-2}$ of lithium is grown on the electrodes (Figure 3.3 h, k), the nano–pyramidal structure is buried by the spherical Li nuclei [197, 205] and pyramidal arrays on the substrate dissipate completely. The size and quantity of spherical lithium metal particles increase during the ongoing lithium deposition (Figure 3.3 i, l).


**Figure 3.4** The optical images of pristine Cu foil (a), Au@CuPPA (d), and corresponding separators (b, e) and electrodes (c, f) after 30 cycles.

Figure 3.4 a, d is the optical images of bare Cu foil and Au@CuPPA. After the electrochemical deposition and reduction reaction, the surface color of the Cu foil transforms from bright yellow to dark brown, affirming the construction of Au covered Cu pentagonal pyramid array on the Cu foil. After 30 cycles, the surfaces of the separator and electrode corresponding to Au@CuPPA are smooth and contaminant-free, essentially as before use, as shown in Figure 3.4 e, f. By contrast, many black particles emerge on the surface of the separator and electrode corresponding to Cu foil (Figure 3.4 b, c), indicating the generation of abun-dant dead lithium and lithium dendrites, which is attributable to the planar structure and inherent lithiophobicity of Cu foil.

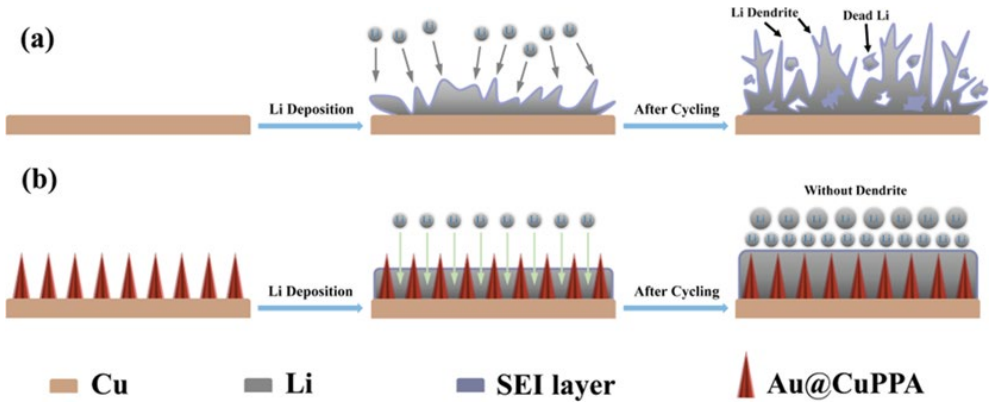


**Figure 3.5** The schematic depiction of Li growth behaviors on (a) Cu foil and (b) Au@CuPPA.

**Figure 3.5** illustrates the deposition behavior of Li metal on the surface of planar Cu foil and Au@CuPPA. Li metal initially grows in an orientation away from the substrate surface and ultimately produces Li dendrites and dead Li after cycling due to the disordered electric field caused by the innate lithiophobicity of copper. The Li dendrites generated after deep cycling can stab the separator and lead to the occurrence of short circuits, as shown in Figure 3.5 a. By contrast, the Au@CuPPA current collector provides substantial lithiophilic Au layer, which facilitates the Li uniform growth on the substrates. In the early Li deposition stage, Li-ion could readily fill up the spaces between nano–pyramids due to the sufficient porosity and high lithiophilicity of the Au@CuPPA surface of. Meanwhile, a steady SEI film is formed on the Li anode surface. In the subsequent cycling, lithium dendrites are absent and spherical lithium metal covers the whole nano-pyramidal arrays, as exhibited in Figure 3.5 b. The volume expansion of Li metal is significantly mitigated due to the large specific surface area of the proposed substrate, which effectively averts unstable electric fields and achieves homogenous deposition of lithium metal.

### 3.5 Electrochemical performance of Au@CuPPA

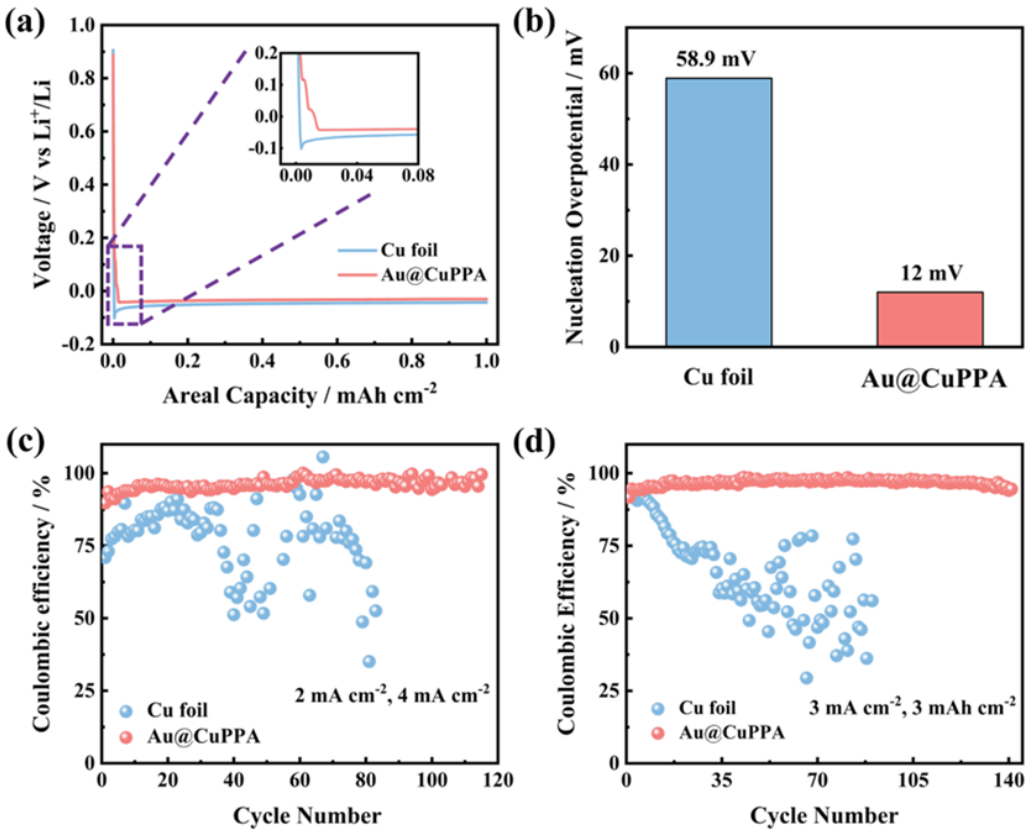


**Figure 3. 6** (a) Voltage profiles of Li nucleation process on two type electrodes at 1 mA $cm^{-2}$, and (b) the corresponding histogram. Coulombic efficiency of coin cells based on two electrodes under different testing conditions (c, d).

The nucleation overpotential of lithium is denoted as the gap between the lowest point of voltage at the initial nucleation stage of lithium and the flat voltage plateau at the subsequent stage of further Li growth, which is affected by the current density and degree of lithiophilicity of the substrates [206, 207]. The Li nucleation overpotential on the bare Cu foil is 58.9 mV, as displayed in Figure 3.6 b. In comparison, the Li nucleation overpotential on Au@CuPPA is approximately 12 mV, which manifests Au@CuPPA possesses an ex-tremely small Li nucleation barrier. Two voltage plateaus can be found in the enlarged view in Figure 3.6 a, indicating two typical lithium-gold conversion

reactions, respectively, which can enhance Li affinity of host, thereby greatly guiding the diffusion channel of Li metal to the bottom of the 3D structure. The phase conversion of Au upon lithiation during the discharging process is given as follows [204]:

$Au \rightarrow Au_3Li \rightarrow AuLi_3$ (1)

Two dealloying reactions occur during the charging process as follows:

$AuLi_3 \rightarrow Au_3Li \rightarrow Au$ (2)

The electrochemical properties of the Au@CuPPA current collector were assessed by Coulombic Efficiency (CE) testing. In Figure 3.6 c, the bare Cu foil displays a poor initial CE of 70.9%, and the CE of Cu foil after 40 cycles slumps steeply to 51.2%. In contrast, the Au@CuPPA maintains an excellent CE of 95.5% over 114 cycles at 2 mA $cm^{-2}$. The first cycle CE of Au@CuPPA is 89%, which is superior to 70.9% of Cu foil, indicating an exceptional plating/stripping process, which is attributable to the stable SEI film and uniform electric field. In Figure 3.6 d, the CE of Au@CuPPA remains at 96.8% over 137 cycles at 3 mA $cm^{-2}$, whereas the CE of planar Cu foil displays dramatic degradation after 8 cycles. Obviously, the CE of Au@CuPPA is remarkably enhanced compared to planar Cu foil. The inferior CE performance of the Cu foil may be attributed to the increased polarization and the uncontrolled growth of Li dendrites, which leads to the rupture of the SEI, exposing fresh lithium metal to the electrolyte, thereby bringing about a heavy consumption of the active Li metal.

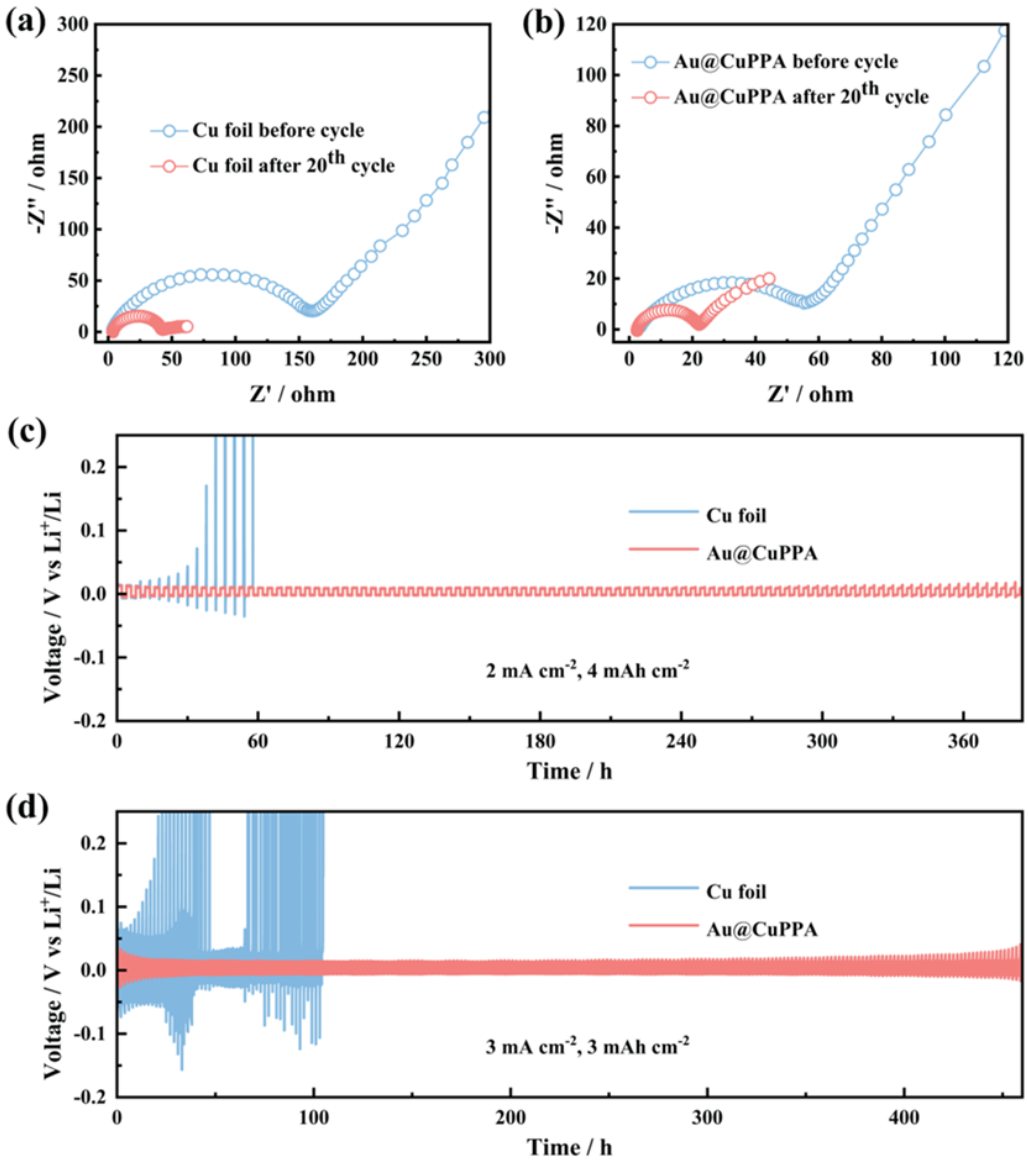


**Figure 3.7** EIS spectrum of (a) Cu foil and (b) Au@CuPPA before cycle and after 20 cycles in symmetric cells. Voltage curves of Cu foil and Au@CuPPA in symmetric cells under different testing conditions (c, d).

To study the interfacial performance of two types of current collectors, EIS measurement was implemented. The diameter of the arc ($R_{ct}$) at the high-frequency regions reflects the solid-liquid interfacial resistance and the charge transfer resistance. The planar Cu foil exhibits a high $R_{ct}$ value of 161.2 Ω before cycling, whereas the Au@CuPPA current

collector displays a low $R_{ct}$ value of 57.26 Ω before cycling, and then it decreases to 18.75 Ω after 20 cycles, which is smaller than the Rct value of 38.42 Ω of Cu foil after 20 cycles, as shown in Figure 3.7 a, b. The lower $R_{ct}$ value of the Au@CuPPA before cycling and after 20 cycles reveals a superior Li diffusion kinetics and a more stable SEI film during Li deposition/stripping process. Meanwhile, the sloping straight line in the low frequency region could be ascribed to the Warburg resistance, which implies the Li-ion diffusion process. From Figure 3.7 a, b, it can be found that the Cu foil exhibits a relatively large slope change before and after cycling, while the slope of the proposed current collector barely alters thus possessing great Li-ion diffusion kinetics, which can be assigned to the larger exposed electrode surface and stable SEI film.

Moreover, the cycling stability of two current collectors was investigated by assembling the symmetrical Li|Li@Cu foil and Li|Li@Au@CuPPA coin cells. The Au@CuPPA based electrode exhibits a stable voltage curve without apparent voltage fluctuation at 2 mA $cm^{-2}$, as exhibited in Figure 3.7 c. At 3 mA $cm^{-2}$, the voltage-time curve of planar Cu foil shows a sharp ascent at the early stage, indicating an enlarging polarization inside the coin cell, and then an abrupt voltage fall appears after 48 h, resulting from the internal short–circuit and electrode failure, whereas the Au@CuPPA based electrode can run stably for 460 h without the issues of voltage oscillation and short–circuit, as shown in Figure 3.7 d. This further proves that the Au@CuPPA current collector can stably operate at a relatively high current density with a large area capacity of Li and achieve stable charging and discharging cycling. Furthermore, Figure 3.8 illustrates the deposition/stripping performance of the CuPA current collector at current densities of 3 and capacity densities of 3. It is evident that the cycle performance of Au@CuPPA under

identical conditions surpasses that of CuPA. This enhancement is attributed to the presence of the surface lithiophilic layer.

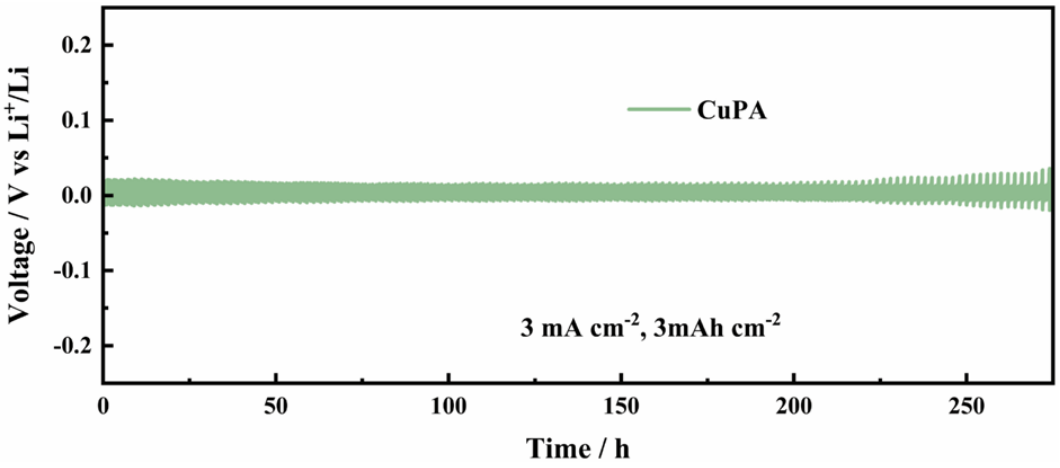


**Figure 3.8** Voltage–time curves of CuPA in symmetric cells under 3 mA $cm^{-2}$, 3 mAh $cm^{-2}$. The CuPA-based electrode exhibits a stable cycle of 275 h at 3 mAh $cm^{-2}$, 3 mA $cm^{-2}$.

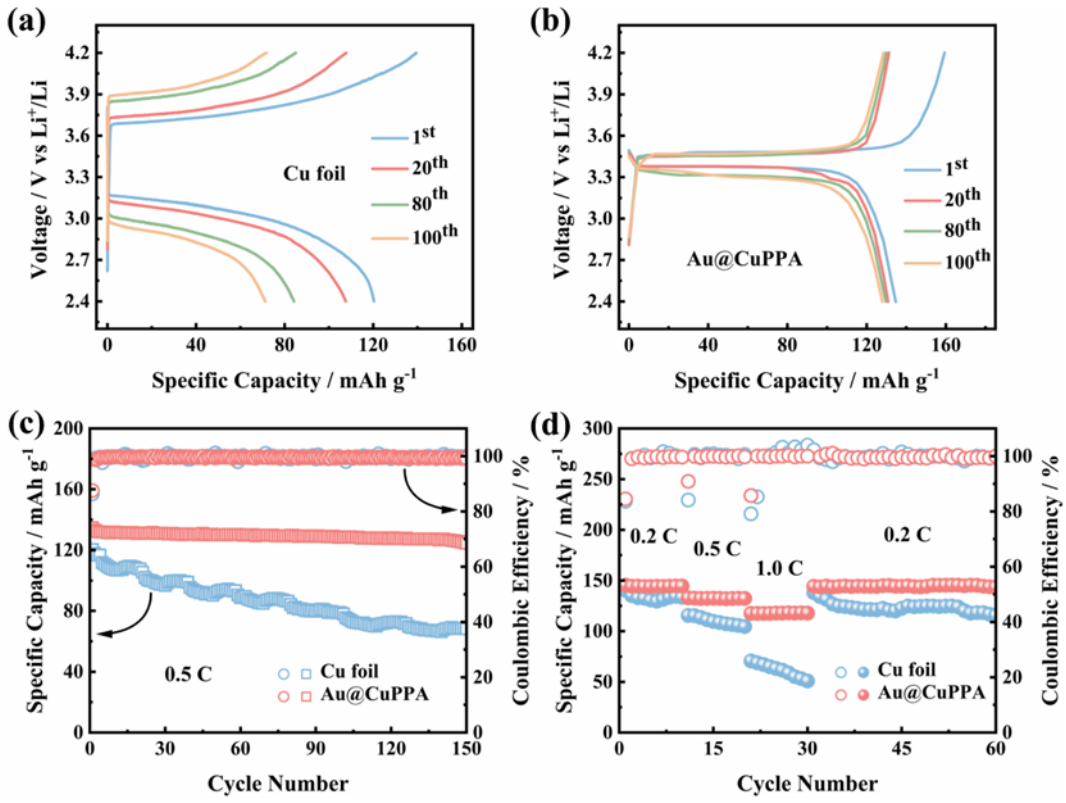

**Figure 3.9** Voltage–specific capacity curves of (a) Li@Cu foil|$LiFePO_4$ and (b) Li@ Au@CuPPA|$LiFePO_4$ cells at 0.5 C with various cycles. (c) Cycling performance of two type electrodes based full cells at 0.5 C. (d) Rate performance under various current rate for Li@Cu foil|$LiFePO_4$ and Li@ Au@CuPPA|$LiFePO_4$ full cells.

To evaluate the commercial application of the proposed electrode, the full cell was examined by pairing the Li-predeposited Au@CuPPA composite with $LiFePO_4$ cathode. $LiFePO_4$ electrode was provided by Guangdong Canrd Technology Co.,Ltd. From Figure 3.10 a-d, it can be seen that the Lithium Iron phosphate electrode has uniformly dispersed particles, and the particle size distribution is approximately between 300 nm and 1 μm. Figure 3.10 e is the EDX spectrum of the LFP electrode, indicating its phase composition. Figure 3.9 a displays the charging-discharging curves of Li@Cu foil|$LiFePO_4$ at 1st, 20th, 80th, 110th at 0.5 C, respectively, from which a large and volatile voltage polarization can be found with a capacity of 139.5 mAh $g^{-1}$ in 1st charging. By contrast, the Li@ Au@CuPPA|$LiFePO_4$ presents a capacity of 159.4 mAh $g^{-1}$ in 1st charging process and a visible voltage plateau with a small and stable voltage polarization, as displayed in Figure 3.9 b. Moreover, the cycling performance of the Au@CuPPA and Cu foil based full cell at 0.5 C for 150 cycles is exhibited in Figure 3.9 c. The capacity of the Li@Cu foil|$LiFePO_4$ decreases to 68.2 mAh $g^{-1}$ after 150 cycles, whereas the capacity of the Li@Au@CuPPA electrode maintains at 124.5 mAh $g^{-1}$ after 150 cycles, which is 92.4% of its initial capacity. Beyond that, the rate performance of the Li@Cu foil or Li@Au@CuPPA was compared in Figure 3.9 d. The specific capacity of Au@CuPPA based full cell is 144.5, 132.4 and 117.5 mAh $g^{-1}$, compared to 134.4, 109.7 and 63.1 of the full cells with Cu foil, at 0.2, 0.5 and 1 C, respectively. Evidently, the Au@CuPPA

based electrode demonstrates excellent reversible specific capacity and outstanding capacity retention, proving the far-reaching impact of the Au@CuPPA electrode with the lithiophilic layer and 3D porous structure on the electrochemical performance of the full cell.

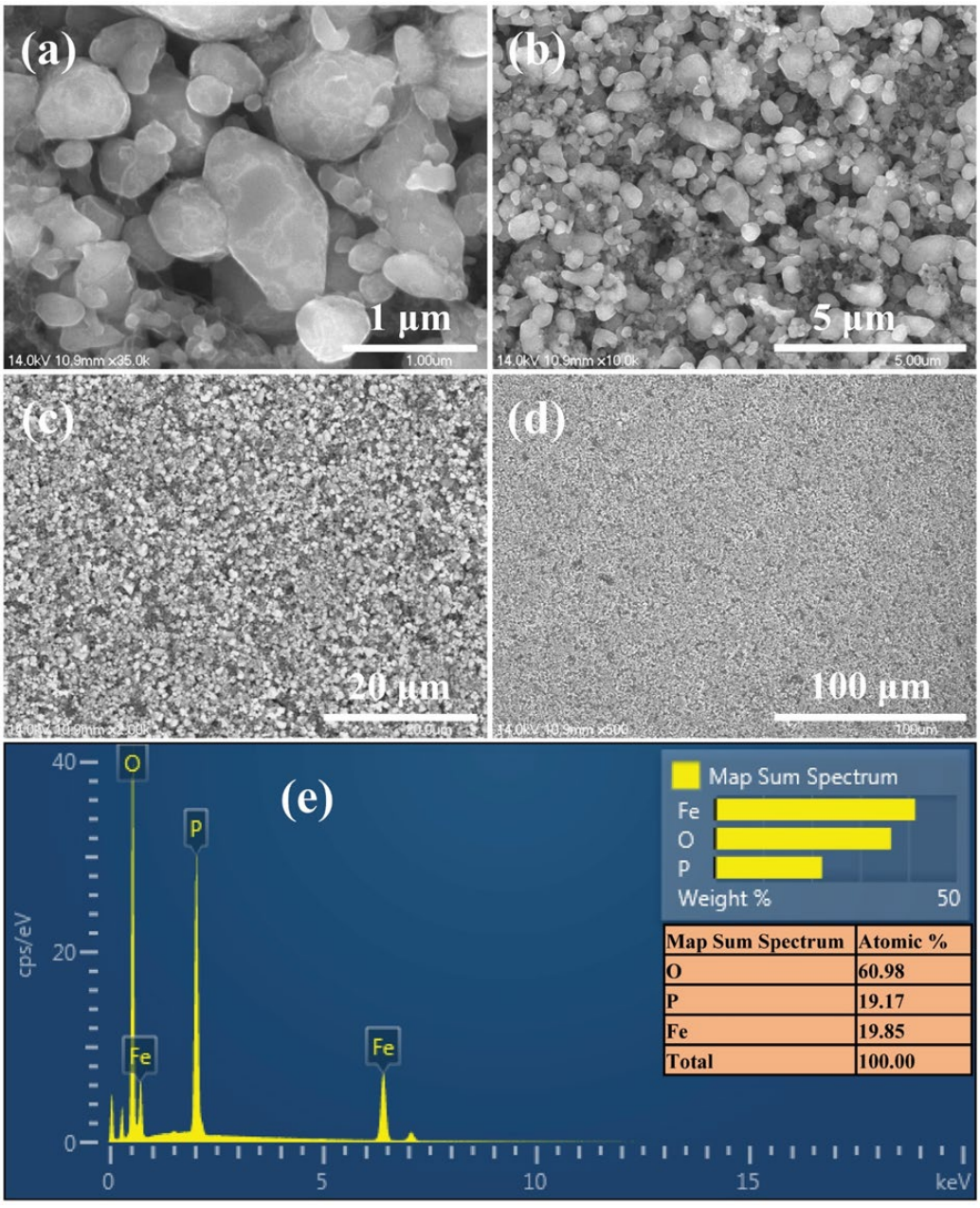


**Figure 3.10** The SEM images (a-d) and EDX spectrum (e) of the $LiFePO_4$ electrode under different magnifications.

**Table 3.1** Comparison of electrochemical performances of different LMAs in full cells with LFP

| **Anodes** | **Mass load (mg cm$^{-2}$)** | **N/P ratio (anode : cathode)** | **Cycle number (n)** | **Ref.** |
|---|---|---|---|---|
| Ni nano-cone @ Al | 1.4 | 8.4 | 110 | [198] |
| MXene @ Au host | 1 | 29 | 200 | [202] |
| CuO nanowire arrays/Cu | 2 | 5.8 | 150 | [208] |
| Cu(f) @ Sb | 3 | 7.85 | 160 | [201] |
| Cu nanowire @ poly (1,3,5-triethynylbenzene) (PTEB) nanofiber | 2 | 14.7 | 100 | [200] |
| CuO nanofilm-covered Cu microcones @ Cu foil | 1.3 | 9 | 100 | [198] |
| Au@CuPPA (This work) | 3 | 5.8 | 150 | Our work |

The mass loading of the LPF cathode and the N:P ratio affect the electrochemical performance of the full cells. Generally speaking, an excessively large N:P ratio means

that the capacity of the anode is too large, which may lead to good electrochemical performance but is contrary to industry standards (the N:P ratio of commercial batteries is generally about 1.06-1.10). In this manuscript, we used LPF with a mass loading of 3 mg $cm^{-2}$ (capacity density of 0.51 mAh $g^{-1}$) as a cathode. The N:P ratio is 5:8 in this work, which is very relatively close to the industry standard compared to previous publications, as shown in Table 3.1. Meanwhile, the proposed anode exhibits relatively good cycling performance at the lowest N:P ratio.

### 3.6 Conclusions

In summary, we present an Au-modified Cu pentagonal pyramid array synthesized by a facile electrochemical deposition and chemical reduction route. The synthesized array was used as a current collector to provide the homogeneous deposition of lithium for dendrite-free Li metal batteries. Au@CuPPA structure possesses a lithiophilic Au-functionalized surface, which lowers Li metal nucleation barriers. Meanwhile, the Au@CuPPA pentagonal nano-pyramid structures provide an efficient porous path for Li-ion transport and interfacial charge transfer. Due to these characteristics, the Au@CuPPA substrates demonstrate an extremely low nucleation overpotential during Li deposition, superior coulombic efficiency of 96.8% over 137 cycles, and long-term cycling stability for over 460 h at 3 mA $cm^{-2}$. Moreover, the Au@CuPPA based full cell presents superior cycling stability at 0.5 C and extraordinary rate performance. This study offers an avenue to realize the potential application of LMAs in prospective high-energy batteries.

# CHAPTER 4 INTERLACED STACKED HOLLOW CU2O DENDRITE FOR STABLE LITHIUM METAL ANODE

**ABSTRAT**

The stable operation of lithium metal batteries faces hindrances due to the persistent issue of uncontrolled lithium dendrite growth. In this study, we present a facile approach wherein 3D structured cuprous oxide ($Cu_2O$) dendrites are constructed on flat copper foil through a straightforward process involving electrodeposition and subsequent high-temperature treatment. The thin lithium oxide ($Li_2O$) layer stemming from lithiophilic $Cu_2O$ further establishes a conducive channel for the swift diffusion of lithium ions ($Li^+$) at the solid-liquid interface. Notably, the staggered stacking of $Cu_2O$ dendrite results in a 3D structure with a significantly enlarged specific surface area, which not only mitigates current density but also promotes a uniform distribution of Li flow. The proposed $Cu_2O$ electrode yields superior performance, achieving a Coulombic efficiency of up to 98.2% and a sustained lithium deposition/stripping process lasting an impressive 880 h. In the full cells, employing Li/$Cu_2O$ dendrite electrode, an exceptional Coulombic efficiency (CE) of 99.9% is attained after 160 cycles at 1 C, coupled with an admirable capacity retention rate of 84%. These findings underscore the promising potential of the $Cu_2O$ dendrite electrode for advancing the practical applications of lithium metal batteries.

**Keywords:** Lithium metal anode, 3D current collector, Lithiophilic $Cu_2O$, Li plating/stripping

## 4.1 Introduction

In the face of rapid advancements in consumer electronics and electric vehicles, traditional lithium-ion batteries, which rely on layered graphite as anodes, encounter the formidable challenge of the ever-growing energy density requirements [8, 9]. Among the array of available anodes, lithium metal stands out as a highly anticipated next-generation anode candidate according to both academia and industry, owing to its intrinsic properties, including an ultra-high specific capacity of 3860 mAh $g^{-1}$ and an extraordinarily low electrode potential of -3.04 V [27, 65]. These compelling advantages underscore the crucial role of lithium metal as an essential component in lithium-sulfur [26], lithium-air [49], and lithium-selenium [49] battery systems.

Despite the early deployment of lithium metal as an anode material in the 1970s, particularly in Prof. Whittingham's pioneering lithium battery [209], its widespread utilization has been hindered by the persistent challenge of uncontrolled lithium dendrite growth during continuous reversible reaction, which leads to uneven lithium deposition, compromised solid electrolyte interphase (SEI) film, separator puncture, and eventual battery failure [47, 58].

To surmount these challenges, various strategies have been employed to impede lithium dendrite growth and stabilize the interface which include innovative liquid electrolyte additives [99, 107], artificial SEI membranes [142, 151], and novel separators [159]. However, these approaches often fall short in providing suitable structural hosts for lithium deposition, leaving the issue of the infinite volume changes of lithium metal unresolved [178, 179]. Additionally, the adoption of 3D porous current collectors with conductive skeletons has emerged as a predominant and straightforward method to

regulate lithium volume expansion and curtail dendrite growth [186]. Numerous Cu-based current collectors with three-dimensional porous structures, such as 3D copper skeletons with bicontinuous pores in a hierarchical structure [191], and 3D porous copper [169] or copper meshes [150, 170], have been utilized in Li metal anodes due to their commendable electrical conductivity and chemical inertness. Nevertheless, the weak adsorption of lithium to copper, stemming from their disparate lattice structures, impedes the incorporation of lithium metal into these current collectors [179]. Consequently, several lithiophilic phases are developed via surface engineering on the 3D Cu current collector to address the lithiophobic interface issue [172, 177].

Despite these modifications, at elevated current densities, further lithium deposition predominantly occurs in the upper region of the 3D Cu current collector, resulting in underutilization issue of the porous framework [190]. Moreover, the use of expensive materials such as Au [203] and Ag [172] for lithiophilic phases is impractical for commercialization. Transition metal oxides such as copper oxide (CuO) [210], tin oxide ($SnO_2$) [175], and zinc oxide (ZnO) [174] have been considered as more practical lithiophilic phases. However, the oxygen content in these TMOs plays a critical role in determining the thickness of the lithium oxide layer in the derived SEI film [127, 153]. While the lithium oxide layer, as a vital component of the SEI film, possesses properties such as ionic conductivity and electronic insulation, an excessively thick lithium oxide layer due to an abundance of oxygen content can impede ion diffusion, leading to severe interface problems [210-212].

In this work, we employ a straightforward two-step methodology involving electrodeposition and subsequent high-temperature treatment to fabricate copper

substrates covered with $Cu_2O$ dendrites, offering a promising solution for achieving stable lithium metal anodes. In contrast to flat copper foil current collectors, the distinctive feature of $Cu_2O$ dendrites, arranged in a staggered stacked fashion on the copper substrate, results in the formation of a 3D structure, which significantly enhances the surface area and effectively mitigates the challenges associated with the infinite volume expansion of lithium metal. The special arrangement of $Cu_2O$ dendrites provides a favorable habitat for Li metal, ensuring optimal utilization of the 3D structures and hampering uncontrolled lithium metal expansion. Furthermore, the $Cu_2O$ layer on the surface serves as a diffusion channel, facilitating the penetration of Li metal to the base of the 3D structure, which is instrumental in fully exploiting the advantages of the nanoporous architecture. Notably, the thin lithium oxide layer, attributed to the lower oxygen content of $Cu_2O$, promotes rapid lithium ions diffusion at the interface, contributing to the superior performance of the $Cu_2O$ dendrite electrode. As a result of these advantageous properties, the $Cu_2O$ dendrite-based electrode demonstrates a remarkable reduction in interfacial resistance, coupled with an impressive Coulombic efficiency (CE) of 98.2% and exceptional cycling stability up to 880 h. Additionally, the full cell employing Li/$Cu_2O$ dendrite exhibits a commendable capacity retention of 84% and outstanding rate performance, attesting to the potential application of the $Cu_2O$ dendrite electrode as a promising candidate for advanced lithium metal batteries.

## 4.2 Experimental method

### 4.2.1 Synthesis of $Cu_2O$ Dendrite Current Collector

The fabrication of the $Cu_2O$ dendrite current collector involved a strict procedure to ensure optimal electrode performance. The commercial copper foil undergoes a rigorous

cleaning process by sequential immersion in acetone, ethanol, 0.8 M $H_2SO_4$, and deionized water. Subsequently, the cleaned copper foil is subjected to a 20-minute ultrasonic bath treatment, followed by vacuum drying at 60 °C for 30 minutes, resulting in a thoroughly dried and pristine copper foil. The preparation of copper dendrites is carried out in a three-electrode system, utilizing a platinum-covered titanium mesh as the counter electrode, a saturated calomel electrode as the reference electrode, and the as-treated copper foil (with a surface area of 1 $cm^2$) as the working electrode. The clean Cu foil is immersed in a plating solution comprising $CuSO_4 \cdot 5H_2O$, $NiSO_4 \cdot 6H_2O$, $NaH_2PO_2 \cdot H_2O$, $Na_3C_6H_5O_7 \cdot 2H_2O$, and polyethylene glycol. The electroplating process is carried out under potentiostatic conditions at -1.00 V for 10 minutes using a sophisticated electrochemical instrument (CHI760E, CH Instruments, Inc. Austin, TX, USA). Notably, bubbles continuously emerge on the surface of the working electrode during the deposition process. Following the electroplating step, the dried copper dendrite electrode undergoes a critical transformation through exposure to an air atmosphere at 250°C for 2 h. This necessary heat treatment results in the desired cuprous oxide ($Cu_2O$) dendrite current collector.

### 4.2.2 Material Characterization

The $Cu_2O$ dendrite electrode undergoes comprehensive material characterization to elucidate their structural and compositional attributes, employing state-of-the-art analytical techniques. STEM images of the $Cu_2O$ dendrites are acquired utilizing a cutting-edge scanning electron microscope, the Thermo Scientific™ Helios™ 5 CX dual-beam field emission system, Waltham, MA, USA. The phase composition of the samples is identified using a Rigaku Ultima-Plus X-ray diffractometer, Tokyo, Japan. The Thermo

Scientific K-alpha$^{+}$, a cutting-edge X-ray photoelectron spectrometer produced in Waltham, MA, USA, is employed to investigate the valence states of elements present in the $Cu_2O$ dendrites. Microstructural observations of the copper foil, copper dendrites, and cuprous oxide dendrites are conducted using a Hitachi S-4700 field-emission scanning electron microscope, fabricated in Tokyo, Japan. In addition, energy-dispersive X-ray (EDX) elements mapping of electrodes and characterization of the morphology of Li metal deposition are conducted by employing this instrument.

### 4.2.3 Electrochemical Measurements

To assess the electrochemical performance of the electrodes, a series of precise measurements and evaluations are conducted using standard electrochemical testing procedures. CR2032 coin cells are assembled within an argon-filled glove box to maintain an oxygen and moisture-free environment, for accurate electrochemical measurements. Coulombic efficiency (CE) measurements and evaluations of long-term lithium deposition/stripping are performed on a half-cell configuration at room temperature, executing at varying current densities and durations using a LANDT battery test system. Lithium iron phosphate ($LiFePO_4$) with a mass loading of 2.5 mg cm$^{-2}$ serves as the cathode for the performance evaluation of the full cell. Prior to assembling the full cell, a fixed amount of Li (3 mAh cm$^{-2}$) is pre-deposited on the samples for the formation of Li metal composite anode. Electrochemical impedance spectroscopy is conducted using a CHI760E electrochemical instrument. The EIS analysis covers a frequency range spanning from 100 kHz to 10 mHz, employing a small amplitude of 5 mV.

### 4.3 Materials characterization of Cu2O dendrites current collector

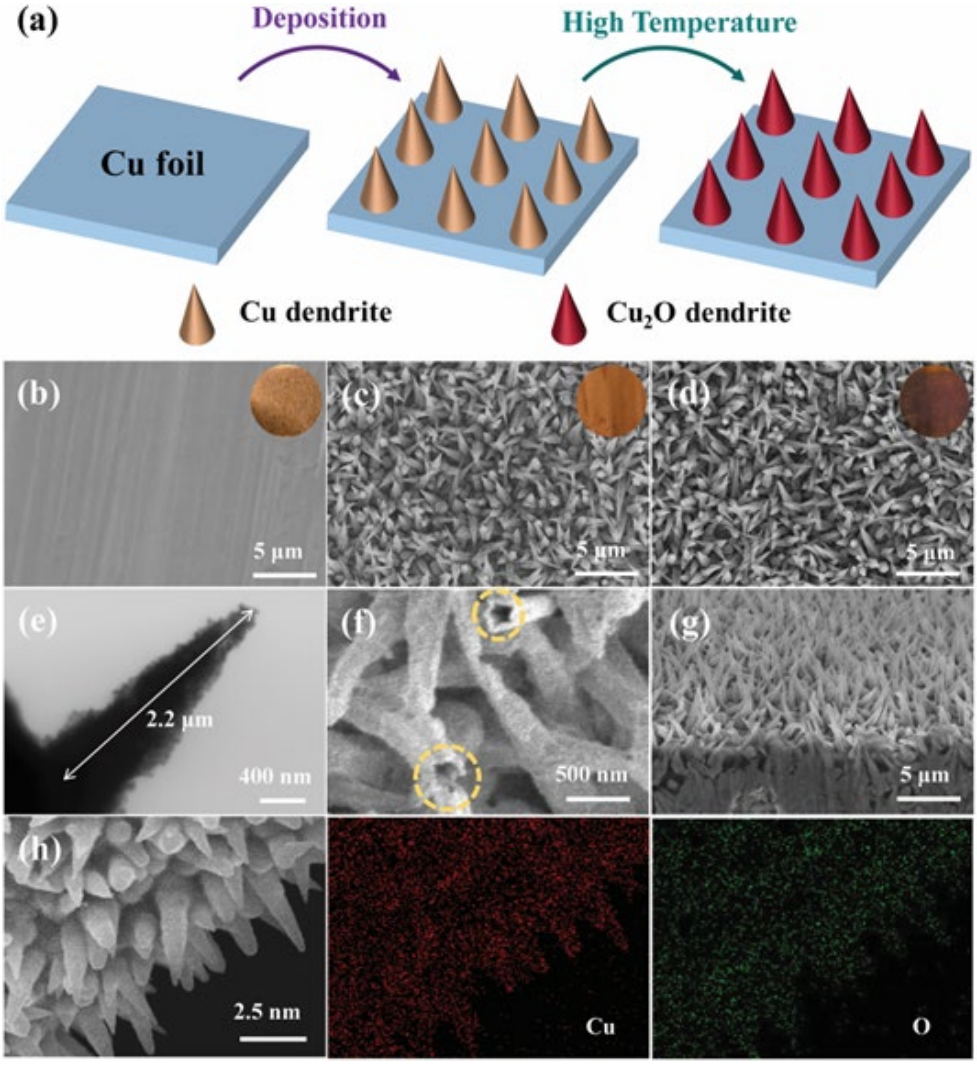


**Figure 4.1** (a) Schematic diagram of the production process of $Cu_2O$ dendrite. Top-view SEM images of pristine Cu foil (b), Cu dendrite (c), and $Cu_2O$ dendrite (d). (e) STEM image of an individual $Cu_2O$ dendrite. (f) SEM image of the fractured $Cu_2O$ dendrite. (g) Cross-section SEM image of $Cu_2O$ dendrite. (h) SEM image and corresponding elemental (Cu, O) mapping of $Cu_2O$ dendrite.

The process for synthesizing $Cu_2O$ dendrites is outlined in Figure 4.1 a. $Cu_2O$ dendrites are generated using a streamlined electrodeposition technique, succeeded by a direct heat treatment process. Top-view scanning electron microscopy (SEM) images sequentially unveil copper foil, copper dendrites, and cuprous oxide dendrites in Figure 4.1 b-d. The smooth and flat surface of the Cu foil, as depicted in Figure 4.1 c, is conspicuously adorned with dense copper dendrites. Post heating treatment, copper (Cu) on the surface of the copper dendrites undergoes a transformation into cuprous oxide ($Cu_2O$). Notably, this transformative process exerts negligible influence on the morphological characteristics, a phenomenon visually affirmed in Figure 4.1 d. Moreover, EDX mapping of the $Cu_2O$ dendrites distinctly presents a uniform distribution of copper and oxygen, thus confirming the presence of $Cu_2O$. Furthermore, the embedded optical photographs in Figure 4.1 b-d sequentially demonstrate a color transition of the sample surface from bright yellow to dark yellow and ultimately to dark red. This progression serves as conclusive evidence for the generation of Cu dendrites and the formation of the $Cu_2O$ layer. Cross-sectional SEM images of the $Cu_2O$ dendrite electrode are captured, revealing a substantial deposition of $Cu_2O$ dendrites on the smooth copper foil surface, as evident in the comparison between Figure 4.2 b, e. High-magnification cross-sectional SEM images in Figure 4.1 g and Figure 4.2 f illustrate the staggered stacked $Cu_2O$ dendrites on the Cu foil surface. This cross-stacked architecture not only provides ample space for the current collector to accommodate Li metal but also augments the specific surface area, effectively reducing the areal current density. The SEM images in Figure 4.2 a, d showcase the morphology of Cu foil and $Cu_2O$ dendrites at low magnification. An individual cuprous oxide dendrite, illustrated in Fig. 1e with a length of 2.2 μm.

Notably, the fractured cuprous oxide dendrite within the yellow dash circle in Figure 4.1 f and Figure 4.2 c reveals a hollow structure. This distinctive feature significantly mitigates the whole weight of the electrode compared to conventional solid 3D copper array current collectors documented in the literature [213, 214], presenting a highly favorable characteristic for enhancing the energy density of commercial battery cells.

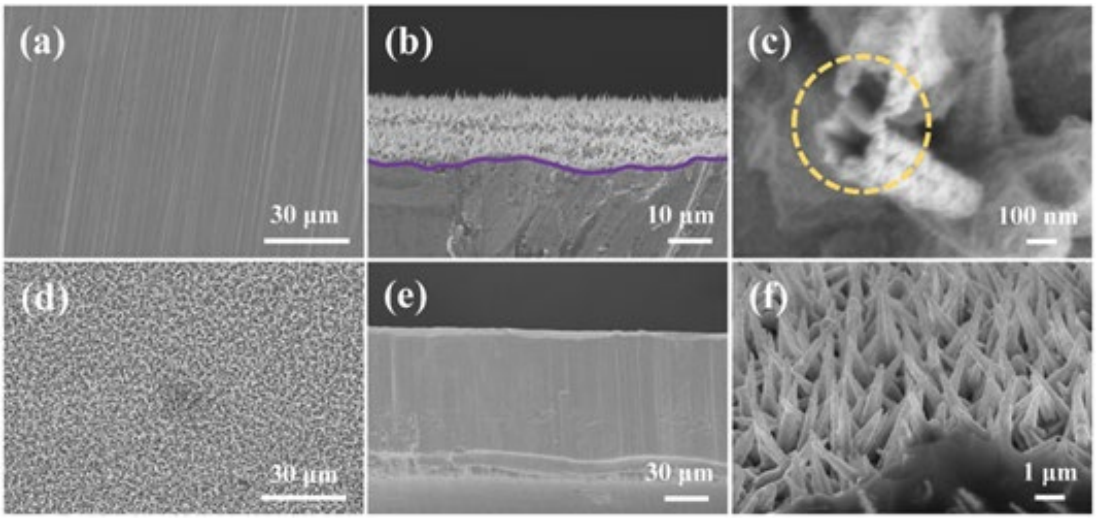


**Figure 4.2** Top-view SEM images of (a) Cu foil and (d) $Cu_2O$ dendrite electrode. Cross-section SEM images of (e) Cu foil and (b) Cu2O dendrite. (c) SEM image of the fractured $Cu_2O$ dendrite. (f) Cross-section SEM images of $Cu_2O$ dendrites at high magnification.

The X-ray diffraction (XRD) patterns for both copper foil and copper dendrites are presented in Figure 4.3 a and Figure 4.4 a, respectively. Their respective peak positions at 43.3°, 50.4°, and 74.1° align with the standard patterns documented in the Powder Diffraction File (PDF) card (#04-0836) [196]. Notably, the XRD pattern of $Cu_2O$ dendrites at 36.4°, 42.3°, 61.3°, and 73.5° impeccably mirrors the standard peak positions provided by the PDF card (#05-0667) [211], as exemplified in Figure 4.3 a. To delve

further into the characterization, X-ray photoelectron spectroscopy (XPS) analyses of $Cu_2O$ dendrite are executed, with the results thoughtfully delineated in Figure 4.4 b. The discerned binding energies at 933.9 eV and 953.8 eV correlate with Cu+, while those at 932.6 eV and 952.6 eV correspond to Cu0, a consistent observation in alignment with established findings in prior literature [215]. In Li metal batteries, the lithiation process, constituting the initial discharge to 0 V, unfolds. This intricate transformation involves the reaction of cuprous oxide with lithium, resulting in the formation of lithium oxide and copper. The consequential XRD curve of the lithiated cuprous oxide current collector, eloquently depicted in Figure 4.3 b, unveils distinctive peaks at 33.6° and 36.2°—typical markers of lithium oxide and metallic lithium, respectively [210]. This experimental evidence unequivocally validates the transmutation expressed by the reaction equation [208]:

$$Cu_2O + Li \rightarrow Li_2O + Cu$$

Furthermore, the curves gleaned from Figure 4.8 a elucidate that cuprous oxide dendrites underwent prolonged discharge, signifying heightened lithium consumption and the consequent formation of a $Li_2O$ layer. This layer, characterized by favorable ionic conductivity and electronic insulation properties, emerges as a facilitator for the diffusion of lithium ions at the interface.

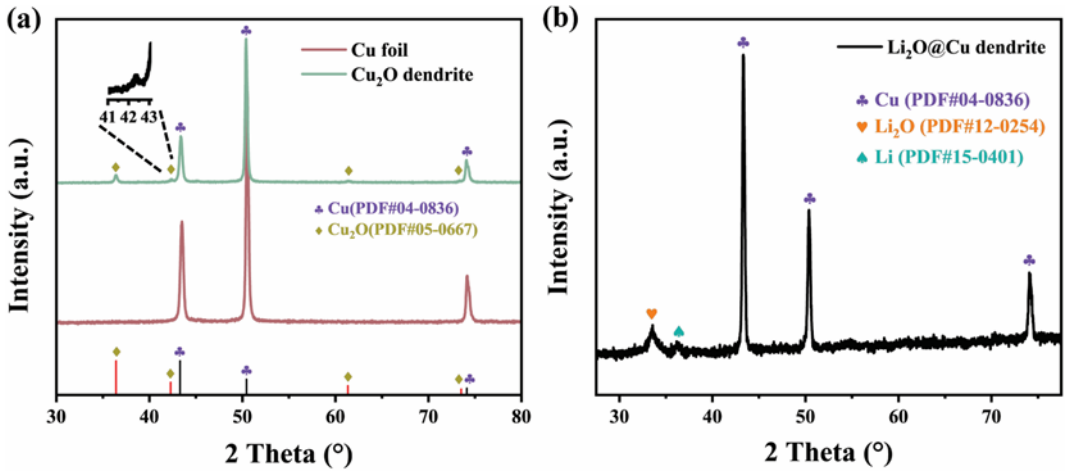


**Figure 4.3** (a) XRD patterns of the prepared $Cu_2O$ dendrite, with Cu foil as a control sample. (Inset of a) enlarged image of the XRD peak of $Cu_2O$ dendrite at 42.5°. (b) XRD patterns of $Li_2O$@Cu dendrite created in the lithiation process.

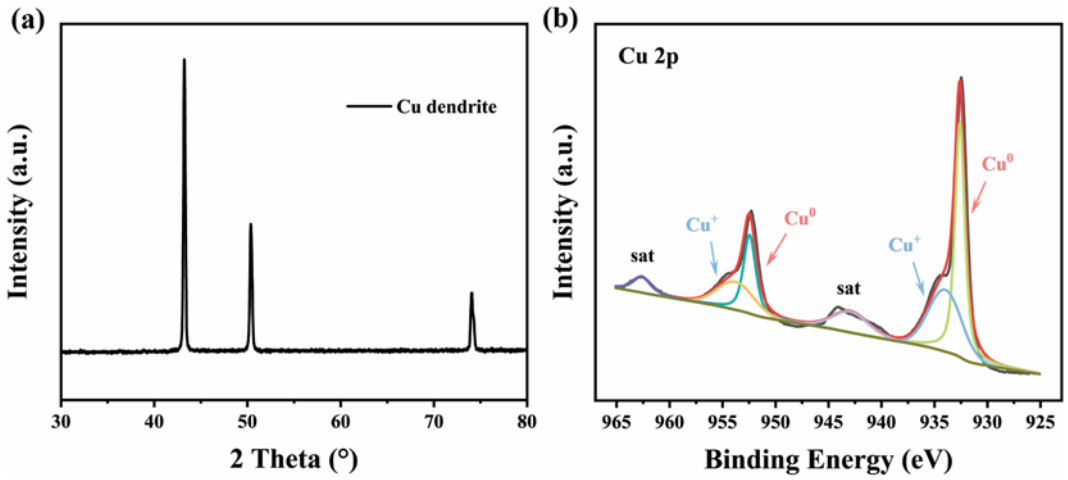


**Figure 4.4** The XRD pattern of prepared Cu dendrite. Cu 2p XPS spectrum of $Cu_2O$ dendrite.

### 4.4 Morphology of Li metal

The investigation of lithium metal deposition/stripping dynamics during the inaugural cycle stands as a pivotal metric for gauging performance excellence. As such, the evolution in lithium metal morphology throughout the initial cycling is scrutinized through ex-situ SEM, illustrated in Figure 4.5 The applied current density is set at 1 mA $cm^{-2}$, with each charge and discharge cycle extending over a duration of 1 h. Figure 4.5 a-e compellingly reveals that, owing to the presence of a special $Cu_2O$ layer on the surface, lithium metal exhibits a tendency to gravitate toward $Cu_2O$, manifesting a proneness to preferential growth on the surface of $Cu_2O$ dendrites, thereby submerging the $Cu_2O$ dendrites. Notably, the initially sharp tips of cuprous oxide dendrites undergo a transformative shift, yielding to a columnar coral morphology. This evolution is conspicuous during the early stages of lithium deposition. As the deposition progresses, uniformly sized lithium nuclei blanket the cuprous oxide dendrites, progressively enlarging with continued deposition. The subsequent stripping stage witnesses a gradual reduction in the lithium nuclei size, akin to a deflating balloon, until its complete disappearance, laying bare the lithiated cuprous oxide dendrites upon completion of the charging process. This morphological evolution of lithium metal unequivocally underscores the reversible nature of the deposition/stripping process on the cuprous oxide dendrite current collector. In contrast, lithium metal deposited on copper foil exhibits a distinct behavior. In early stages, varying-sized lithium nuclei emerge, culminating in the generation of a multitude of lithium dendrites as the deposition capacity expands. Notably, even after peeling off, a substantial presence of dendrites persists, signaling a substantial retention of lithium metal on the copper foil. Regrettably, this

deposition/stripping behavior proves irreversible upon the completion of the cycling process. Furthermore, the examination of the morphology of the electrode surface after 20 and 50 cycles, as depicted in Figure 4.6, unveils a stark dichotomy. The $Cu_2O$ dendrite electrode maintains a relatively flat and clean surface. Conversely, the copper foil bears witness to the emergence of a multitude of lithium dendrites and dead lithium after 20 and 50 cycles. Significantly, these dead Li, excluded from active participation in electrochemical reactions, exert a detrimental influence on overall electrochemical performance.

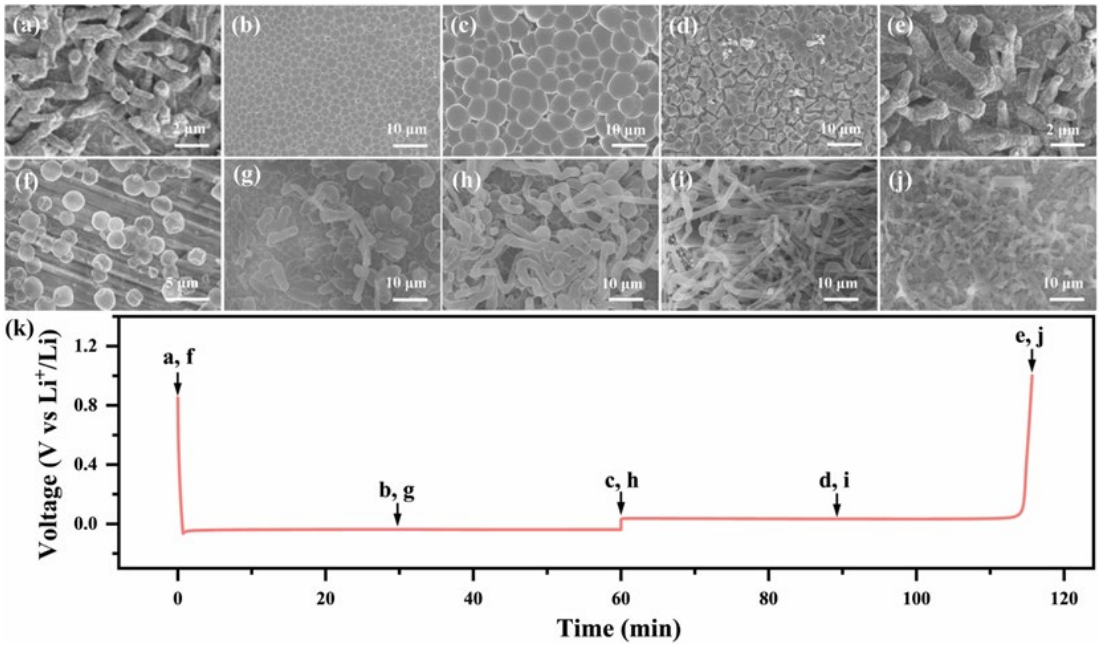


**Figure 4.5** The top-down SEM images of $Cu_2O$ dendrite (a-e) and Cu foil (f-j) after plating and stripping at different lithium capacities. (k) Corresponding points at voltage curves of electrodes at 1 mA $cm^{-2}$.

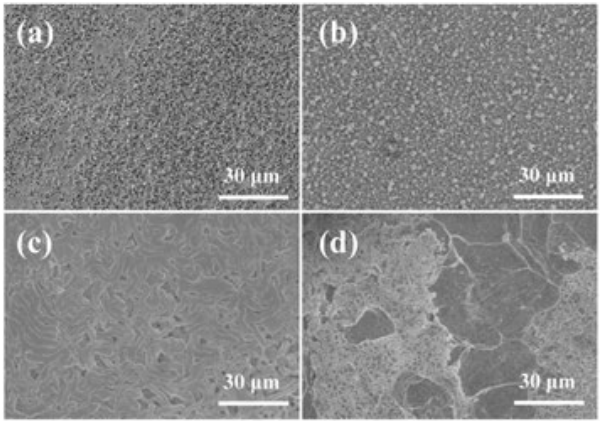


**Figure 4.6** Top-view SEM images of $Cu_2O$ dendrite after 20 (a) and after 50 (b) plating/stripping cycles at a current density of 1 mA $cm^{-2}$ with a capacity of 1 mAh $cm^{-2}$. Top-view SEM images of Cu foil after 20 (c) and after 50 (d) plating/stripping cycles at a current density of 1 mA $cm^{-2}$ with a capacity of 1 mAh $cm^{-2}$.

Drawing on the insights gleaned from the preceding results, Figure 4.7 tenders a comprehensive depiction of the deposition/stripping behavior mechanism of lithium on copper foil and cuprous oxide dendrites. On the copper foil electrodes, lithium metal manifests an uneven deposition in the initial stages, evolving into lithium dendrites as the cycling process unfolds. This erratic behavior is attributed to the planar structure and lithiophobic tendencies inherent in copper foil. Contrastingly, the lithiation process enables the reaction between $Cu_2O$ and metallic lithium, giving rise to the in-situ formation of a $Li_2O$ layer, which facilitates the rapid passage of lithium ions through the interface. Lithium metal exhibits uniform nucleation on the $Cu_2O$ dendrite current collector, growing densely and uniformly with the progression of deposition. This marked difference can be attributed to the larger surface area resulting from the 3D structural properties of $Cu_2O$ dendrites and the minimal nucleation overpotential benefiting from the inherent lithiophilicity of $Cu_2O$.

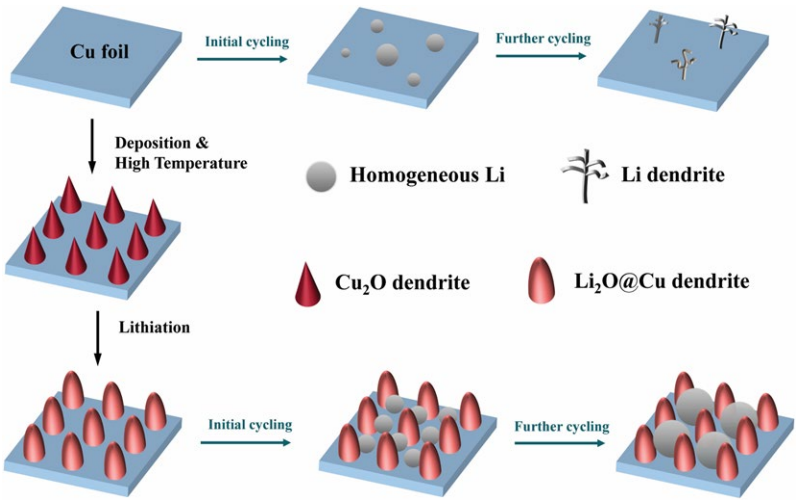


**Figure 4.7** Schematic diagram of the lithiation process of electrodes and the Li deposition behaviors on the bare Cu foil (top) and $Cu_2O$ dendrite (bottom) current collectors.

## 4.5 Electrochemical performance of $Cu_2O$ dendrite current collector

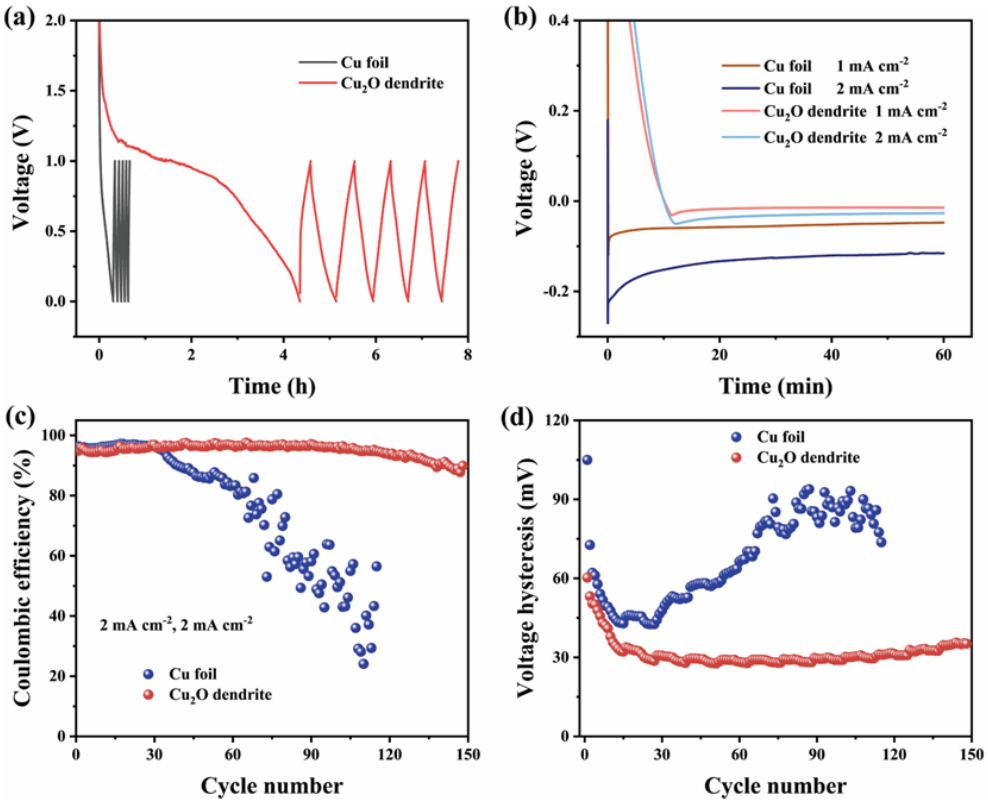

**Figure 4.8** (a) Discharging curves of the initial process at 0.05 mA $cm^{-2}$. (b) Voltage profiles of Cu foil and $Cu_2O$ dendrite showing nucleation potential and deposition platform in the first cycle. (c) The comparison of the CE of two electrodes at 2 mA $cm^{-2}$ with a charging/discharging time of 1 h, and (d) corresponding voltage hysteresis.

The voltage-time curve delineated in Figure 4.8 b encapsulates a discernible voltage dip attributed to lithium metal nucleation and a subsequent voltage plateau associated with lithium metal growth. The disparity between the nadir of this voltage drop and the voltage plateau is defined as the nucleation overpotential [216, 217], signifying the nucleation barrier for lithium metal. Notably, the nucleation overpotential is contingent not only upon the applied current density but also on the lithophilic degree of the electrode surface. Evidently, whether on copper foil or $Cu_2O$ dendrites, the nucleation overpotential at 1 mA $cm^{-2}$ is markedly smaller than that observed at 2 mA $cm^{-2}$. Furthermore, under identical current densities, the nucleation overpotential of the $Cu_2O$ dendrite electrode is substantially diminished compared to that of copper foil. This substantiates that the surface modification involving cuprous oxide effectively enhances the lithophilicity of the substrate, thereby mitigating the nucleation barrier for lithium metal.

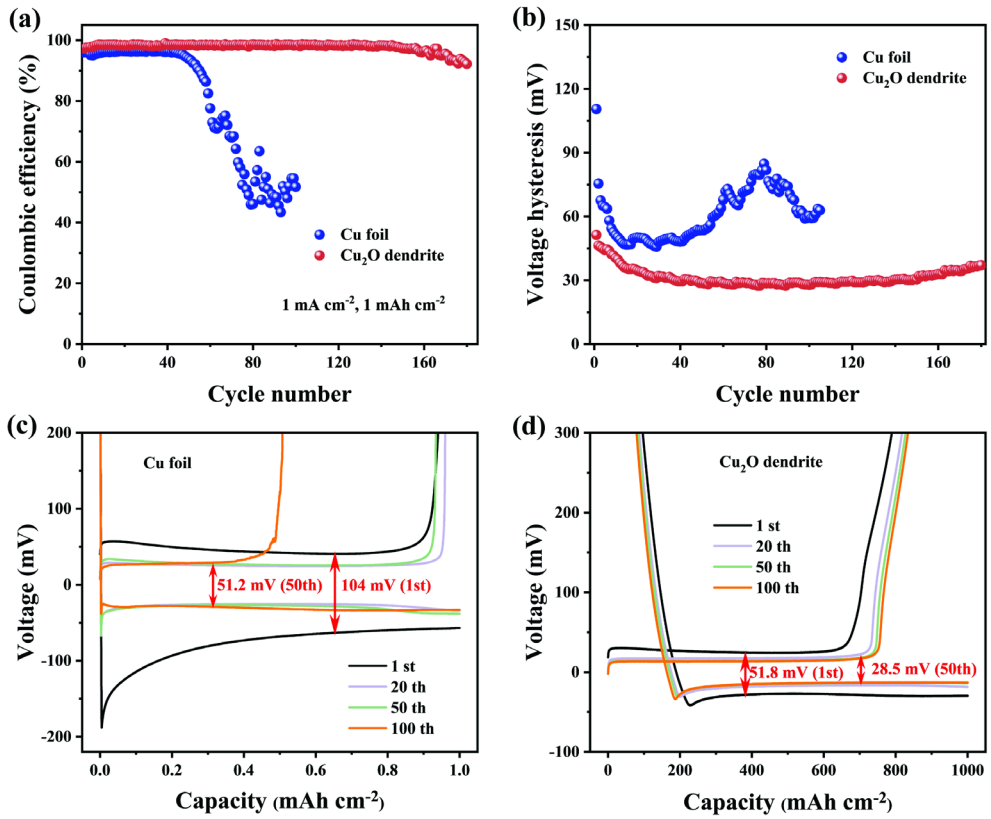


**Figure 4.9** (a) The comparison of the CE of two electrodes at 1 mA $cm^{-2}$ with a charging/discharging time of 1 h, and (b) corresponding voltage hysteresis. (c, d) Plating/stripping profiles of Cu foil (c) and $Cu_2O$ dendrite (d) at various cycles under 1 mA $cm^{-2}$.

Coulombic efficiency and corresponding voltage hysteresis were examined in a half-cell configuration featuring lithium foil as the counter electrode. The working electrodes under scrutiny were copper foil and cuprous oxide dendrites, facilitating a comprehensive comparative analysis. At a current density of 1 mA $cm^{-2}$ and a charge-discharge time of 1 h, detailed in Figure 4.9 a, the $Cu_2O$ dendrite electrode exhibited an initial Coulombic Efficiency (CE) of 97.3%, maintaining a commendable CE of 98.2% over 180 cycles. In contrast, the copper foil electrode displayed a lower initial CE, experiencing a precipitous

and continuous decline of CE after 45 cycles. In Figure 4.9 b, the voltage hysteresis of the copper foil initially diminished due to the dissolution of an intrinsic surface oxide layer. However, after 40 cycles, a sharp increase ensued, attributed to the accumulation of an unstable and non-conductive Solid Electrolyte Interphase (SEI) film. Conversely, the voltage hysteresis of cuprous oxide dendrites remained consistently smaller in the initial stages and exhibited stability throughout the cycling process. Upon escalating the current density to 2 mA $cm^{-2}$ and the capacity density to 2 mAh $cm^{-2}$, the cuprous oxide electrode showcased a remarkable CE of 96.2% after 150 cycles, markedly outperforming the transient stability of the copper foil over a mere 30 cycles, as depicted in Figure 4.8 c. Simultaneously, the voltage hysteresis of cuprous oxide dendrites, illustrated in Figure 4.8 d, was significantly lower than that of the Cu foil, indicating reduced polarization in the battery employing the proposed electrode. Even under a heightened current density of 3 mA $cm^{-2}$, maintaining a charge and discharge time of 1 h, the cuprous oxide dendrite electrode sustained a 94% CE over 110 cycles, demonstrating substantial advantages, as evidenced in Figure 4.10. Conversely, the CE of the half-cell employing copper foil exhibited fluctuations after a mere 22 cycles. The voltage-capacity curves of both electrodes during the $1^{st}$, $20^{th}$, $50^{th}$, and $100^{th}$ cycles are delineated in Figure 4.9 c, d. Notably, the cuprous oxide dendrite electrode showcased a voltage hysteresis of 51.8 mV in the $1^{st}$ cycle, diminishing to 28.5 mV in the $100^{th}$ cycle. This stands in obvious contrast to the voltage hysteresis of 104 mV in the initial cycle, declining to 51.2 mV in the $100^{th}$ cycle in the copper foil-based battery. These enhanced electrochemical properties affirm that the cuprous oxide dendrite electrode fosters an improved interface, a stable SEI film, and lower reaction polarization.

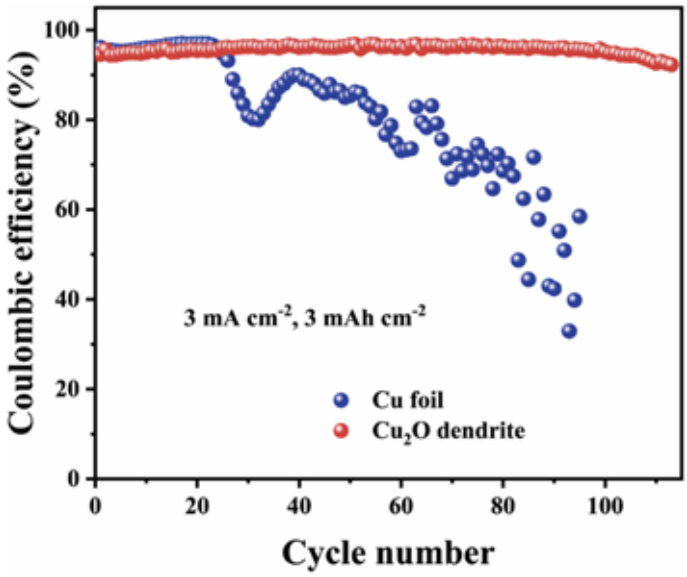


**Figure 4.10** Coulombic efficiencies (CEs) for Li plating/stripping cycling on two electrodes at current densities of 3 with a capacity of 3 mAh $cm^{-2}$.

The Nyquist curves presented in Figure 4.11 a, b offer a comprehensive information about the electrochemical interfacial behavior of both copper foil and cuprous oxide dendrites at various stages: before cycling, after the 1st cycle, post the 20th cycle, and subsequent to the 80th cycle. Examining the semicircle in the initial segment of the horizontal axis, which signifies the interface impedance of the electrode/electrolyte, one gains information about the stability of the SEI film. Before cycling to after the 20th cycle, the interface resistance of the copper foil exhibits a declining trend, attributable to the deposition of Li metal on the electrode surface. However, the increase in impedance observed from the 20th to the 80th cycle is ascribed to the destabilization of the SEI film and the concomitant growth of Li dendrites. Conversely, the interfacial resistance of $Cu_2O$ dendrite consistently outperforms that of Cu foil across different cycles, indicating a more stable interface, and uniform lithium deposition/stripping behavior. Moreover, the interface resistance of $Cu_2O$ dendrite undergoes a reduction with cycling, signifying the

development of a stable SEI film during the cycling. This further underscores the superior electrochemical performance and enhanced stability of $Cu_2O$ dendrite electrode as a promising electrode material.

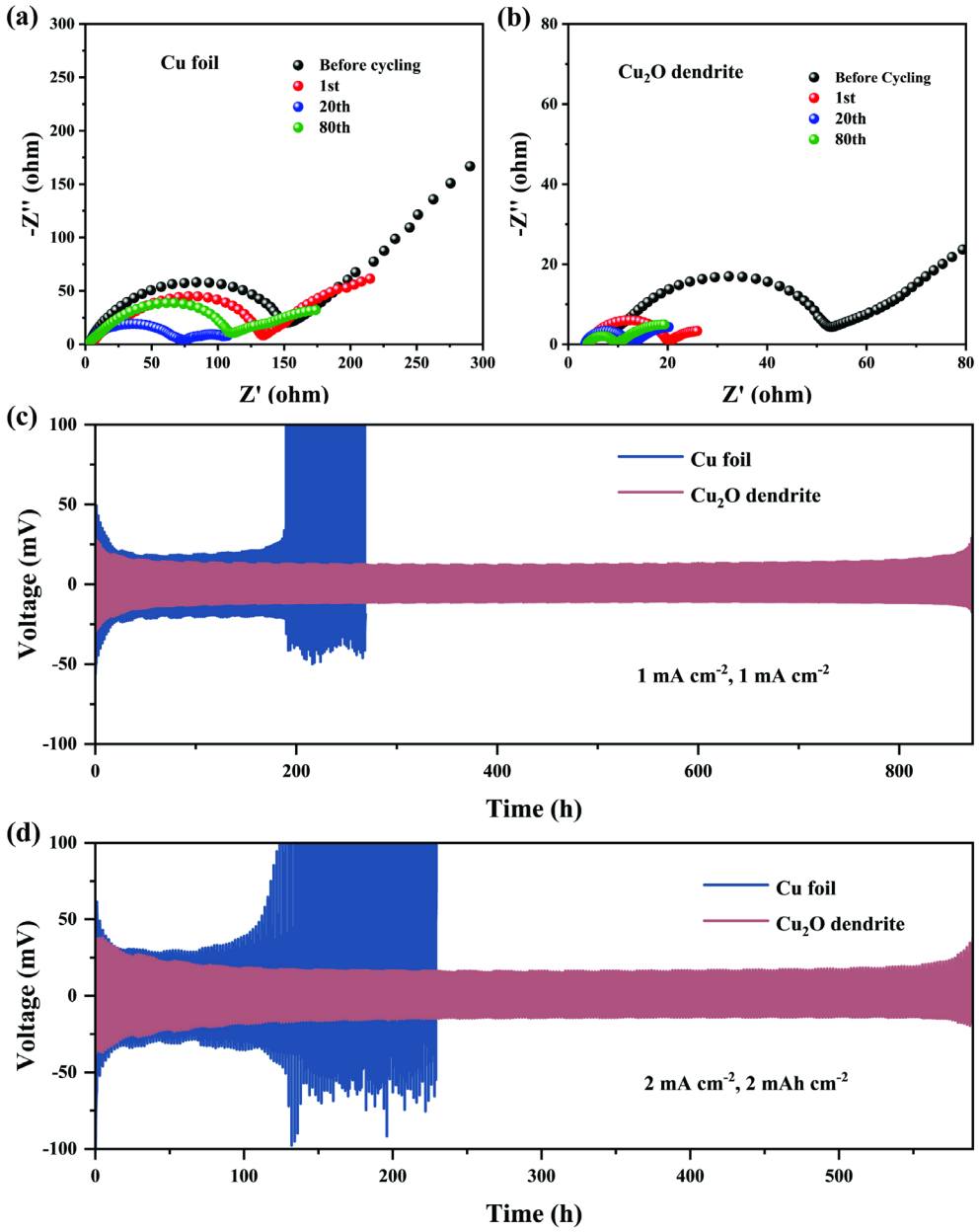


**Figure 4.11** (a) EIS curves for different cycles of half cells with (a) Cu foil and (b) $Cu_2O$ dendrite at 1 mA $cm^{-2}$. Voltage-time curves of symmetric cells with Cu foil and Cu2O dendrite at (c) 1 mA $cm^{-2}$ and (d) 2 mA $cm^{-2}$ with a charging/discharging time of 1 h.

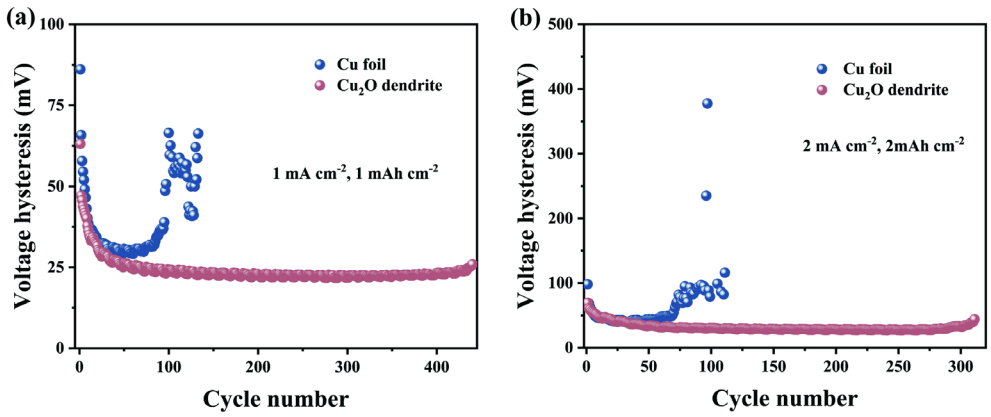


**Figure 4.12** Voltage hysteresis for Li plating/stripping cycling on two electrodes at various current densities of (a) 1 and (b) 2 with a charging/discharging time of 1 h.

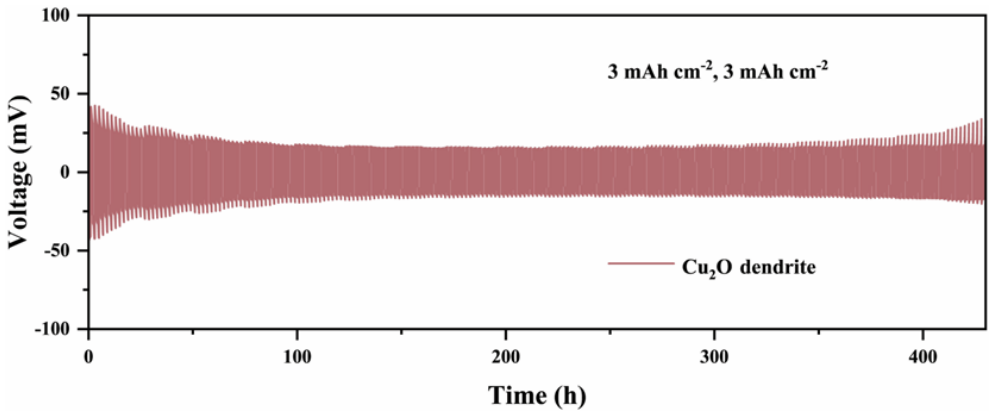


**Figure 4.13** Cycling stability of symmetrical cells with $Cu_2O$ dendrite at current densities of 3 mA $cm^{-2}$ with a capacity density of 3 mAh $cm^{-2}$.

The cycling stability of $Cu_2O$ dendrites is assessed by predepositing a specific quantity of Li on the current collector, followed by the assembly of symmetrical cells with lithium foil. The galvanostatic charge-discharge cycling tests are applied to a symmetrical cell. In Figure 4.11 c, d, it is evident that the cuprous oxide dendrite electrode demonstrates exceptional cyclic stability, sustaining continuous stable cycling for 880 h and 600 h at 1 and 2 mA $cm^{-2}$, respectively, with a charge and discharge duration of 1 h. Notably, the

voltage plateau remains remarkably stable throughout these extended cycles, underscoring the reliability and longevity of cuprous oxide dendrites as an electrode material. In contrast, the copper foil electrode exhibits a notable increase in voltage at 180 h and 100 h under equivalent conditions, accompanied by voltage fluctuations. Additionally, the charge-discharge voltage platform of $Cu_2O$ dendrites is significantly smaller than that of copper foil, indicative of lower reaction polarization. The voltage hysteresis depicted in Figure 4.12 further verifies this point, revealing that the $Cu_2O$ dendrite electrode manifests smaller and more stable voltage polarization, thereby signifying a stable electrode interface and controllable lithium deposition. Even under more demanding conditions with increased current and capacity density (3 mA $cm^{-2}$, 3 mAh $cm^{-2}$), the cuprous oxide dendrite electrode demonstrates exceptional stability, cycling for 430 h without succumbing to severe polarization or short circuits, as shown in Figure 4.13. This impressive performance attests to the remarkable cycling stability and robust electrochemical behavior of cuprous oxide dendrites, reinforcing their potential as a superior electrode material.

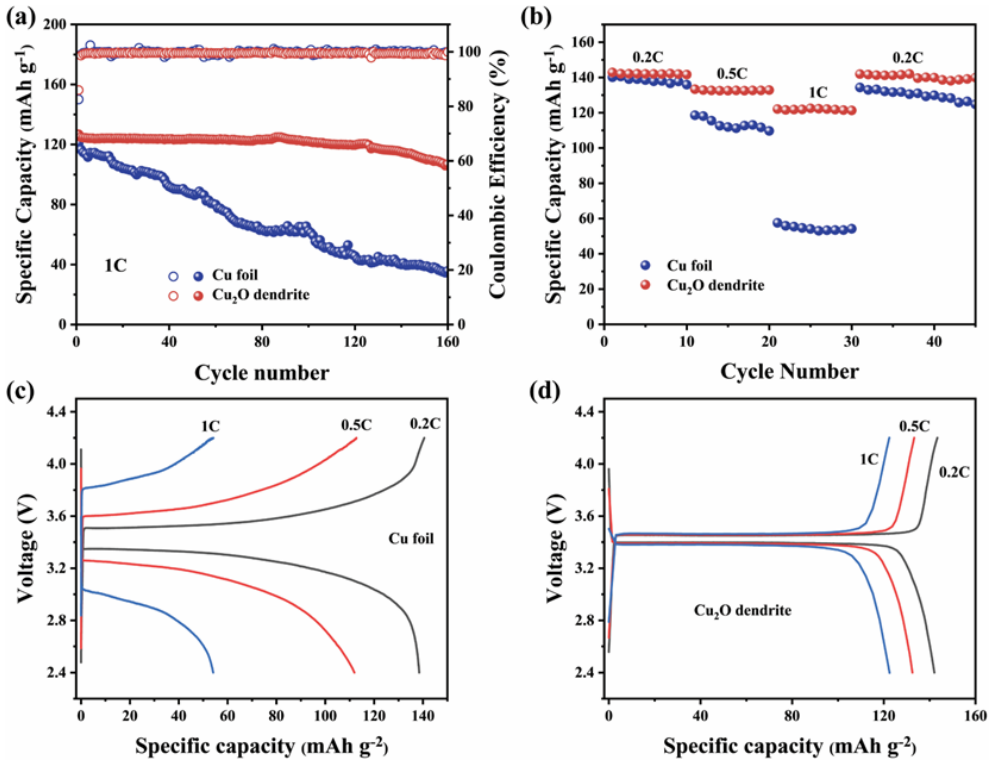


**Figure 4.14** (a) Cycling performance of full cells with Cu foil and $Cu_2O$ dendrite current collectors coupling with LFP at 1 C. (b) Rate capability comparison of full cells, and the corresponding voltage-capacity profiles of full cells with (c) Cu foil and (d) $Cu_2O$ dendrite at various rates.

The comprehensive electrochemical performance of cuprous oxide dendrite electrodes in full cells was systematically examined in couple with an LFP cathode. Prior to cycling, 3 mAh $cm^{-2}$ of lithium metal was strategically deposited on both copper foil and $Cu_2O$ dendrite current collectors, resulting in the formation of Li/Cu foil and Li/$Cu_2O$ dendrite composite electrodes. Evidently, the Li/$Cu_2O$ dendrite-based full cell exhibits remarkable stability, cycling for 160 cycles while maintaining an impressive capacity retention rate of 84%, as shown in Figure 4.14 a. In contrast, the capacity of the Li@Cu foil-based full cell experiences a rapid decline with cycling, culminating in a capacity retention rate of

only 28% after 160 cycles. This stark discrepancy in performance highlights the superior electrochemical stability and longevity offered by cuprous oxide dendrites as an electrode material. The rate performance of the samples at different rates, as depicted in Figure 4.14 b, underscores the favorable attributes of the Li/$Cu_2O$ dendrite-based full cell. Particularly notable is its superior performance between 0.2 C and 1 C, indicating rapid lithium ions diffusion kinetics—a characteristic in harmony with the interfacial impedance results. Upon reverting to a 0.2 C rate, the Li/$Cu_2O$ dendrite-based full cell remarkably maintains 98.3% of its initial capacity, affirming its exceptional cycle reversibility. Examining the charge-discharge curves at different rates (Figure 4.14 c, d), the Li/$Cu_2O$ dendrite-based full cell exhibits a distinct voltage plateau and lower voltage polarization. This observation underscores the pronounced suppression of lithium dendrites by the Li/$Cu_2O$ dendrite electrode, ensuring swift reaction kinetics. Furthermore, the comparison of charge and discharge curves under different cycles (Figure 4.15) consistently reaffirms these performance differentials. Collectively, these substantial enhancements in electrochemical performance underscore the practical viability and potential applications of $Cu_2O$ dendrite electrodes as stable lithium metal electrodes.

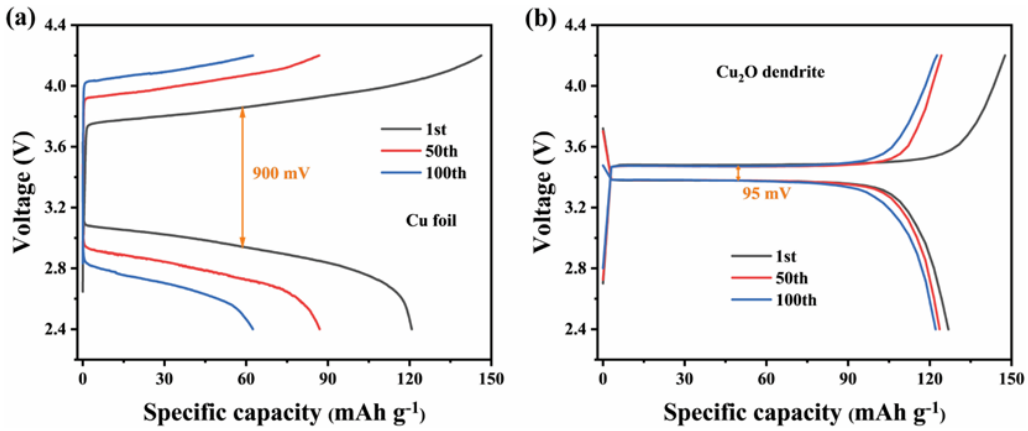

**Figure 4.15** Voltage-capacity curves of full cells with (a) Cu foil and (b) $Cu_2O$ dendrite at various cycles from 1st to 100th.

### 4.6 Conclusions

In conclusion, we fabricate $Cu_2O$ dendrites on flat copper foil via a readily scalable two-step methodology involving electrodeposition and high-temperature treatment. The three-dimensional architecture engendered by the distinctive staggered stacking of $Cu_2O$ dendrites affords ample space for the electrode to house lithium metal, effectively curtailing the challenges associated with the infinite volume expansion of Li metal. The lithophilic properties of $Cu_2O$ layer enhance the even deposition/stripping of lithium metal owing to the robust binding energy between Li and $Cu_2O$. The resulting thin lithium oxide layer post-lithiation further facilitates the kinetics of lithium ions diffusion at the solid-liquid interface. Leveraging these attributes, the $Cu_2O$ dendrite current collector demonstrates enduring cycling stability exceeding 880 h and a minimal voltage hysteresis of 21.8 mV. Moreover, the $Cu_2O$ dendrite-based full cell showcases outstanding capacity retention and remarkable rate performance at 1 C. This investigation illuminates a direction toward prospective applications of Li metal anodes (LMA) in forthcoming high-energy battery technologies.

# CHAPTER 5 CONCLUSION AND FUTURE WORK

## 5.1 Conclusions

Cu pyramid array (CPA) with 3D porous structure has been prepared as a 3D host for Li metal anodes employing the facile, and economical electrodeposition method. Such current collector possesses the following advantages: (1) Nano-pyramid arrays can enlarge the surface area and reduce the local current density. (2) The spaces between the arrays provide sufficient sites to accommodate Li metal. (3) The preparation technology adopted is simple, facile, and cost-effective, which contributes to large-scale commercialization. Owing to these properties, CuPA based electrode exhibits extremely low overpotential, superior Coulombic efficiency (CE) and durable cycling stability. In addition, Li@CuPA based full cell also demonstrates outstanding cycling stability and superior rate performance. More importantly, such a simple, direct, and inexpensive preparation procedure is very conducive to large-scale practical applications.

Based on the lithiophobicity of the copper substrate, we fabricated a 3D host for Li metal anodes by preparing a gold layer-modified pentagonal pyramid structured Cu array (Au@CuPPA) through a facile combination of electrodeposition and chemical reduction methods. This current collector offers several advantages: (1) Nano-pyramid arrays increase the surface area, reducing local current density. (2) The Au-enhanced Li affinity guides the diffusion channel of Li metal, preventing underutilization of the nano-porous structure. (3) Empty spaces between arrays provide ample sites for Li metal accommodation. As a result, the Au@CuPPA electrode demonstrates minimal overpotential, exceptional Coulombic efficiency (CE), and sustained cycling stability. Furthermore, a full cell based on Li@Au@CuPPA exhibits outstanding cycling stability

and superior rate performance. This study introduces a novel 3D nano-pyramid structured current collector with a lithiophilic layer, achieving remarkable electrochemical performance for Lithium Metal Batteries (LMBs).

For large-scale application considerations, we demonstrate a novel strategy to inhibit lithium dendrite growth by depositing staggered stacked $Cu_2O$ dendrites on the surface of planar copper foil. The three-dimensional structure, along with the lithiophilic nature of $Cu_2O$, effectively retards the volume expansion of lithium metal, fostering highly reversible, dendrite-free lithium deposition/stripping behavior. The thin $Li_2O$ derived from $Cu_2O$ enhances $Li^+$ diffusion at the interface due to its low oxygen content. Additionally, the hollow structure of $Cu_2O$ dendrites addresses the weight issue of the current collector, contributing to improved energy density. The $Cu_2O$ dendrite electrode demonstrates enhanced nucleation overpotential and reduced interfacial resistance. This study delves into the rational design of the composition and structure of lithiophilic phases on the surface of current collector to achieve dendrite-free lithium metal anodes, offering inspiration for the development of next-generation high-energy-density rechargeable lithium metal batteries (LMB).

The fabricated current collector underwent characterization through SEM, XRD, and XPS. Electrochemical tests were conducted to analyze Coulombic efficiency, lithium metal battery deposition/stripping stability, as well as the cycle stability and rate performance of the full cell.

The key findings are summarized as follows:

(1) The simple electrodeposition method prepared CPA@CF with three-dimensional structure for lithium metal anode. Ex-XRD analysis reveals the phase composition of the

CPA@CF electrode. Ex-SEM images further demonstrate the stability of lithium metal growth on the surface of CPA@CF, with no dendrite formation observed.

(2) The CPA@CF current collector enables a consistently even Li plating/stripping process for up to 360 hours. The Li@CPA@CF|$LiFePO_4$ full cell exhibits outstanding electrochemical performance, achieving an excellent Coulombic efficiency (CE) of 99.3% over 160 cycles at 0.3 C, accompanied by a superior capacity retention of 84.2%.

(3) The pentagonal pyramid array structure of Au@CuPPA offers a substantial specific surface area for the electrode, effectively decreasing interface impedance. Furthermore, owing to the gold layer modification, Au@CuPPA demonstrates an exceptionally low nucleation overpotential of 12 mV at a current density of 1 mA $cm^{-2}$.

(4) The morphological evolution of lithium metal on the Au@CuPPA electrode surface is controllable, consistently maintaining a spherical shape. The Au@CuPPA substrates exhibit outstanding Coulombic efficiency of 96.8% over 137 cycles, showing long-term cycling stability for over 460 hours at 3 mA $cm^{-2}$.

(5) Strong adsorption energy between $Cu_2O$ and Li atoms enables uniform Li plating/stripping behaviors. The deposition of staggered stacks of $Cu_2O$ dendrites yields a three-dimensional structure, enhancing the specific surface area and optimizing the space utilization of the current collector.

(6) The $Li_2O$ layer, derived in situ from $Cu_2O$, establishes a rapid pathway for the diffusion of lithium ions at the solid-liquid interface. The hollow structure of $Cu_2O$ effectively diminishes the overall mass of the current collector, thereby contributing to the enhancement of the energy density of the battery cells.

(7) In symmetrical cells using $Cu_2O$ dendrite-based lithium metal anodes, continuous operation at a current density of 1 mA $cm^{-2}$ and a capacity of 1 mAh $cm^{-2}$ is sustained for 880 hours without encountering short circuits.

(8) In the full cells, employing Li/$Cu_2O$ dendrite electrode, an exceptional Coulombic efficiency (CE) of 99.9% is attained after 160 cycles at 1 C, coupled with an admirable capacity retention rate of 84%.

**5.2 Significance**

The electrodeposition method holds significant importance in preparing current collectors for several reasons. Firstly, it provides a versatile and controllable approach, allowing precise tuning of the current collector's properties such as morphology and composition. Secondly, electrodeposition enables the deposition of uniform and well-adhered coatings, ensuring enhanced stability and performance. Additionally, this method is relatively cost-effective and scalable, making it practical for large-scale production. Overall, the electrodeposition method is instrumental in tailoring current collectors with desired characteristics, contributing to advancements in various electrochemical applications, including batteries and sensors.

Surface treatment using chemical reduction and high-temperature treatment holds significant importance in enhancing material properties for various applications. Chemical reduction, often involving the use of reducing agents, enables the modification of surface chemistry, introducing functional groups or coatings. This process can improve the material's reactivity, or electronic properties. High-temperature treatment contributes to the structural and morphological changes of materials. It can lead to crystallinity

enhancement, phase transformation, and the removal of impurities, resulting in improved mechanical strength, thermal stability, and conductivity.

The significance of an optimized current collector lies in its crucial role within electrochemical devices, particularly in energy storage systems. An optimized current collector can positively impact several key aspects:

These innovative current collectors in this dissertation represent a crucial advancement that addresses key challenges associated with the utilization of lithium metal anodes. By introducing a novel design, the proposed current collector promises to enhance the overall performance and safety of lithium-ion batteries. Its innovative features are poised to mitigate issues such as dendrite formation, uneven deposition, and unstable cycling that have traditionally plagued lithium metal anodes. This breakthrough is particularly impactful in advancing the energy density and efficiency of lithium-ion batteries, contributing to the development of high-performance and reliable energy storage systems.

The significance of this dissertation for a Li metal anode lies in its potential to revolutionize lithium-ion battery technology, addressing critical challenges and paving the way for more efficient, reliable, and environmentally friendly energy storage solutions.

### 5.3 Future work

The future work for this dissertation will involve measuring the performance of current collectors within pouch cells, leveraging optical microscopy for Lithium dendrite imaging and analysis, and integrating first-principle theory calculations for deeper insights. These endeavors collectively contribute to advancing our understanding of

lithium metal batteries and refining the design principles for more efficient and safer energy storage systems.

(1) Expanding the measurement parameters within the pouch cells is a key element of future work. This involves investigating the influence of varying temperatures, electrolyte compositions suitable for pouch cell designs, and other specific factors relevant to the pouch cell environment. The objective is to comprehensively understand how the current collector performs under conditions unique to pouch cells, thereby guiding the optimization of these batteries for real-world applications.

(2) One promising avenue for further exploration involves the utilization of optical microscopy to capture and study lithium dendrite formation. By employing advanced imaging techniques, aiming to gain a detailed understanding of the morphological evolution and behavior of lithium dendrites on the current collector surface. This macroscopic analysis will provide valuable insights into the factors influencing dendrite growth, shedding light on potential strategies for dendrite suppression and improved battery safety.

(3) Additionally, incorporating first-principle theory calculations into the investigation will allow for a more in-depth exploration of the underlying mechanisms governing the electrochemical processes at play. This theoretical framework can aid in predicting and understanding the complex interplay of factors affecting the performance of the current collector under varying conditions, contributing to the development of more accurate models and design strategies.

# REFERENCE

[1] Dunn B, Kamath H, Tarascon J M. Electrical energy storage for the grid: A battery of choices. Science. 2011;334(6058):928-935.

[2] Chu S, Majumdar A. Opportunities and challenges for a sustainable energy future. Nature. 2012;488(7411):294-303.

[3] Armand M, Tarascon J M. Building better batteries. Nature. 2008;451: 652–657.

[4] Liang Y, Zhao C Z, Yuan H, Chen Y, Zhang W, Huang J Q, et al. A review of rechargeable batteries for portable electronic devices. InfoMat. 2019;1(1):6-32.

[5] Goodenough J B. Energy storage materials: A perspective. Energy Storage Materials. 2015;1:158-161.

[6] Goodenough J B, Kim Y. Challenges for rechargeable Li batteries. Chemistry of Materials. 2009;22(3):587-603.

[7] Liu Y, Yang Y. Recent progress of $TiO_2$-based anodes for Li ion batteries. Journal of Nanomaterials. 2016;2016:1-15.

[8] Ye H, Xin S, Yin Y X, Li J Y, Guo Y G, Wan L J. Stable Li plating/stripping electrochemistry realized by a hybrid Li reservoir in spherical carbon granules with 3D conducting skeletons. J Am Chem Soc. 2017;139(16):5916-5922.

[9] Palacin M R, de Guibert A. Why do batteries fail?. Science. 2016;351(6273):1253292.

[10] Choudhury S, Wan C T C, Sadat W A, Tu Z, Lau S, Zachman M J, et al. Designer interphases for the lithium-oxygen electrochemical cell. Science Advances. 2017;3:e1602809.

[11] He P, Zhang T, Jiang J, Zhou H. Lithium-air batteries with hybrid electrolytes. J Phys Chem Lett. 2016;7(7):1267-1280.

[12] Whittingham M S. Lithium batteries and cathode materials. Chemical Reviews. 2004;104:4271-4301.

[13] Liu K, Pei A, Lee H R, Kong B, Liu N, Lin D, et al. Lithium metal anodes with an adaptive "solid-liquid" interfacial protective layer. J Am Chem Soc. 2017;139(13):4815-4820.

[14] Freunberger S A, Chen Y, Drewett N E, Hardwick L J, Barde F, Bruce P G. The lithium-oxygen battery with ether-based electrolytes. Angew Chem Int Ed. 2011;50(37):8609-8613.

[15] Grande L, Paillard E, Hassoun J, Park J B, Lee Y J, Sun Y K, et al. The lithium/air battery: still an emerging system or a practical reality?. Advanced Materials. 2015;27(5):784-800.

[16] Liu B, Zhang J-G, Xu W. Advancing lithium metal batteries. Joule. 2018;2(5):833-845.

[17] Zhu Y, He X, Mo Y. Strategies based on nitride materials chemistry to stabilize Li metal anode. Advanced Science. 2017;4(8):1600517.

[18] Sun Y, Zheng G, Seh Zhi W, Liu N, Wang S, Sun J, et al. Graphite-encapsulated Li-metal hybrid anodes for high-capacity Li batteries. Chem. 2016;1(2):287-297.

[19] Dong Y, Lu P, Shi H, Qin J, Chen J, Ren W, et al. 2D hierarchical yolk-shell heterostructures as advanced host-interlayer integrated electrode for enhanced Li-S batteries. Journal of Energy Chemistry. 2019;36:64-73.

[20] Guo Y, Li H, Zhai T. Reviving lithium-metal anodes for next-generation high-energy batteries. Advanced Materials. 2017;29(29):1700007.

[21] Wang D, Zhang W, Zheng W, Cui X, Rojo T, Zhang Q. Towards high-safe Lithium metal anodes: suppressing lithium dendrites via tuning surface energy. Advanced Science. 2017;4(1):1600168.

[22] Cheng X B, Zhang R, Zhao C Z, Wei F, Zhang J G, Zhang Q. A Review of solid electrolyte interphases on lithium metal anode. Advanced Science. 2016;3(3):1500213.

[23] Zhang R, Li N W, Cheng X B, Yin Y X, Zhang Q, Guo Y G. Advanced micro/nanostructures for lithium metal anodes. Advanced Science. 2017;4(3):1600445.

[24] Rao B M L, Fancis R W, Christopher H A. Lithium-aluminum electrode. Journal of The Electrochemical Society. 1977;124(10):1490-1492.

[25] Murphy D W, Di Salvo F J, Carides J N, Waszczak J V. Topochemical reactions of rutile related structures with lithium. 1978;13:1395-1402.

[26] Xu K. Electrolytes and interphases in Li-ion batteries and beyond. Chemical Reviews. 2014;114(23):11503-11618.

[27] Lazzari M, Scrosati B. A cyclable Lithium organic electrolyte cell based on two intercalation electrodes. Journal of The Electrochemical Society. 2019;127(3):773-774.

[28] Peled E. The Electrochemical behavior of alkali and alkaline earth metals in nonaqueous battery systems—The solid electrolyte interphase model. Journal of The Electrochemical Society. 1979;126(12):2047-2051.

[29] Zhang X Q, Chen X, Xu R, Cheng X B, Peng H J, Zhang R, et al. Columnar lithium metal anodes. Angew Chem Int Ed. 2017;56(45):14207-14211.

[30] Cheng X B, Zhao M Q, Chen C, Pentecost A, Maleski K, Mathis T, et al. Nanodiamonds suppress the growth of lithium dendrites. Nature Communication. 2017;8(1):336.

[31] Lang J, Qi L, Luo Y, Wu H. High performance lithium metal anode: Progress and prospects. Energy Storage Materials. 2017;7:115-129.

[32] Hou T Z, Chen X, Peng H J, Huang J Q, Li B Q, Zhang Q, et al. Design principles for heteroatom-doped nanocarbon to achieve strong anchoring of polysulfides for lithium-sulfur batteries. Small. 2016;12(24):3283-3291.

[33] Hou T Z, Xu W T, Chen X, Peng H J, Huang J Q, Zhang Q. Lithium bond chemistry in lithium-sulfur batteries. Angew Chem Int Ed. 2017;56(28):8178-8182.

[34] Kong L, Peng H-J, Huang J-Q, Zhu W, Zhang G, Zhang Z-W, et al. Beaver-dam-like membrane: A robust and sulphifilic $MgBO_2(OH)$/CNT/PP nest separator in Li-S batteries. Energy Storage Materials. 2017;8:153-160.

[35] Peng H J, Wang D W, Huang J Q, Cheng X B, Yuan Z, Wei F, et al. Janus separator of polypropylene-supported cellular graphene framework for sulfur cathodes with high utilization in lithium-sulfur batteries. Advanced Science. 2016;3(1):1500268.

[36] Liang J, Sun Z-H, Li F, Cheng H-M. Carbon materials for Li–S batteries: Functional evolution and performance improvement. Energy Storage Materials. 2016;2:76-106.

[37] Mi K, Jiang Y, Feng J, Qian Y, Xiong S. Hierarchical carbon nanotubes with a thick microporous wall and inner channel as efficient scaffolds for lithium–sulfur batteries. Advanced Functional Materials. 2016;26(10):1571-1579.

[38] Peng H J, Zhang Z W, Huang J Q, Zhang G, Xie J, Xu W T, et al. A cooperative interface for highly efficient lithium-sulfur batteries. Advanced Materials. 2016;28(43):9551-9558.

[39] Zhai P-Y, Peng H-J, Cheng X-B, Zhu L, Huang J-Q, Zhu W, et al. Scaled-up fabrication of porous-graphene-modified separators for high-capacity lithium–sulfur batteries. Energy Storage Materials. 2017;7:56-63.

[40] Stark J K, Ding Y, Kohl P A. Nucleation of electrodeposited lithium metal: Dendritic growth and the effect of Co-deposited sodium. Journal of The Electrochemical Society. 2013;160(9):D337-D342.

[41] Liu X H, Zhong L, Zhang L Q, Kushima A, Mao S X, Li J, et al. Lithium fiber growth on the anode in a nanowire lithium ion battery during charging. Applied Physics Letters. 2011;98(18): 183107.

[42] Porthault H, Decaux C. Electrodeposition of lithium metal thin films and its application in all-solid-state microbatteries. Electrochimica Acta. 2016;194:330-337.

[43] Steiger J, Kramer D, Mönig R. Mechanisms of dendritic growth investigated by in situ light microscopy during electrodeposition and dissolution of lithium. Journal of Power Sources. 2014;261:112-119.

[44] Sano H, Kitta M, Matsumoto H. Effect of charge transfer resistance on morphology of lithium electrodeposited in ionic liquid. Journal of The Electrochemical Society. 2016;163(12):D3076-D3079.

[45] Tang C-Y, Dillon S J. In Situ scanning electron microscopy characterization of the mechanism for Li dendrite growth. Journal of The Electrochemical Society. 2016;163(8):A1660-A1665.

[46] Steiger J, Kramer D, Mönig R. Microscopic observations of the formation, growth and shrinkage of lithium moss during electrodeposition and dissolution. Electrochimica Acta. 2014;136(529-536.

[47] Sun F, Zhou D, He X, Osenberg M, Dong K, Chen L, et al. Morphological reversibility of modified Li-based anodes for next-generation batteries. ACS Energy Letters. 2019;5(1):152-161.

[48] Aryanfar A, Brooks D J, Colussi A J, Hoffmann M R. Quantifying the dependence of dead lithium losses on the cycling period in lithium metal batteries. Phys Chem Chem Phys. 2014;16(45):24965-24970.

[49] Park M S, Ma S B, Lee D J, Im D, Doo S G, Yamamoto O. A highly reversible lithium metal anode. Scientific Reports. 2014;4:3815.

[50] Brissot C, Rosso M, Chazalviel J.N, Baudry P, Lascaud S. In situ study of dendritic growth in lithium/PEO-salt/lithium cells. 1998;43(10-11):1569-1574.

[51] Bai P, Li J, Brushett F R, Bazant M Z. Transition of lithium growth mechanisms in liquid electrolytes. Energy & Environmental Science. 2016;9(10):3221-3229.

[52] Orsini F, Pasquier A, Beaudouin B, Tarascon J.M, Trentin M, Langenhuizen N, Beer E, Notten P. In situ SEM study of the interfaces in plastic lithium cells. Journal of Power Sources. 1999;81-82:918-921.

[53] Becking J, Gröbmeyer A, Kolek M, Rodehorst U, Schulze S, Winter M, et al. Lithium-metal foil surface modification: An effective method to improve the cycling performance of lithium-metal batteries. Advanced Materials Interfaces. 2017;4(16).

[54] Cheng X-B, Yan C, Huang J-Q, Li P, Zhu L, Zhao L, et al. The gap between long lifespan Li-S coin and pouch cells: The importance of lithium metal anode protection. Energy Storage Materials. 2017;6:18-25.

[55] Cheng X B, Zhang R, Zhao C Z, Zhang Q. Toward safe lithium metal anode in rechargeable batteries: A review. Chemical Reviews. 2017;117(15):10403-10473.

[56] Dornbusch D A, Hilton R, Lohman S D, Suppes G J. Experimental validation of the elimination of dendrite short-circuit failure in secondary lithium-metal convection cell batteries. Journal of The Electrochemical Society. 2014;162(3):A262-A268.

[57] Liu K, Zhuo D, Lee H.W, Liu W, Lin D, Lu Y, et al. Extending the life of lithium-based rechargeable batteries by reaction of lithium dendrites with a novel silica nanoparticle sandwiched separator. Advanced Materials. 2017;29(4):1603987.

[58] Park J, Jeong J, Lee Y, Oh M, Ryou M H, Lee Y M. Micro-patterned lithium metal anodes with suppressed dendrite formation for post lithium-ion batteries. Advanced Materials Interfaces. 2016;3(11):1600140.

[59] Liu S, Li G R, Gao X P. Lanthanum nitrate as electrolyte additive to stabilize the surface morphology of lithium anode for lithium-sulfur battery. ACS Appl Mater Interfaces. 2016;8(12):7783-7789.

[60] Tao R, Bi X, Li S, Yao Y, Wu F, Wang Q, et al. Kinetics tuning the electrochemistry of lithium dendrites formation in lithium batteries through electrolytes. ACS Appl Mater Interfaces. 2017;9(8):7003-7008.

[61] Leung K, Soto F, Hankins K, Balbuena P B, Harrison K L. Stability of solid electrolyte interphase components on lithium metal and reactive anode material surfaces. The Journal of Physical Chemistry C. 2016;120(12):6302-6313.

[62] Fan L, Zhuang H L, Gao L, Lu Y, Archer L A. Regulating Li deposition at artificial solid electrolyte interphases. Journal of Materials Chemistry A. 2017;5(7):3483-3492.

[63] Liu Z, Qi Y, Lin Y X, Chen L, Lu P, Chen L Q. Interfacial study on solid electrolyte interphase at Li metal anode: Implication for Li dendrite growth. Journal of The Electrochemical Society. 2016;163(3):A592-A598.

[64] Liu W, Li W, Zhuo D, Zheng G, Lu Z, Liu K, et al. Core-shell nanoparticle coating as an interfacial layer for dendrite-free lithium metal anodes. ACS Central Science. 2017;3(2):135-140.

[65] Wood K N, Kazyak E, Chadwick A F, Chen K H, Zhang J G, Thornton K, et al. Dendrites and pits: Untangling the complex behavior of lithium metal anodes through operando video microscopy. ACS Central Science. 2016;2(11):790-801.

[66] López C M, Vaughey J T, Dees D W. Morphological transitions on lithium metal anodes. 2009:156(9):A726-A729.

[67] Lv D, Shao Y, Lozano T, Bennett W D, Graff G L, Polzin B, et al. Failure mechanism for fast-charged lithium metal batteries with liquid electrolytes. Advanced Energy Materials. 2014;5(3):1400993.

[68] Bucur C B, Lita A, Osada N, Muldoon J. A soft, multilayered lithium–electrolyte interface. Energy & Environmental Science. 2016;9(1):112-116.

[69] Liu K, Bai P, Bazant M Z, Wang C-A, Li J. A soft non-porous separator and its effectiveness in stabilizing Li metal anodes cycling at 10 mA $cm^{-2}$ observed in situ in a capillary cell. Journal of Materials Chemistry A. 2017;5(9):4300-4307.

[70] Peng Z, Wang S, Zhou J, Jin Y, Liu Y, Qin Y, et al. Volumetric variation confinement: surface protective structure for high cyclic stability of lithium metal electrodes. Journal of Materials Chemistry A. 2016;4(7):2427-2432.

[71] Liu Y, Lin D, Liang Z, Zhao J, Yan K, Cui Y. Lithium-coated polymeric matrix as a minimum volume-change and dendrite-free lithium metal anode. Nature Communications. 2016;7:10992.

[72] Gregory T D, Hoffman R J, Winterton, R C. Nonaqueous electrochemistry of magnesium: Applications to energy storage. Journal of The Electrochemical Society. 1990;137(3):775-780.

[73] Guo Y, Yang J, NuLi Y, Wang J. Study of electronic effect of Grignard reagents on their electrochemical behavior. Electrochemistry Communications. 2010;12(12):1671-1673.

[74] Matsui M. Study on electrochemically deposited Mg metal. Journal of Power Sources. 2011;196(16):7048-7055.

[75] Ling C, Banerjee D, Matsui M. Study of the electrochemical deposition of Mg in the atomic level: Why it prefers the non-dendritic morphology. Electrochimica Acta. 2012;76:270-274.

[76] Zhao Q, Stalin S, Archer L A. Stabilizing metal battery anodes through the design of solid electrolyte interphases. Joule. 2021;5(5):1119-1142.

[77] Jackle M, Gross A. Microscopic properties of lithium, sodium, and magnesium battery anode materials related to possible dendrite growth. J Chem Phys. 2014;141(17):174710.

[78] Yamaki J I, Tobishima S I, Hayashi K, Saito K, Nemoto Y, Arakawa M A consideration of the morphology of electrochemically deposited lithium in an organic electrolyte. Journal of Power Sources. 1998;74:219-227.

[79] Jeong J H, Goldenfeld N, Dantzig J A. Phase field model for three-dimensional dendritic growth with fluid flow. Phys Rev E Stat Nonlin Soft Matter Phys. 2001;64(4 Pt 1):041602.

[80] Ely D R, García R E. Heterogeneous nucleation and growth of Lithium electrodeposits on negative electrodes. Journal of The Electrochemical Society. 2013;160(4):A662-A668.

[81] Okajima Y, Shibuta Y, Suzuki T. A phase-field model for electrode reactions with Butler–Volmer kinetics. Computational Materials Science. 2010;50(1):118-124.

[82] Yan K, Lu Z, Lee H-W, Xiong F, Hsu P-C, Li Y, et al. Selective deposition and stable encapsulation of lithium through heterogeneous seeded growth. Nature Energy. 2016;1(3):16010.

[83] Wang S H, Yue J, Dong W, Zuo T T, Li J Y, Liu X, et al. Tuning wettability of molten lithium via a chemical strategy for lithium metal anodes. Nature Communications. 2019;10(1):4930.

[84] Liu D H, Bai Z, Li M, Yu A, Luo D, Liu W, et al. Developing high safety Li-metal anodes for future high-energy Li-metal batteries: strategies and perspectives. Chemical Society Reviews. 2020;49(15):5407-5445.

[85] Chazalviel J. Electrochemical aspects of the generation of ramified metallic electrodeposits. Phys Rev A. 1990;42(12):7355-7367.

[86] Fleury V, Chazalviel J N, Rosso M, Sapoval B. The role of the anions in the growth speed of fractal electrodeposits. 1990;290:249-255.

[87] Soto F A, Ma Y, Martinez de la Hoz J M, Seminario J M, Balbuena P B. Formation and growth mechanisms of solid-electrolyte interphase layers in rechargeable batteries. Chemistry of Materials. 2015;27(23):7990-8000.

[88] Pinson M B, Bazant M Z. Theory of SEI formation in rechargeable batteries: Capacity fade, accelerated aging and lifetime prediction. Journal of The Electrochemical Society. 2013;160(2):A243-A250.

[89] Wenzel S, Leichtweiss T, Krüger D, Sann J, Janek J. Interphase formation on lithium solid electrolytes—An in situ approach to study interfacial reactions by photoelectron spectroscopy. Solid State Ionics. 2015;278:98-105.

[90] Zhu B, Jin Y, Hu X, Zheng Q, Zhang S, Wang Q, et al. Poly(dimethylsiloxane) thin film as a stable interfacial layer for high-performance lithium-metal battery anodes. Advanced Materials. 2017;29(2):1603755.

[91] Zahn R, Lagadec M F, Hess M, Wood V. Improving ionic conductivity and lithium-ion transference number in lithium-ion battery separators. ACS Appl Mater Interfaces. 2016;8(48):32637-32642.

[92] Liu Y, Lin D, Yuen P Y, Liu K, Xie J, Dauskardt R H, et al. An artificial solid electrolyte interphase with high Li-ion conductivity, mechanical strength, and flexibility for stable lithium metal anodes. Advanced Materials. 2017;29(10):1605531.

[93] Lin D, Liu W, Liu Y, Lee H R, Hsu P C, Liu K, et al. High ionic conductivity of composite solid polymer electrolyte via in situ synthesis of monodispersed $SiO_2$ nanospheres in poly(ethylene oxide). Nano Lett. 2016;16(1):459-465.

[94] Kushima A, So K P, Su C, Bai P, Kuriyama N, Maebashi T, et al. Liquid cell transmission electron microscopy observation of lithium metal growth and dissolution: Root growth, dead lithium and lithium flotsams. Nano Energy. 2017;32:271-279.

[95] Gauthier M, Carney T J, Grimaud A, Giordano L, Pour N, Chang H H, et al. Electrode-electrolyte interface in Li-ion batteries: current understanding and new insights. J Phys Chem Lett. 2015;6(22):4653-4672.

[96] Zhou W, Wang S, Li Y, Xin S, Manthiram A, Goodenough J B. Plating a dendrite-free lithium anode with a polymer/ceramic/polymer sandwich electrolyte. J Am Chem Soc. 2016;138(30):9385-9388.

[97] Rosso M, Brissot C, Teyssot A, Dollé M, Sannier L, Tarascon J-M, et al. Dendrite short-circuit and fuse effect on Li/polymer/Li cells. Electrochimica Acta. 2006;51(25):5334-5340.

[98] Rosso M, Gobron T, Brissot C, Chazalviel J N, Lascaud S. Onset of dendritic growth in lithium/polymer cells. Journal of Power Sources. 2001;97-98:804-806.

[99] Chen X, Hou T-Z, Li B, Yan C, Zhu L, Guan C, et al. Towards stable lithium-sulfur batteries: Mechanistic insights into electrolyte decomposition on lithium metal anode. Energy Storage Materials. 2017;8:194-201.

[100] Xu K. Nonaqueous liquid electrolytes for lithium-based rechargeable batteries. Chemical Reviews. 2004;104:4303-4417.

[101] Heine J, Hilbig P, Qi X, Niehoff P, Winter M, Bieker P. Fluoroethylene carbonate as electrolyte additive in tetraethylene glycol dimethyl ether based electrolytes for application in lithium ion and lithium metal batteries. Journal of The Electrochemical Society. 2015;162(6):A1094-A1101.

[102] Guo J, Wen Z, Wu M, Jin J, Liu Y. Vinylene carbonate–$LiNO_3$: A hybrid additive in carbonic ester electrolytes for SEI modification on Li metal anode. Electrochemistry Communications. 2015;51:59-63.

[103] Sano H, Sakaebe H, Matsumoto H. Observation of electrodeposited lithium by optical microscope in room temperature ionic liquid-based electrolyte. Journal of Power Sources. 2011;196(16):6663-6669.

[104] Jung R, Metzger M, Haering D, Solchenbach S, Marino C, Tsiouvaras N, et al. Consumption of fluoroethylene carbonate (FEC) on Si-C composite electrodes for Li-Ion batteries. Journal of The Electrochemical Society. 2016;163(8):A1705-A1716.

[105] McMillan R, Slegr H, Shu Z, Wang W. Fluoroethylene carbonate electrolyte and its use in lithium ion batteries with graphite anodes. 1999;81-82:20-26.

[106] Rezqita A, Sauer M, Foelske A, Kronberger H, Trifonova A. The effect of electrolyte additives on electrochemical performance of silicon/mesoporous carbon (Si/MC) for anode materials for lithium-ion batteries. Electrochimica Acta. 2017;247:600-609.

[107] Leggesse E G, Jiang J C. Theoretical study of the reductive decomposition of ethylene sulfite: a film-forming electrolyte additive in lithium ion batteries. J Phys Chem A. 2012;116(45):11025-11033.

[108] Li C, Gu L, Maier J. Enhancement of the Li conductivity in LiF by introducing glass/crystal interfaces. Advanced Functional Materials. 2012;22(6):1145-1149.

[109] Sun H-H, Dolocan A, Weeks J A, Rodriguez R, Heller A, Mullins C B. In situ formation of a multicomponent inorganic-rich SEI layer provides a fast charging and high specific energy Li-metal battery. Journal of Materials Chemistry A. 2019;7(30):17782-17789.

[110] Zhang X Q, Cheng X B, Chen X, Yan C, Zhang Q. Fluoroethylene carbonate additives to render uniform Li deposits in lithium metal batteries. Advanced Functional Materials. 2017;27(10):1605989.

[111] Adams B D, Carino E V, Connell J G, Han K S, Cao R, Chen J, et al. Long term stability of Li-S batteries using high concentration lithium nitrate electrolytes. Nano Energy. 2017;40:607-617.

[112] Zhang S S. Role of $LiNO_3$ in rechargeable lithium/sulfur battery. Electrochimica Acta. 2012;70:344-348.

[113] Zhang S S. A new finding on the role of $LiNO_3$ in lithium-sulfur battery. Journal of Power Sources. 2016;322:99-105.

[114] Shi Q, Zhong Y, Wu M, Wang H, Wang H. High-capacity rechargeable batteries based on deeply cyclable lithium metal anodes. Proceedings of the National Academy of Sciences. 2018;115(22):5676-5680.

[115] Yan C, Yao Y X, Chen X, Cheng X B, Zhang X Q, Huang J Q, et al. Lithium nitrate solvation chemistry in carbonate electrolyte sustains high-voltage lithium metal batteries. Angew Chem Int Ed. 2018;57(43):14055-14059.

[116] Zhang X Q, Chen X, Cheng X B, Li B Q, Shen X, Yan C, et al. Highly stable lithium metal batteries enabled by regulating the solvation of lithium ions in nonaqueous electrolytes. Angew Chem Int Ed. 2018;57(19):5301-5305.

[117] Ren X, Zhang Y, Engelhard M H, Li Q, Zhang J-G, Xu W. Guided lithium metal deposition and improved lithium coulombic efficiency through synergistic effects of $LiAsF_6$ and cyclic carbonate additives. ACS Energy Letters. 2017;3(1):14-19.

[118] Xiang H, Shi P, Bhattacharya P, Chen X, Mei D, Bowden M E, et al. Enhanced charging capability of lithium metal batteries based on lithium bis(trifluoromethanesulfonyl)imide-lithium bis(oxalato)borate dual-salt electrolytes. Journal of Power Sources. 2016;318:170-177.

[119] Li S, Zhao D, Wang P, Cui X, Tang F. Electrochemical effect and mechanism of adiponitrile additive for high-voltage electrolyte. Electrochimica Acta. 2016;222:668-677.

[120] Yan C, Cheng X-B, Zhao C-Z, Huang J-Q, Yang S-T, Zhang Q. Lithium metal protection through in-situ formed solid electrolyte interphase in lithium-sulfur batteries: The role of polysulfides on lithium anode. Journal of Power Sources. 2016;327:212-220.

[121] Huang Z, Ren J, Zhang W, Xie M, Li Y, Sun D, et al. Protecting the Li-Metal anode in a Li-$O_2$ battery by using boric acid as an SEI-Forming additive. Advanced Materials. 2018;30(39):e1803270.

[122] Ding F, Xu W, Graff G L, Zhang J, Sushko M L, Chen X, et al. Dendrite-free lithium deposition via self-healing electrostatic shield mechanism. J Am Chem Soc. 2013;135(11):4450-4456.

[123] Zhang Y, Qian J, Xu W, Russell S M, Chen X, Nasybulin E, et al. Dendrite-free lithium deposition with self-aligned nanorod structure. Nano Lett. 2014;14(12):6889-6896.

[124] Xiao L, Chen X, Cao R, Qian J, Xiang H, Zheng J, et al. Enhanced performance of Li|$LiFePO_4$ cells using $CsPF_6$ as an electrolyte additive. Journal of Power Sources. 2015;293:1062-1067.

[125] Ye H, Yin Y-X, Zhang S-F, Shi Y, Liu L, Zeng X-X, et al. Synergism of Al-containing solid electrolyte interphase layer and Al-based colloidal particles for stable lithium anode. Nano Energy. 2017;36:411-417.

[126] Chen Y, Luo Y, Zhang H, Qu C, Zhang H, Li X. The challenge of lithium metal anodes for practical applications. Small Methods. 2019;3(7):1800551.

[127] Liu Q C, Xu J J, Yuan S, Chang Z W, Xu D, Yin Y B, et al. Artificial protection film on Lithium metal anode toward long-cycle-life lithium-oxygen batteries. Advance Materials. 2015;27(35):5241-5247.

[128] Kozen A C, Lin C-F, Zhao O, Lee S B, Rubloff G W, Noked M. Stabilization of lithium metal anodes by hybrid artificial solid electrolyte interphase. Chemistry of Materials. 2017;29(15):6298-6307.

[129] Zhang X Q, Cheng X B, Zhang Q. Advances in interfaces between Li metal anode and electrolyte. Advanced Materials Interfaces. 2017;5(2):1701097.

[130] Xu R, Cheng X-B, Yan C, Zhang X-Q, Xiao Y, Zhao C-Z, et al. Artificial interphases for highly stable lithium metal anode. Matter. 2019;1(2):317-344.

[131] Shi L, Xu A, Zhao T. First-principles investigations of the working mechanism of 2D h-BN as an interfacial layer for the anode of lithium metal batteries. ACS Appl Mater Interfaces. 2017;9(2):1987-1994.

[132] Zhao J, Liao L, Shi F, Lei T, Chen G, Pei A, et al. Surface fluorination of reactive battery anode materials for enhanced stability. J Am Chem Soc. 2017;139(33):11550-11558.

[133] Yan C, Cheng X B, Yao Y X, Shen X, Li B Q, Li W J, et al. An armored mixed conductor interphase on a dendrite-free lithium-metal anode. Advanced Materials. 2018;30(45):e1804461.

[134] Wang L, Fu S, Zhao T, Qian J, Chen N, Li L, et al. In situ formation of a LiF and Li–Al alloy anode protected layer on a Li metal anode with enhanced cycle life. Journal of Materials Chemistry A. 2020;8(3):1247-1253.

[135] Peng Z, Zhao N, Zhang Z, Wan H, Lin H, Liu M, et al. Stabilizing Li/electrolyte interface with a transplantable protective layer based on nanoscale LiF domains. Nano Energy. 2017;39:662-672.

[136] Zhang Y, Wang G, Tang L, Wu J, Guo B, Zhu M, et al. Stable lithium metal anodes enabled by inorganic/organic double-layered alloy and polymer coating. Journal of Materials Chemistry A. 2019;7(44):25369-25376.

[137] Wang G, Xiong X, Xie D, Fu X, Lin Z, Yang C, et al. A scalable approach for dendrite-free alkali metal anodes via room-temperature facile surface fluorination. ACS Appl Mater Interfaces. 2019;11(5):4962-4968.

[138] Liang X, Pang Q, Kochetkov I R, Sempere M S, Huang H, Sun X, et al. A facile surface chemistry route to a stabilized lithium metal anode. Nature Energy. 2017;2(9):17119.

[139] Ren Y, Qi Z, Zhang C, Yang S, Ma X, Liu X, et al. The charge transfer of intercalated Li atoms around islands on Li-halide (F, Br, Cl) surface of SEIs: A first principles calculation. Computational Materials Science. 2020;176:109535.

[140] Li G, Huang Q, He X, Gao Y, Wang D, Kim S H, et al. Self-formed hybrid interphase layer on lithium metal for high-performance lithium-sulfur batteries. ACS Nano. 2018;12(2):1500-1507.

[141] Li W, Yao H, Yan K, Zheng G, Liang Z, Chiang Y M, et al. The synergetic effect of lithium polysulfide and lithium nitrate to prevent lithium dendrite growth. Nature Communications. 2015;6:7436.

[142] Chen H, Pei A, Lin D, Xie J, Yang A, Xu J, et al. Uniform high ionic conducting lithium sulfide protection layer for stable lithium metal anode. Advanced Energy Materials. 2019;9(22):1900858.

[143] Liu F, Wang L, Zhang Z, Shi P, Feng Y, Yao Y, et al. A mixed lithium-ion conductive $Li_2S/Li_2Se$ protection layer for stable lithium metal anode. Advanced Functional Materials. 2020;30(23):2001607.

[144] Liao K, Wu S, Mu X, Lu Q, Han M, He P, et al. Developing a "water-defendable" and "Dendrite-Free" lithium-metal anode using a simple and promising $GeCl_4$ pretreatment method. Advanced Materials. 2018;30(36):1705711.

[145] Jing H-K, Kong L-L, Liu S, Li G-R, Gao X-P. Protected lithium anode with porous $Al_2O_3$ layer for lithium–sulfur battery. Journal of Materials Chemistry A. 2015;3(23):12213-12219.

[146] Ren F, Li Z, Zhu Y, Huguet P, Deabate S, Wang D, et al. Artificial nucleation sites with stable SEI for Li metal anodes by aggressive Al pulverization. Nano Energy. 2020;73:104746.

[147] Li N W, Yin Y X, Yang C P, Guo Y G. An artificial solid electrolyte interphase layer for stable lithium metal anodes. Advanced Materials. 2016;28(9):1853-1858.

[148] Tang W, Yin X, Kang S, Chen Z, Tian B, Teo S L, et al. Lithium silicide surface enrichment: A solution to lithium metal battery. Advanced Materials. 2018;30(34):1801745.

[149] Chu F, Hu J, Tian J, Zhou X, Li Z, Li C. In-Situ plating of porous Mg network layer to reinforce anode dendrite suppression in Li-metal batteries. ACS Applied Mterials Interfaces. 2018;10(15):12678-12689.

[150] Liu Y, Xiong S, Wang J, Jiao X, Li S, Zhang C, et al. Dendrite-free lithium metal anode enabled by separator engineering via uniform loading of lithiophilic nucleation sites. Energy Storage Materials. 2019;19:24-30.

[151] Liu T, Hu J, Li C, Wang Y. Unusual conformal Li plating on alloyable nanofiber frameworks to enable dendrite suppression of Li metal anode. ACS Applied Energy Materials. 2019;2(6):4379-4388.

[152] Li N W, Shi Y, Yin Y X, Zeng X X, Li J Y, Li C J, et al. A flexible solid electrolyte interphase layer for long-life lithium metal anodes. Angew Chem Int Ed. 2018;57(6):1505-1509.

[153] Xu R, Zhang X Q, Cheng X B, Peng H J, Zhao C Z, Yan C, et al. Artificial soft–rigid protective layer for dendrite-free lithium metal anode. Advanced Functional Materials. 2018;28(8):1705838.

[154] Luo J, Fang C C, Wu N L. High polarity poly(vinylidene difluoride) thin coating for dendrite-free and high-performance lithium metal anodes. Advanced Energy Materials. 2017;8(2):1701482.

[155] Wang G, Chen C, Chen Y, Kang X, Yang C, Wang F, et al. Self-stabilized and strongly adhesive supramolecular polymer protective layer enables ultrahigh-rate and large-capacity lithium-metal anode. Angew Chem Int Ed. 2020;59(5):2055-2060.

[156] Liu Y, Liu Q, Xin L, Liu Y, Yang F, Stach E A, et al. Making Li-metal electrodes rechargeable by controlling the dendrite growth direction. Nature Energy. 2017;2(7):17083.

[157] Monroe C, Newman J. Dendrite growth in lithium/polymer systems. Journal of The Electrochemical Society. 2003;150(10):A1377-A1384.

[158] Li C, Liu S, Shi C, Liang G, Lu Z, Fu R, et al. Two-dimensional molecular brush-functionalized porous bilayer composite separators toward ultrastable high-current density lithium metal anodes. Nature Communications. 2019;10(1):1363.

[159] Luo W, Zhou L, Fu K, Yang Z, Wan J, Manno M, et al. A thermally conductive separator for stable Li metal anodes. Nano Lett. 2015;15(9):6149-6154.

[160] He Y, Chang Z, Wu S, Qiao Y, Bai S, Jiang K, et al. Simultaneously inhibiting lithium dendrites growth and polysulfides shuttle by a flexible MOF-based membrane in Li–S batteries. Advanced Energy Materials. 2018;8(34):1802130.

[161] Wu H, Huang Y, Xu S, Zhang W, Wang K, Zong M. Fabricating three-dimensional hierarchical porous N-doped graphene by a tunable assembly method for interlayer assisted lithium-sulfur batteries. Chemical Engineering Journal. 2017;327:855-867.

[162] Hu M, Ma Q, Yuan Y, Pan Y, Chen M, Zhang Y, et al. Grafting polyethyleneimine on electrospun nanofiber separator to stabilize lithium metal anode for lithium sulfur batteries. Chemical Engineering Journal. 2020;388:124258

[163] Lee H, Oh P, Kim J, Cha H, Chae S, Lee S, et al. Advances and prospects of sulfide All-Solid-State lithium batteries via One-to-One comparison with conventional liquid lithium ion batteries. Advanced Materials. 2019;31(29):1900376.

[164] Han F, Westover A S, Yue J, Fan X, Wang F, Chi M, et al. High electronic conductivity as the origin of lithium dendrite formation within solid electrolytes. Nature Energy. 2019;4(3):187-196.

[165] Duan H, Yin Y X, Shi Y, Wang P F, Zhang X D, Yang C P, et al. Dendrite-Free Li-metal battery enabled by a thin asymmetric solid electrolyte with engineered layers. J Am Chem Soc. 2018;140(1):82-85.

[166] Duan J, Wu W, Nolan A M, Wang T, Wen J, Hu C, et al. Lithium-Graphite paste: An interface compatible anode for Solid-State Batteries. Advanced Materials. 2019;31(10):1807243.

[167] Zhao C Z, Zhang X Q, Cheng X B, Zhang R, Xu R, Chen P Y, et al. An anion-immobilized composite electrolyte for dendrite-free lithium metal anodes. Proceedings of the National Academy of Sciences. 2017;114(42):11069-11074.

[168] Rupp R, Caerts B, Vantomme A, Fransaer J, Vlad A. Lithium diffusion in copper. J Phys Chem Lett. 2019;10(17):5206-5210.

[169] Stan M C, Becking J, Kolesnikov A, Wankmiller B, Frerichs J E, Hansen M R, et al. Sputter coating of lithium metal electrodes with lithiophilic metals for homogeneous and reversible lithium electrodeposition and electrodissolution. Materials Today. 2020;39:137-145.

[170] Liu S, Zhang X, Li R, Gao L, Luo J. Dendrite-free Li metal anode by lowering deposition interface energy with $Cu_{99}Zn$ alloy coating. Energy Storage Materials. 2018;14:143-148.

[171] Guo F, Wu C, Chen H, Zhong F, Ai X, Yang H, et al. Dendrite-free lithium deposition by coating a lithiophilic heterogeneous metal layer on lithium metal anode. Energy Storage Materials. 2020;24:635-643.

[172] Hou Z, Yu Y, Wang W, Zhao X, Di Q, Chen Q, et al. Lithiophilic Ag Nanoparticle Layer on Cu Current Collector toward Stable Li Metal Anode. ACS Appl Mater Interfaces. 2019;11(8):8148-8154.

[173] Zhang S S, Fan X, Wang C. A tin-plated copper substrate for efficient cycling of lithium metal in an anode-free rechargeable lithium battery. Electrochimica Acta. 2017;258:1201-1207.

[174] Oyakhire S T, Huang W, Wang H, Boyle D T, Schneider J R, de Paula C, et al. Revealing and elucidating ALD-Derived control of lithium plating microstructure. Advanced Energy Materials. 2020;10(44):2002736.

[175] Chen W, Salvatierra R V, Ren M, Chen J, Stanford M G, Tour J M. Laser-Induced silicon oxide for anode-free lithium metal batteries. Advanced Materials. 2020;32(33):2002850.

[176] Tu Z, Zachman M J, Choudhury S, Khan K A, Zhao Q, Kourkoutis L F, et al. Stabilizing protic and aprotic liquid electrolytes at high-bandgap oxide interphases. Chemistry of Materials. 2018;30(16):5655-5662.

[177] Wondimkun Z T, Beyene T T, Weret M A, Sahalie N A, Huang C-J, Thirumalraj B, et al. Binder-free ultra-thin graphene oxide as an artificial solid electrolyte interphase for

anode-free rechargeable lithium metal batteries. Journal of Power Sources. 2020;450:227589.

[178] Liu Y, Xu X, Sadd M, Kapitanova O O, Krivchenko V A, Ban J, et al. Insight into the Critical Role of Exchange Current Density on Electrodeposition Behavior of Lithium Metal. Advanced Science. 2021;8(5):2003301.

[179] Li Q, Pan H, Li W, Wang Y, Wang J, Zheng J, et al. Homogeneous interface conductivity for lithium dendrite-free anode. ACS Energy Letters. 2018;3(9):2259-2266.

[180] Lee D, Sun S, Kwon J, Park H, Jang M, Park E, et al. Copper nitride nanowires printed Li with stable cycling for Li metal batteries in carbonate electrolytes. Advanced Materials. 2020;32(7):1905573.

[181] He D, Liao Y, Cheng Z, Sang X, Yuan L, Li Z, et al. Facile one-step vulcanization of copper foil towards stable Li metal anode. Science China Materials. 2020;63(9):1663-1671.

[182] Lin K, Li T, Chiang S W, Liu M, Qin X, Xu X, et al. Facile synthesis of Ant-Nest-Like porous duplex copper as deeply cycling host for Lithium metal anodes. Small. 2020;16(37):2001784.

[183] Yang C P, Yin Y X, Zhang S F, Li N W, Guo Y G. Accommodating lithium into 3D current collectors with a submicron skeleton towards long-life lithium metal anodes. Nature Communications. 2015;6:8058.

[184] Ye H, Zheng Z J, Yao H R, Liu S C, Zuo T T, Wu X W, et al. Guiding uniform Li plating/stripping through lithium-aluminum alloying medium for long-life Li metal batteries. Angew Chem Int Ed. 2019;58(4):1094-1099.

[185] Tang Y, Shen K, Lv Z, Xu X, Hou G, Cao H, et al. Three-dimensional ordered macroporous Cu current collector for lithium metal anode: Uniform nucleation by seed crystal. Journal of Power Sources. 2018;403:82-89.

[186] Umh H N, Park J, Yeo J, Jung S, Nam I, Yi J. Lithium metal anode on a copper dendritic superstructure. Electrochemistry Communications. 2019;99:27-31.

[187] Chi S S, Liu Y, Song W L, Fan L Z, Zhang Q. Prestoring lithium into stable 3D nickel foam host as dendrite-free lithium metal anode. Advanced Functional Materials. 2017;27(24):1700348.

[188] Zhang D, Dai A, Wu M, Shen K, Xiao T, Hou G, et al. Lithiophilic 3D porous CuZn current collector for stable lithium metal batteries. ACS Energy Letters. 2019;5(1):180-186.

[189] Yun Q, He Y B, Lv W, Zhao Y, Li B, Kang F, et al. Chemical dealloying derived 3D porous current collector for Li metal anodes. Advanced Materials. 2016;28(32):6932-6939.

[190] Li Q, Zhu S, Lu Y. 3D porous Cu current collector/Li-metal composite anode for stable lithium-metal batteries. Advanced Functional Materials. 2017;27(18):1606422.

[191] Kim H, Gong Y J, Yoo J, Kim Y S. Highly stable lithium metal battery with an applied three-dimensional mesh structure interlayer. Journal of Materials Chemistry A. 2018;6(32):15540-15545.

[192] Chang J, Shang J, Sun Y, Ono L K, Wang D, Ma Z, et al. Flexible and stable high-energy lithium-sulfur full batteries with only 100% oversized lithium. Nature Communications. 2018;9(1):4480.

[193] Chen X, Lv Y, Shang M, Niu J. Ironing controllable lithium into lithiotropic carbon fiber fabric: A novel Li-metal anode with improved cyclability and dendrite suppression. ACS Appl Mater Interfaces. 2019;11(24):21584-21592.

[194] Huang G, Han J, Zhang F, Wang Z, Kashani H, Watanabe K, et al. Lithiophilic 3D nanoporous nitrogen-doped graphene for dendrite-free and ultrahigh-rate lithium-metal anodes. Adv Mater. 2019;31(2):1805334.

[195] Matsuda S, Kubo Y, Uosaki K, Nakanishi S. Lithium-metal deposition/dissolution within internal space of CNT 3D matrix results in prolonged cycle of lithium-metal negative electrode. Carbon. 2017;119:119-123.

[196] Qiu H, Tang T, Asif M, Huang X, Hou Y. 3D porous Cu current collectors derived by hydrogen bubble dynamic template for enhanced Li metal anode performance. Advanced Functional Materials. 2019;29(19):1808468.

[197] Diao W Y, Xie D, Li Y F, Jiang R, Tao F Y, Sun H Z, et al. Sustainable and robust graphene cellulose paper decorated with lithiophilic Au nanoparticles to enable dendrite-free and High-Power lithium metal anode. Chemistry-A European Journal. 2021;27(31):8168-8177.

[198] Hu W, Yao Y, Huang X, Ju S, Chen Z, Li M, et al. CuO nanofilm-covered Cu microcone coating for a long cycle Li metal anode by In Situ formed $Li_2O$. ACS Applied Energy Materials. 2022;5(3):3773-3782.

[199] Luo Y, He G. Clusters of CuO nanorods arrays for stable lithium metal anode. Journal of Materials Science. 2020;55(21):9048-9056.

[200] Yang S, Xiao R, Zhang T, Li Y, Zhong B, Wu Z, et al. Cu nanowires modified with carbon-rich conjugated framework PTEB for stabilizing lithium metal anodes. Chemical Communications. 2021;57(99):13606-13609.

[201] Wang J-r, Wang M-m, He X-d, Wang S, Dong J-m, Chen F, et al. A lithiophilic 3D conductive skeleton for high performance Li metal battery. ACS Applied Energy Materials. 2020;3(8):7265-7271.

[202] Qian Y, Wei C, Tian Y, Xi B, Xiong S, Feng J, et al. Constructing ultrafine lithiophilic layer on MXene paper by sputtering for stable and flexible 3D lithium metal anode. Chemical Engineering Journal. 2021;421:129685.

[203] Lin H, Zhang Z, Wang Y, Zhang X L, Tie Z, Jin Z. Template-Sacrificed hot fusion construction and nanoseed modification of 3D porous copper nanoscaffold host for stable-cycling lithium metal anodes. Advanced Functional Materials. 2021;31(30):2102735.

[204] Zhang S, Yang G, Li X, Li Y, Wang Z, Chen L. Electrolyte and current collector designs for stable lithium metal anodes. International Journal of Minerals, Metallurgy and Materials. 2022;29(5):953-964.

[205] Zhao Y, Hao S, Su L, Ma Z, Shao G. Hierarchical Cu fibers induced Li uniform nucleation for dendrite-free lithium metal anode. Chemical Engineering Journal. 2020;392:123691.

[206] Lu L L, Ge J, Yang J N, Chen S M, Yao H B, Zhou F, et al. Free-Standing copper nanowire network current collector for improving lithium anode performance. Nano Lett. 2016;16(7):4431-4437.

[207] Hu W, Rao Y, Chen P, Ju S, Ling H, Wu Y, et al. Nano-Cone structured lithiophilic Ni film on Cu current collector facilitates $Li^+$ Ion diffusion toward uniform lithium deposition. Advanced Materials Interfaces. 2022;9(15):2200129.

[208] Cao J, Deng L, Wang X, Li W, Xie Y, Zhang J, et al. Stable lithium metal anode achieved by In Situ grown CuO nanowire arrays on Cu foam. Energy & Fuels. 2020;34(6):7684-7691.

[209] Whittingham M S. Electrical energy storage and intercalation chemistry. Science. 1976;192(4244):1126-1127.

[210] Zhang N, Zhao T, Wei L, Feng T, Wu F, Chen R. Stable Li/$Cu_2O$ composite anodes enabled by a 3D conductive skeleton with lithiophilic nanowire arrays. Journal of Power Sources. 2022;536:231374.

[211] Zhang Q, Luan J, Tang Y, Ji X, Wang S, Wang H. A facile annealing strategy for achieving in situ controllable $Cu_2O$ nanoparticle decorated copper foil as a current collector for stable lithium metal anodes. Journal of Materials Chemistry A. 2018;6(38):18444-18448.

[212] Cai Y, Qin B, Li C, Si X, Cao J, Zheng X, et al. Stable lithium metal anode achieved by shortening diffusion path on solid electrolyte interface derived from $Cu_2O$ lithiophilic layer. Chemical Engineering Journal. 2022;433:133689

[213] Jiang H, Dong Q, Bai M, Qin F, Yi M, Lai J, et al. A 3D-mixed ion/electron conducting scaffold prepared by in situ conversion for long-life lithium metal anodes. Nanoscale. 2021;13(5):3144-3152.

[214] Zhao M, Huang X, Zhuang D, Sheng L, Xie X, Cao M, et al. Constructing porous nanosphere structure current collector by nitriding for lithium metal batteries. Journal of Energy Storage. 2022;47:103665

[215] Liu X F, Xie D, Tao F Y, Diao W Y, Yang J L, Luo X X, et al. Regulating the Li nucleation/growth behavior via $Cu_2O$ nanowire array and artificial solid electrolyte interphase toward highly stable Li metal anode. ACS Appl Mater Interfaces. 2022;14(20):23588-23596.

[216] Wu Q, Qin M, Yan H, Zhong W, Zhang W, Liu M, et al. Facile replacement reaction enables Nano-Ag-Decorated Three-Dimensional Cu foam as High-Rate lithium metal anode. ACS Appl Mater Interfaces. 2022;14(37):42030-42037.

[217] Zhao B, Li B, Wang Z, Xu C, Liu X, Yi J, et al. Uniform Li deposition sites provided by atomic layer deposition for the dendrite-free lithium metal anode. ACS Appl Mater Interfaces. 2020;12(17):19530-19538.